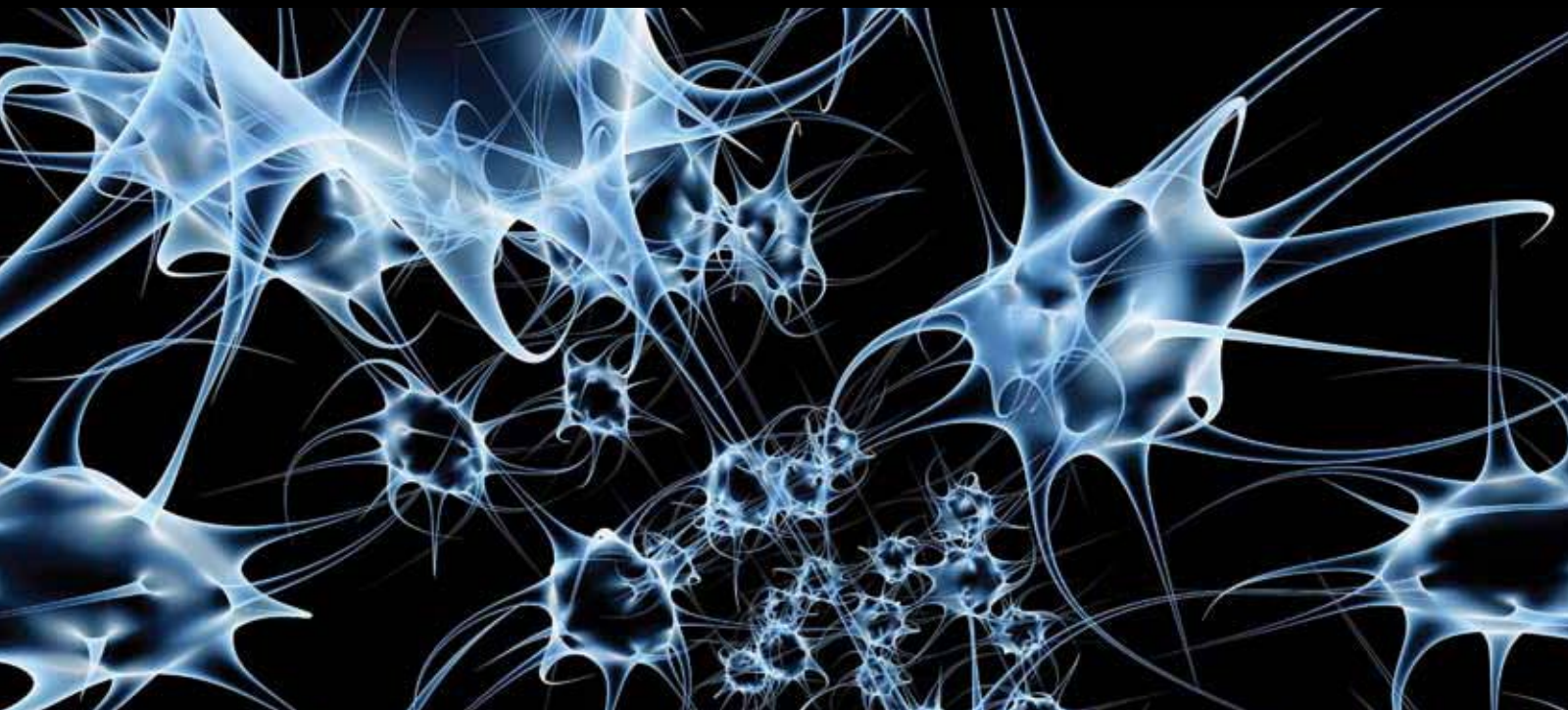


# Multimodal MRI in Neurodegenerative Disorders

GUEST EDITORS: ANTONIO CERASA, ANDREA CHERUBINI, AND PATRICE PERAN





---

# **Multimodal MRI in Neurodegenerative Disorders**

Neurology Research International

---

## **Multimodal MRI in Neurodegenerative Disorders**

Guest Editors: Antonio Cerasa, Andrea Cherubini,  
and Patrice Peran



---

Copyright © 2012 Hindawi Publishing Corporation. All rights reserved.

This is a special issue published in volume 2012 of "Neurology Research International." All articles are open access articles distributed under the Creative Commons Attribution License, which permits unrestricted use, distribution, and reproduction in any medium, provided the original work is properly cited.

## Editorial Board

Jason J. S. Barton, Canada	Fady T. Charbel, USA	Richard Maddock, USA
George Bartzokis, USA	Prabhakara V. Choudary, USA	B. R. Ott, USA
Ralf W. Baumgartner, Switzerland	Mamede de Carvalho, Portugal	D. Pleasure, USA
T. Ben-Hur, Israel	Dirk Deleu, Qatar	Mohammed Rachidi, France
Julien Bogousslavsky, Swaziland	Vincenzo Di Lazzaro, Italy	Vijayalakshmi Ravindranath, India
M. Brainin, Austria	Takamitsu Fujimaki, Japan	G. Sebire, Canada
Herbert Brok, The Netherlands	Changiz Geula, USA	Marcus Stoodley, Australia
Jeff Bronstein, USA	Jean-Michel Guerit, Belgium	Peter van den Bergh, Belgium
Ferdinando S. Buonanno, USA	Linda Liau, USA	Zinaida Vexler, USA
Jean-Marc Burgunder, Switzerland	A. C. Ludolph, Germany	Richard A. Wennberg, Canada
Leo Chalupa, USA		Michael J. Zigmond, USA

# Contents

**Multimodal MRI in Neurodegenerative Disorders**, Antonio Cerasa, Andrea Cherubini, and Patrice Peran  
Volume 2012, Article ID 287891, 2 pages

**Structural Angle and Power Images Reveal Interrelated Gray and White Matter Abnormalities in Schizophrenia**, Lai Xu, Tülay Adali, David Schretlen, Godfrey Pearlson, and Vince D. Calhoun  
Volume 2012, Article ID 735249, 18 pages

**Multimodal MRI Neuroimaging Biomarkers for Cognitive Normal Adults, Amnesic Mild Cognitive Impairment, and Alzheimer's Disease**, Ai-Ling Lin, Angela R. Laird, Peter T. Fox, and Jia-Hong Gao  
Volume 2012, Article ID 907409, 17 pages

**DTI and MR Volumetry of Hippocampus-PC/PCC Circuit: In Search of Early Micro- and Macrostructural Signs of Alzheimer's Disease**, F. Palesi, P. Vitali, P. Chiarati, G. Castellazzi, E. Caverzasi, A. Pichiecchio, E. Colli-Tibaldi, F. D'Amore, I. D'Errico, E. Sinforiani, and S. Bastianello  
Volume 2012, Article ID 517876, 9 pages

**Understanding the Pathophysiology of Alzheimer's Disease and Mild Cognitive Impairment: A Mini Review on fMRI and ERP Studies**, Takao Yamasaki, Hiroyuki Muranaka, Yumiko Kaseda, Yasuyo Mimori, and Shozo Tobimatsu  
Volume 2012, Article ID 719056, 10 pages

**A Pilot Study of Quantitative MRI Measurements of Ventricular Volume and Cortical Atrophy for the Differential Diagnosis of Normal Pressure Hydrocephalus**, Dana W. Moore, Ilhami Kovanlikaya, Linda A. Heier, Ashish Raj, Chaorui Huang, King-Wai Chu, and Norman R. Relkin  
Volume 2012, Article ID 718150, 6 pages

**MRI Findings in Neuroferritinopathy**, Emiko Ohta and Yoshihisa Takiyama  
Volume 2012, Article ID 197438, 7 pages

## Editorial

# Multimodal MRI in Neurodegenerative Disorders

**Antonio Cerasa,<sup>1</sup> Andrea Cherubini,<sup>1</sup> and Patrice Peran<sup>2,3</sup>**

<sup>1</sup>Neuroimaging Research Unit, Institute of Neurological Sciences, National Research Council, 88100 Catanzaro, Italy

<sup>2</sup>Inserm, Imagerie Cérébrale et Handicaps Neurologiques, UMR 825, 31059 Toulouse, France

<sup>3</sup>Université de Toulouse (UPS), Imagerie Cérébrale et Handicaps Neurologiques, UMR 825, 31059 Toulouse, France

Correspondence should be addressed to Antonio Cerasa, a.cerasa@isn.cnr.it

Received 17 July 2011; Accepted 17 July 2011

Copyright © 2012 Antonio Cerasa et al. This is an open access article distributed under the Creative Commons Attribution License, which permits unrestricted use, distribution, and reproduction in any medium, provided the original work is properly cited.

In the last twenty years, advanced magnetic resonance imaging (MRI) techniques have provided fundamental knowledge about neurodegenerative processes underlying several neurological and psychiatric diseases.

The native approach in this field of study was the investigation of a single MRI parameter at a time: (a) blood oxygenation-level-dependent (BOLD) images, (b) anatomical 3D T1-weighted images, (c) diffusion-weighted imaging (DWI)/diffusion tensor imaging (DTI), and (d) quantitative relaxometry. (a) The common observation in functional MRI studies is that increasing in the BOLD MRI signal represents increasing of neural activity. Such a neurophysiological “activation” results from elevated oxygen saturation levels (and reduced paramagnetic deoxyhemoglobin contents) of capillary and venous blood. These positive signal changes are considered the basis for the functional organization of the brain. (b) The T1-weighted sequence allows the employment of several neuroanatomical techniques able to describe and quantify macrostructural changes by using probabilistic (voxel-based morphometry analysis) or quantitative research tools (manual/automatic region-of-interest volumetry, cortical thickness measurements). (c) DWI and DTI provide specific quantitative measurement of microstructural changes within white and gray matter compartments. In particular DTI provides quantitative parameters, such as the mean diffusivity that increases with microscopic barrier disruption and extracellular fluid accumulation and the fractional anisotropy that provides information on the microstructural integrity of highly oriented microstructures (i.e., myelin). (d) Finally, another potential MRI technique is the quantification of mineral levels in the brain. MR relaxometry is a sensitive method to evaluate the brain iron

content *in vivo*. Iron accumulation has been implicated in the pathogenesis of many neurodegenerative diseases.

In the last five years, multimodal neuroimaging has become the most popular approach to study pathophysiology of diseased brain. In fact, the aim of this field of study is to quantify the single or combined weight of MRI parameters in describing neurodegenerative processes. In other words, the possibility to measure MR parameters sensitive to complementary tissue characteristics (e.g., volume atrophy, iron deposition, and microstructural damage) could have great potential for investigating pathological changes in several neurologic/psychiatric diseases. At this moment, important new findings have been reported although several issues remain open. In this special edition, we have featured some papers that address such issues.

The first paper of this special edition is more forward-looking. In fact, it presents a new experimental multimodal MRI approach to better elucidate interrelated gray and white matter changes in schizophrenic patients. This new method represents a theoretical evolution of the previous and well-known voxel-based analysis of T1-weighted images that generally provides a mixed measure of neuronal “volume” or “density.”

The second and third papers provide fundamental overviews of recent findings about neurodegenerative processes underlying Alzheimer’s disease (AD) and mild cognitive impairments (MCIs) obtained through a multimodal neuroimaging approach. The subsequent paper addresses the specific advance in functional neuroimaging studies of AD and MCI patients. All these papers highlight the importance of multimodal neuroimaging in enhancing our ability to diagnose MCI and AD in its early stages.

Finally, the last two papers present the application of advanced MRI measurements (automatic ROI volumetry, cortical thickness measurements, and T2\* iron quantification) to define the presence of new biomarkers able to distinguish AD patients from normal pressure hydrocephalus and to improve the accurate diagnosis of suspect neuroferritinopathy, a neurodegenerative disorder characterized by the deposition of iron and ferritin in the brain.

*Antonio Cerasa  
Andrea Cherubini  
Patrice Peran*

## Research Article

# Structural Angle and Power Images Reveal Interrelated Gray and White Matter Abnormalities in Schizophrenia

Lai Xu,<sup>1,2</sup> Tülay Adali,<sup>3</sup> David Schretlen,<sup>4</sup> Godfrey Pearlson,<sup>5,6</sup> and Vince D. Calhoun<sup>1,2,4,5,6</sup>

<sup>1</sup>The Mind Research Network, Albuquerque, NM 87106, USA

<sup>2</sup>Department of ECE, University of New Mexico, Albuquerque, NM 87131, USA

<sup>3</sup>Department of CSEE, University of Maryland Baltimore County, Baltimore, MD 21250, USA

<sup>4</sup>Department of Psychiatry, Johns Hopkins University School of Medicine, Baltimore, MD 21287, USA

<sup>5</sup>Olin Neuropsychiatry Research Center, Institute of Living, Hartford, CT 06106, USA

<sup>6</sup>Department of Psychiatry, Yale University School of Medicine, New Haven, CT 06520, USA

Correspondence should be addressed to Vince D. Calhoun, vcalhoun@unm.edu

Received 24 February 2011; Revised 14 June 2011; Accepted 20 June 2011

Academic Editor: Patrice Peran

Copyright © 2012 Lai Xu et al. This is an open access article distributed under the Creative Commons Attribution License, which permits unrestricted use, distribution, and reproduction in any medium, provided the original work is properly cited.

We present a feature extraction method to emphasize the interrelationship between gray and white matter and identify tissue distribution abnormalities in schizophrenia. This approach utilizes novel features called structural phase and magnitude images. The phase image indicates the relative contribution of gray and white matter, and the magnitude image reflects the overall tissue concentration. Three different analyses are applied to the phase and magnitude images obtained from 120 healthy controls and 120 schizophrenia patients. First, a single-subject subtraction analysis is computed for an initial evaluation. Second, we analyze the extracted features using voxel based morphometry (VBM) to detect voxelwise group differences. Third, source based morphometry (SBM) analysis was used to determine abnormalities in structural networks that co-vary in a similar way. Six networks were identified showing significantly lower white-to-gray matter in schizophrenia, including thalamus, right precentral-postcentral, left pre/post-central, parietal, right cuneus-frontal, and left cuneus-frontal sources. Interestingly, some networks look similar to functional patterns, such as sensory-motor and vision. Our findings demonstrate that structural phase and magnitude images can naturally and efficiently summarize the associated relationship between gray and white matter. Our approach has wide applicability for studying tissue distribution differences in the healthy and diseased brain.

## 1. Introduction

Structural magnetic resonance imaging (sMRI) obtains high-resolution structural images that are useful for brain morphometry investigation. In sMRI images, two types of brain tissue, gray matter and white matters, are clearly perceptible and distinguishable. Usually, these two tissues are analyzed separately in studies of both healthy and diseased brain [1–3]. However, the relationship between gray and white matters is complicated. Gray matter is composed predominantly of cell bodies while white matter is composed mainly of axons connecting cell bodies; both are highly integrated within cerebral cortex and subcortical structures; spatial expansion of one can be associated with contraction of the other [4, 5]. Therefore, it is reasonable to expect that morphometric

changes in one tissue may result in or be related to disturbance of the other.

Several previous approaches have examined the relationship between gray and white matters. In voxel-based morphometry (VBM) studies, sMRI images were segmented first and the voxelwise correlation between regional cerebral gray and white matters was calculated [6, 7]; in region of interest (ROI) studies, gray and white matters were correlated with volumes in the rest of the cortex [8]. These correlation studies addressed the intricate relationship between gray and white matters and provided evidence of gray and white matter relative differences between diagnostic groups. One limitation of these approaches is that the correlations can only be calculated between individual voxels or between averages within prespecified regions. More complicated gray and

white matter relationships can be studied by using univariate ANCOVA [9] or by using multivariate independent component analysis to identify linked gray and white matter networks [10]. In the current study, we propose a new approach to directly extract new features for gray and white matter fusion. The extracted angle and power features are sensitive to the gray and white matter interrelationship and can be used for single-subject diagnostic analysis or for group level analysis.

Schizophrenia affects multiple brain regions including both gray and white matters [11], it is likely that the interrelationship between gray and white matters is affected in this mental illness. The disconnection model of schizophrenia [12] has led to increased focus on both gray and white matter analysis. Reviews of structural brain imaging in schizophrenia [11, 13] highlighted multiple regional abnormalities; reviews of white matter changes [14, 15] suggest that white matter disconnections are associated with the abnormalities, and reports of the corpus callosum and thalamus [16–18] identified subcortical regions whose abnormalities would likely reflect disturbances in circuits of multiple structural systems.

In this paper, our feature extraction method was applied to a large data set of healthy controls and schizophrenia patients, and the corresponding structural angle and power images were computed. As an initial evaluation, we performed a subtraction analysis between a single schizophrenia patient and a single healthy control. We then performed a univariate VBM analysis to detect the group level abnormalities in a voxelwise manner. Finally, an SBM analysis was used to detect structural networks covarying in a similar way which were related to the schizophrenia disturbances.

## 2. Methods

**2.1. Subjects and Imaging Parameters.** One hundred and twenty participants with schizophrenia (SZ) (mean age 42.1, SD 12.9, range 20–81, 51 females) and 120 matched healthy controls (mean age 42.7, SD 16.6, range 18–78, 65 females) were scanned at Johns Hopkins University. Exclusion criteria for all participants included a history of overt brain disease, mental retardation, head injury with loss of consciousness for greater than 60 minutes, or a diagnosis of substance abuse within the last year or lifetime substance dependence. Healthy participants were recruited using random digit dialing as part of Phase 1 of the Johns Hopkins aging, brain imaging, and cognition (ABC) study [19], a representative community sample. All healthy controls were screened to ensure they were free from current major depression, bipolar disorder, schizophrenia, and severe anxiety disorders using the schedule for clinical assessment in neuropsychiatry (SCAN) interview [20]. Patients met DSM-IV criteria for schizophrenia on the basis of the diagnostic interview for genetic studies (DIGSs) and review of the available medical records [21]. All patients with schizophrenia were stable and taking antipsychotic medications (precise medication information was not available for these data). These data were previously analyzed using SBM [22] and jSBM [10].

Whole brain sMRIs were obtained on a single 1.5T scanner (Signa; GE Medical Systems, Milwaukee, Wis). The whole brain was evaluated in the coronal plane using a spoiled GRASS 3D imaging sequence, with the following imaging parameters: 35 ms TR, 5 ms TE, 45° flip angle, 1 excitation, 1.5 mm slice thickness, 24 cm field of view, and a matrix size of  $256 \times 256$ .

**2.2. Image Preprocessing.** The images were preprocessed using the preprocessing steps typically applied for VBM [23, 24] and employed the Matlab program SPM5 (Statistical Parametric Mapping, Wellcome Institute, London, UK). Images were normalized to the 152 average  $T_1$  Montreal Neurological Institute (MNI) templates, interpolated to voxel dimensions of  $1.5 \times 1.5 \times 1.5$  mm and segmented into gray matter, white matter, and cerebrospinal fluid (CSF) compartments. Registration, bias correction, and tissue classification were combined within one generative Gaussian mixture model which takes image intensity nonuniformities and tissue probability maps into consideration. The model parameter estimation involves alternating among classification, bias correction, and registration steps and aims to maximize the posterior solution of the three compartments. Then, the segmented gray matter and white matter images were smoothed separately with 12-mm full width at half-maximum (FWHM) Gaussian kernel. Each voxel in a smoothed image contains the averaged concentration of gray matter or white matter from around and within the selected voxel, a value ranging from 0 to 1. Next, we generated a mask using the smoothed gray and white matter images. The corresponding gray and white images were added together and then averaged. The averaged image was threshold at 0.1 and used to mask the smoothed gray or white matter images in order to exclude regions of very low concentrations (less than 0.1 of either gray or white matter). The masked gray and white matter images were used in the following steps. The size of each processed image was  $121 \times 145 \times 121$  voxels.

**2.3. Gray and White Matter Fusion: Structural Angle and Power Images.** Structural angle and power images are then computed in order to combine/fuse gray and white matter tissue estimates. The overall scheme we use for image generation is represented in Figure 1. From one sMRI image, we obtain gray matter and white matter images. We assume the gray matter concentration within each voxel in the gray matter image is  $g_i$  and the white matter concentration within each voxel in the corresponding white matter image is  $w_i$ ,  $i = 1, \dots, 121 \times 145 \times 121$ . Next, we construct a complex variable  $g_i + jw_i$  for each and every voxel where  $g_i$  is the gray matter concentration and  $w_i$  is the white matter concentration. Thus, the phase/angle part of the complex variable is  $\varphi_i(g_i, w_i) = \arctan(w_i/g_i)$ . The magnitude/power part of the complex variable is  $M_i(g_i, w_i) = \sqrt{g_i^2 + w_i^2}$ . The structural angle image is then constructed based on the angle value of each voxel, and the structural power image is constructed based on the power value of each voxel.

Compared to approaches that work with the segmented gray and white matter images, the structural angle and power

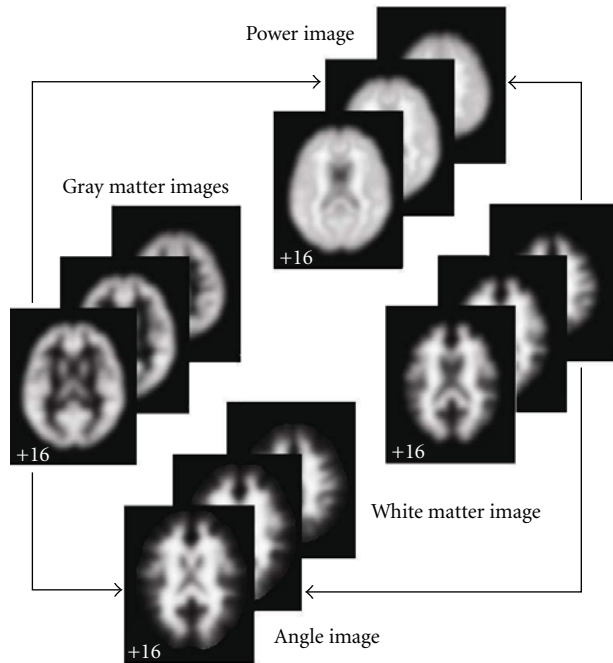


FIGURE 1: Structural angle and power image generation. Structural angle and power images are generated from the segmented gray and white matter images.

images we define emphasize more the relationship of gray and white matter distribution instead of focusing on the pure gray or white density. The angle image reflects the relative contributions of gray and white matter within each voxel and is proportional to the gray and white matter ratio changes. The power image is the mean power of the gray and white matter tissue concentrations and is proportional to overall tissue concentration. Thus, the angle and power images naturally and efficiently fuse gray and white matter together to emphasize the relationship between tissues and enable subsequent analysis without increasing computing complexity. Next, we apply three different methods, single-subject subtraction, VBM and SBM, to provide intuition and explain the utility of the structural angle and power images to study brain structure.

**2.4. Single-Subject Subtraction Analysis of Structural Angle and Power Images.** The structural angle and power features highlighted the interrelationship of gray and white matter for each subject. We performed a simple subtraction of randomly selected angle/power images between one healthy control and one patient to demonstrate the approach.

**2.5. VBM Analysis of Structural Angle and Power Images.** In order to detect statistically meaningful group differences, VBM was performed on the angle and power image set using SPM5. The 240 structural angle images and 240 structural power images were directly entered into a two sample  $t$ -test separately. The resulting angle/power  $t$ -maps highlight voxels that showed significant differences in angle/power between healthy controls and patients. The  $t$ -maps were then

converted to angle/power  $Z$ -maps and thresholded at a value of  $|Z| > 3.0$  for visualization.

**2.6. SBM Analysis of Structural Angle and Power Images.** We also performed an SBM analysis to identify structural networks showing group differences and common intersubject covariation. SBM was performed on the angle/power image set using the GIFT toolbox. SBM [22] is an approach that has been successfully applied to identify gray or white matter sources separately in sMRI images. A “source” is a network comprising several regions that together exhibit intersubject covariance and show group differences. Compared to VBM, SBM is a multivariate data-driven method taking cross-voxel information into account, which results in group differences that are represented by maximally independent sources not voxels as in VBM. Our previous work [22] has shown the effectiveness of applying SBM for network detection in segmented gray matter images. Here we applied SBM to structural angle and power images to detect networks of relative gray and white matter changes. This SBM approach consists of three steps: independent component analysis (ICA), statistical analysis, and visualization.

First, ICA is performed on the angle images and power images separately (see Figure 2). We take the angle images as our example. Each angle image is converted to a one-dimensional vector. The 120 angle image vectors of healthy controls and 120 angle image vectors of patients are then arrayed into one 240 row subject-by-angle matrix. Akaike’s information criterion (AIC), modified to improve the estimation performance for medical images [25], was applied to the matrix in order to estimate the number of sources  $k$ . Next, the subject-by-angle matrix was decomposed into a subject  $\times$  source *angle mixing matrix* and source  $\times$  angle *angle source matrix* using spatial ICA [26]. The angle mixing matrix expresses the relationship between 240 subjects and  $k$ -angle sources. The rows of the matrix are scores that indicate to what degree each of the  $k$ -angle sources contribute to a given subject. The columns of the matrix indicate how one angle source contributes to the 240 subjects. In contrast, the angle source matrix expresses the relationship between the  $k$ -angle sources and the voxels within the brain. The rows of the matrix indicate how one angle source contributes to different brain voxels and the columns of the matrix are scores that indicate how one voxel contributes to each of the angle sources. The same process was applied to the 240 power images to determine the *power mixing matrix* and *power source matrix*.

Then statistical analysis was performed on the angle mixing matrix and power mixing matrix separately. Since every column of the mixing matrix contains the loading parameters expressing the contribution of every source for the 240 subjects, a two-sample  $t$ -test can be used on each column of the mixing matrix to test which source shows a significant control versus schizophrenia difference. A corrected threshold of  $P < 0.05$ , controlling for the false discovery rate (FDR), was used to identify the most significant sources [27]. The effects of age and gender on the significant sources were also determined. We regressed the columns of the mixing matrix

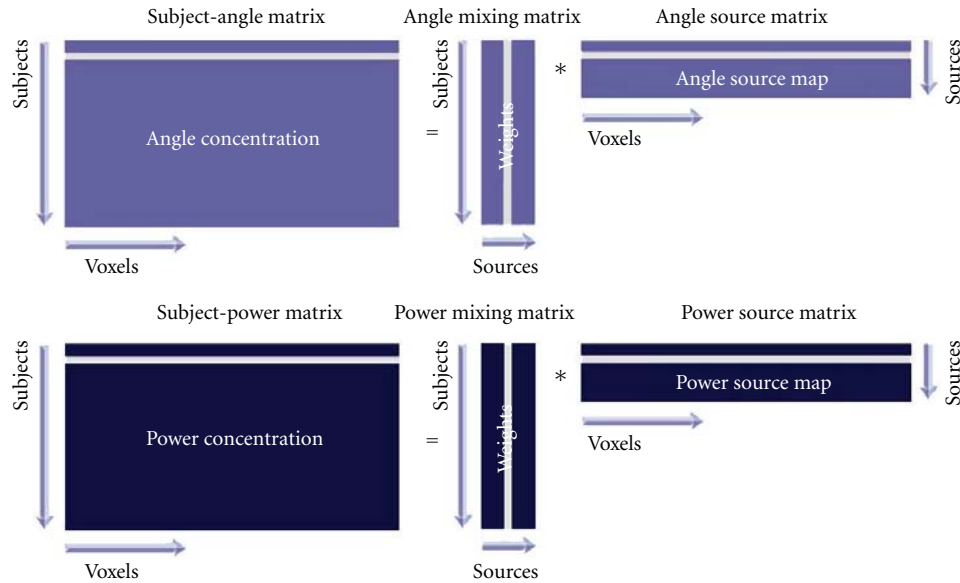


FIGURE 2: Independent component analysis on angle and power images. Angle or power images are stacked into one subject-angle/power matrix. ICA is then used to decompose this matrix into a mixing matrix and a source matrix. The mixing matrix is used for statistical analysis and the source matrix is used for sources visualization in the following steps.

on these variables using a threshold of  $P < 0.05$  to determine sources that were significantly correlated with them. In order to verify that the group differences in the significant sources were still present after removing the effect of age and gender, we computed a two-sample  $t$ -test on the residual of the regression and tested the difference between controls and patients.

Finally, the source matrix was used for visualization. The angle source maps were obtained from the angle source matrix and power source maps were obtained from the power source matrix. Each row of the source matrix was scaled to unit standard deviation, then reshaped separately into one 3D image (source map). The significant source maps were then superimposed on the MNI-normalized template brain and thresholded at  $|Z| > 3.0$ . Regions within the most significant sources were labeled by transforming from the MNI coordinate system to the coordinates of the standard space of Talairach and Tournoux [28] using a Matlab conversion program (<http://imaging.mrc-cbu.cam.ac.uk/downloads/MNI2tal/>; MRC Cognition and Brain Sciences Unit, Cambridge, England). Once converted, the Talairach coordinates were entered into the Talairach daemon [29] and summarized. In addition, white matter regions within significant sources were thresholded at  $|Z| > 3.0$  and specifically labeled using the ICBM DTI-81 atlas [30].

**2.7. Simulations.** Figure 3(a) presents a simple plot of gray matter versus the ratio of white matter/gray matter (assuming for simplicity that gray matter =  $1 -$  white matter). Approximate cases with mostly gray matter, mostly white matter, and in between (boundary regions) are denoted on the plots as well. It is clear this is a highly nonlinear relationship with the function going to infinity as gray matter approaches zero. Figure 3(b) shows that gray matter versus

the structural angle is much more linear, with some smaller nonlinearities as gray matter or white matter goes to zero. This squashing of the instability near zero is a very useful property of the atan function. Also note that the slope is steeper than that for gray matter. As we will see in the next simulation, the structural angle also provides increased sensitivity to group differences compared to using gray matter alone.

In order to better understand the added value of using the angle measure, we performed a simulation of a single voxel in a group of 100 subjects in group 1 and 100 subjects in group 2. We generated data for a range of gray matter values from 5% to 90% in a given voxel for each group. For each gray matter, setting a small amount of random (uniform) noise was added to each voxel. White matter voxels were then calculated assuming that white matter =  $1 -$  gray matter. Once this data was generated, we computed the two-sample  $T$ -values for group 1 versus group 2 for either the gray matter values along (analogous to standard VBM) or for the angle arc  $\tan(w_m/g_m)$ . Results are presented in Figure 4. In general, the pattern of the  $T$ -values is quite similar for both gray matter and angle ( $T$ -values and log of absolute  $T$ -values are shown). Unsurprisingly, the largest  $T$ -values for both measures occur when one group have large gray matter values and the other group has small gray matter values. The difference in these  $T$ -values tells us where the sensitivity is greater for either gray matter or angle. Figure 4(d) (red regions) show where the angle value is greater than the gray matter value. In general, the angle measure is providing more sensitivity to the group differences than gray matter alone, especially where one group has larger gray matter values and the other group has smaller gray matter values. This includes, but is not limited to, regions where boundaries between gray matter and white matter are shifted in the two groups

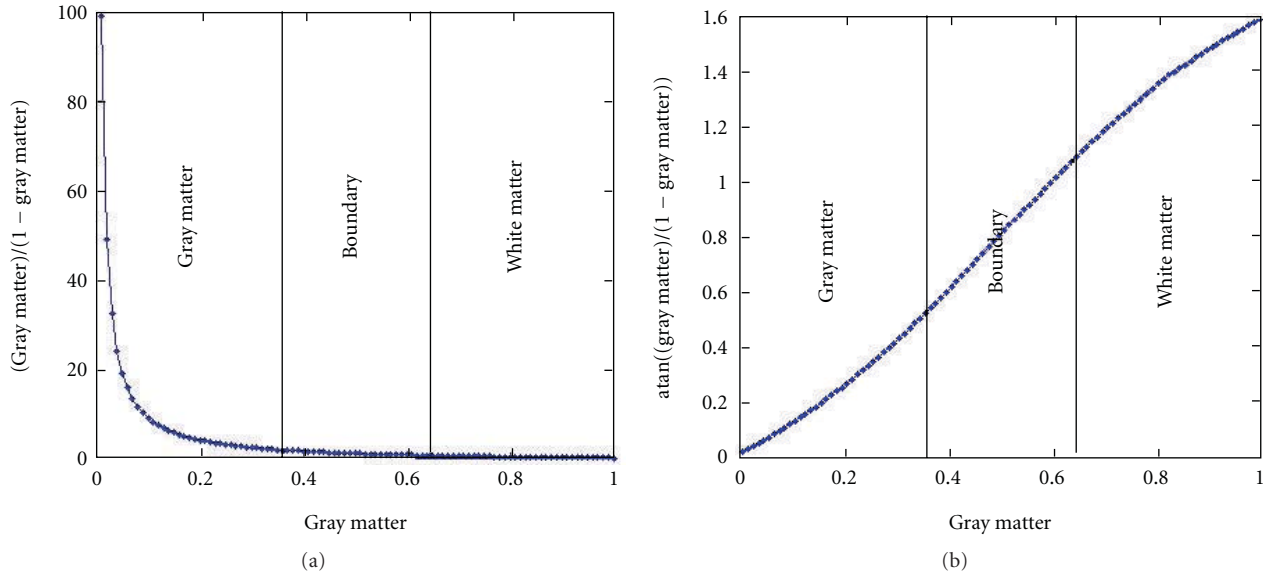


FIGURE 3: Evaluation of atan function.

(e.g., where the gray matter in one group drops off faster than that in the other group). In contrast, the power images have the greatest sensitivity to group differences where the gray matter value of one group is more similar to that of the other group and when both groups have larger gray matter values.

### 3. Results

We propose structural angle and power as two new features describing the interrelationship of gray and white matters. We show the results of the three different analyses performed on the structural angle and power images extracted from the sMRI images of healthy controls and schizophrenia patients below. We also show an application of these features to study schizophrenia.

**3.1. Results of Single-Subject Subtraction: Single-Subject Abnormality.** By simply subtracting the structural angle and power images between subjects, we highlighted the regions showing subject differences of overall gray and white matter distribution. As shown in Figure 5, the upper row consists of angle images and the bottom consists of power images. The first column shows the images from one healthy adult. The second shows images from one patient with schizophrenia. The third depicts subtraction-related differences in the angle and power images. Compared to the healthy adult, the patient with schizophrenia showed higher angle values in middle temporal and frontal gyri, precuneus and cuneus, cingulum, the body and splenium of corpus callosum, and lower power values in superior and inferior frontal gyri, superior temporal gyrus, and fornix.

**3.2. Results of VBM Analysis: Group Level Differences.** By applying VBM on the structural angle and power images, the statistical Z-maps (see Figure 6) reflecting the group

differences of relative gray and white matter between controls and patients were obtained. The Talairach coordinates for the maps are listed in Table 1. The white matter determined by ICBM DTI-81 atlas is listed in Table 2.

The angle map reveals significantly higher white-to-gray ratio for patients with schizophrenia in thalamus, internal capsule, insula, cuneus and precuneus, superior and middle frontal gyri, inferior frontooccipital fasciculus, and uncinate fasciculus. The power map shows the most significant average concentration differences between the diagnostic groups in bilateral superior temporal gyrus, medial and superior frontal gyri, claustrum, external capsule, cingulum, inferior frontooccipital fasciculus and uncinate fasciculus. The temporal regions are notably constrained to the superior temporal gyrus and its medial counterparts, the transverse temporal gyrus and insula, suggesting a clear distinction between these structures and the rest of the temporal lobe.

**3.3. Results of SBM Analysis: Network Disturbances.** Through SBM analysis, sources that are formed by networking regions showing the same intersubject covariance can be detected. The number of angle sources was estimated to be 25, and the number of power sources to be 37 using the modified AIC approach. Eight angle sources and three power sources were identified as having loading parameters that significantly differed between controls and patients. On visual inspection of the source maps, two angle sources and two power sources appeared to be obvious artifacts showing sharp edges near the brain boundary or appearing within CSF regions. Within the remaining six angle sources and one power source, the loading parameters of patients in the mixing matrix were all lower than those of controls. Each of the identified sources includes regions reflecting group differences in angle/power covariation among subjects (see Figure 7). The Talairach coordinates for the sources are listed in Table 3. The white matter determined by ICBM DTI-81 atlas is listed in Table 4.

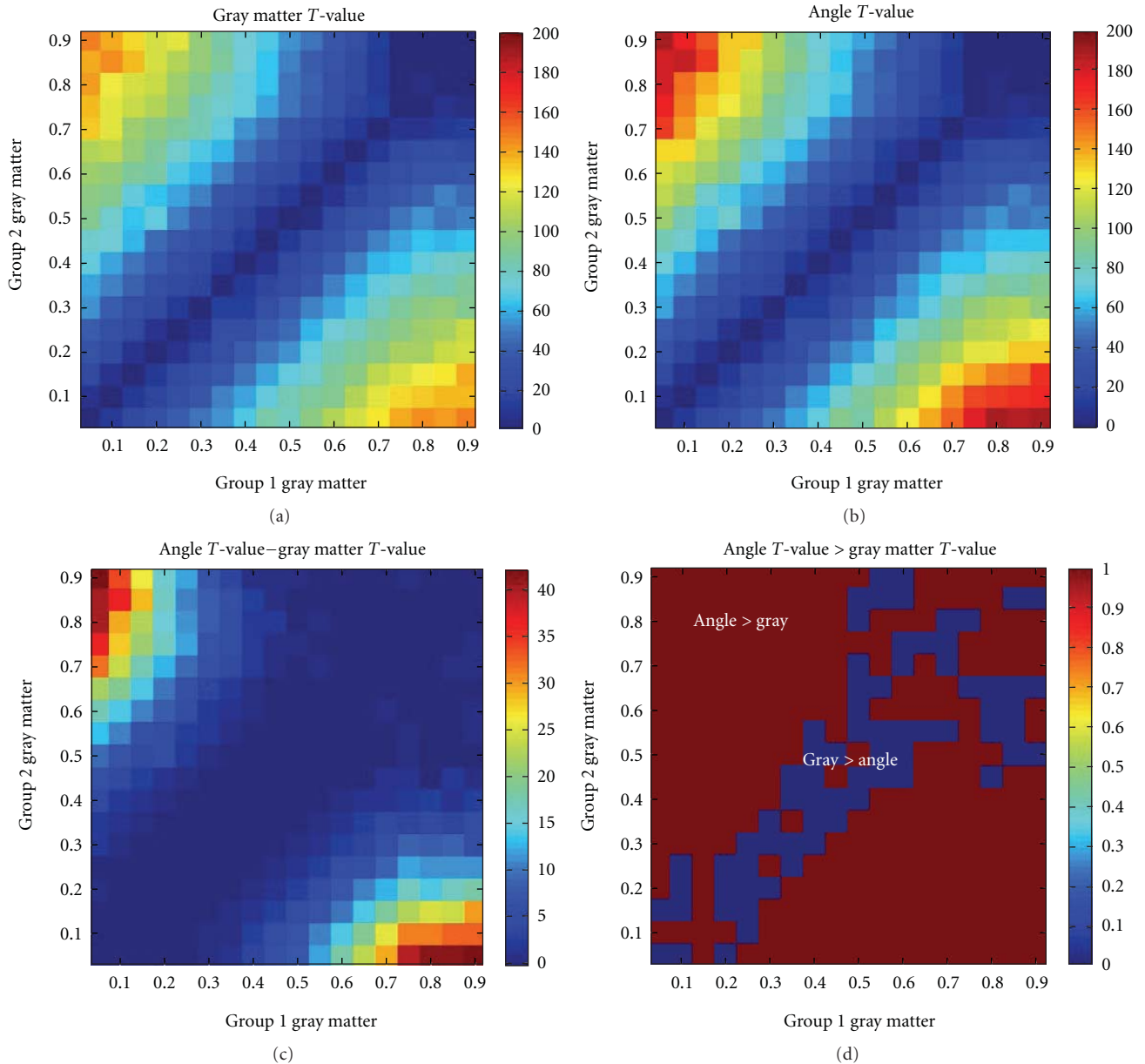


FIGURE 4: Simulation results. Group differences in gray matter or angle for a range of gray matter values from 5% to 100%. (a, b) show group difference  $T$ -values for gray matter and angle, respectively. The patterns are quite similar, although the angle shows generally larger  $T$ -values (see colorbar scales). (c) shows the difference in  $T$ -values. (d) shows that for most combinations of gray matter, the  $T$ -values for angle are larger than those for gray matter (red regions in the image) especially in regions where one group has larger gray matter values and the other has smaller gray matter values.

The analysis of age and gender effects on these sources was also given. For convenience, the sources are listed by a summary of their anatomical regions and represented in order of increasing  $P$  values (decreasing significance). Note that since each source represents a set of regions, the short anatomic label does not fully describe them.

*Angle Source 1: Thalamus.* The most significant angle difference between controls and schizophrenia was in angle source 1. Within this source, the angle value was larger (e.g.,

the white/gray ratio was higher) for patients than controls in thalamus, lingual gyrus, cuneus, precuneus, inferior occipital gyrus, retrolenticular part of internal capsule, fornix, and cingulum.

*Angle Source 2: Right Precentral and Postcentral Gyri.* This source presented the second angle significant difference between healthy controls and patients with controls having lower angle values (e.g., less gray and more white matter) in postcentral gyrus, precentral gyrus, inferior and middle

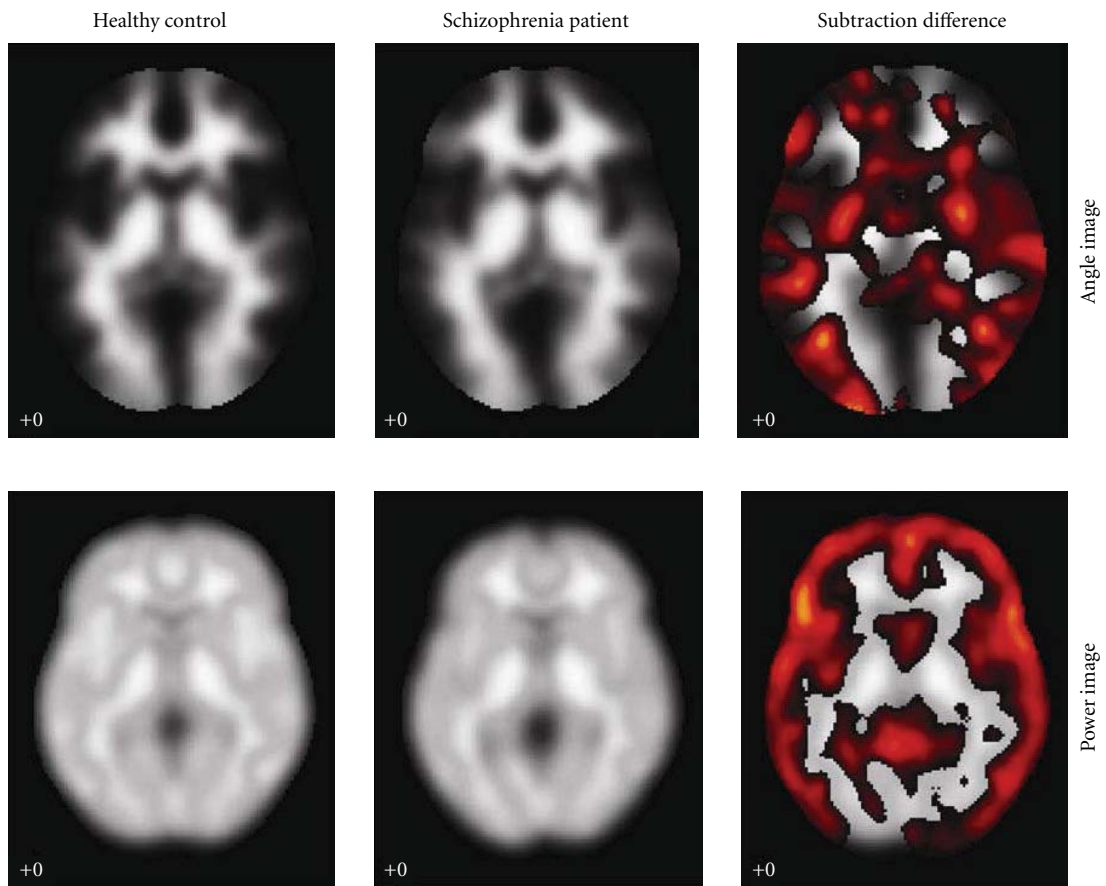
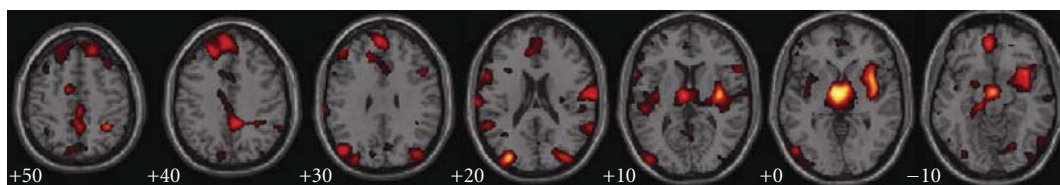
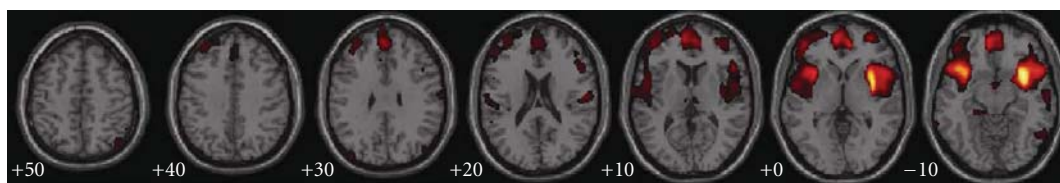


FIGURE 5: Subject differences in angle and power. The upper row consists of angle images and the bottom consists of power images. The first column is the images from healthy control; the second is the images from the schizophrenia patient; the third is the subtraction showing the subject differences.



(a) Group differences in angle



(b) Group differences in power

FIGURE 6: Group differences in angle and power detected by VBM. The regions were thresholded at  $|Z| > 3.0$ .

TABLE 1: Talairach labels for regions detected by VBM. Voxels above a threshold of  $|Z| > 3.0$  were converted from Montreal Neurological Institute (MNI) coordinates to Talairach coordinates and entered into a database to assign anatomic labels for the left (L) and right (R) hemispheres. The concentration of voxels in each area is provided in cubic centimeters (cc). The areas with volume above 1.0 are listed. Within each area, the maximum Z value and its coordinate are provided.

Angle	Brodmann area	L/R volume (cc)	L/R random effects: max $Z(x, y, z)$
Thalamus		6.0/6.7	6.3(1, -13, 2)/6.5(-3, -9, -3)
Insula	13, 47, 41	6.9/2.4	5.9(-1, -7, 2)/4.5(3, -3, -7)
Middle, superior and inferior occipital gyri	19, 37, 18	8.2/11.3	4.6(-31, 4, -17)/5.7(1, -3, -2)
Anterior cingulate	25, 32, 24, 10	1.9/2.8	5.7(1, -15, -3)/4.0(34, 5, -18)
Inferior, superior, medial, and middle frontal gyri	47, 13, 44, 45, 11, 46, 9, 10, 6, 8	32.5/26.9	5.4(7, -6, -5)/5.2(-1, -16, 6)
Clastrum		4.8/1.5	5.2(3, -3, 3)/4.2(-39, -17, 12)
Inferior parietal lobule	40, 39	4.5/2.6	5.0(-7, -43, 42)/4.1(-61, 18, 9)
Cingulate gyrus	31, 24, 32	4.5/6.0	5.0(-15, -76, -14)/4.7(-34, 13, 2)
Parahippocampal gyrus	34, Amygdala, 27, 36, 28, 35, 19	1.9/2.8	5.0(10, -9, 5)/3.9(-27, -15, 12)
Lentiform nucleus		3.7/1.7	4.9(-30, 11, -18)/4.7(3, 51, -9)
Postcentral gyrus	43, 40, 2, 1, 3, 7, 6, 13, 4, 44	6.2/5.0	4.8(-6, -13, -6)/4.5(45, -73, 33)
Cuneus and precuneus	19, 18, 17, 7, 39, 31	9.2/9.1	4.7(9, -4, 42)/4.7(-27, -75, -15)
Angular gyrus	39	1.5/1.1	4.2(-13, -84, -25)/4.7(7, 0, 0)
Supramarginal gyrus	40	2.2/1.3	4.6(-34, 14, -6)/3.6(-4, -25, 3)
Superior, inferior and middle temporal gyri	38, 42, 22, 41, 13, 39, 21, 19, 20, 37	13.4/12.9	4.6(-1, 50, 29)/4.3(-22, 46, 45)
Inferior semilunar lobule		9.1/2.8	4.5(-9, -80, -24)/3.8(-1, -55, 8)
Cerebellar tonsil		11.4/1.1	4.5(-59, -69, -2)/3.5(-7, -10, 10)
Paracentral lobule	31, 6, 5	2.2/0.6	4.3(30, -75, -15)/3.3(9, -66, 46)
Cerebellar vermis		19.5/7.3	5.3(1, -19, 2)/4.3(50, -77, 29)
Lingual gyrus	18, 19	1.9/0.2	4.0(-37, -79, 27)/3.5(67, -44, 20)
Fusiform gyrus	37, 18, 19, 20	3.2/1.5	3.6(39, -7, -19)3.6(-53, -60, -10)
Power	Brodmann area	L/R volume (cc)	L/R random effects: max $Z(x, y, z)$
Clastrum		3.2/3.0	5.8(-34, 5, -9)/4.5(-45, 16, -10)
Inferior, superior, medial and middle Frontal gyri	13, 47, 11, 10, 45, 46, 47, 44, 9, 25, 6, 8	38/59.3	5.6(-34, 13, -3)/4.8(-40, 10, -7)
Insula	13, 40	5.2/4.8	5.6(-36, 1, -3)/5.1(-30, 8, -12)
Superior temporal gyrus	38, 22, 41, 13	14.3/16.6	5.0(-37, -3, 2)/4.3(-45, -15, -41)
Inferior semilunar lobule		9.1/3.5	4.6(-52, 14, -7)/3.8(-34, 54, -3)
Parahippocampal gyrus	34, Amygdala, 36, 35, 27, 30	0.9/1.7	4.5(30, 29, -23)/4.1(6, 54, 6)
Middle and inferior temporal gyri	21, 38, 39, 37, 19, 20, 25	6.7/5.0	4.4(-25, 14, -15)/3.7(-22, -79, -33)
Cerebellar tonsil		2.4/1.1	4.2(24, 28, -24)/3.4(-3, 54, 22)
Anterior cingulate	32, 25	1.9/1.9	3.6(3, 46, -6)/3.9(-22, -59, -46)
Cerebellar vermis		6.4/4.9	4.3(-36, 2, 5)/4.1(-49, 9, -2)
Precentral and postcentral gyri	3, 7, 43, 40, 1, 44, 6, 13	6.9/5.4	3.7(-33, -72, -39)/3.6(-6, 44, 1)

TABLE 2: White matter labels for regions detected by VBM. Voxels above a threshold of  $|Z| > 3.0$  were converted from Montreal Neurological Institute (MNI) coordinates to the ICBM DTI-81 coordinates and entered into a database to assign anatomic labels. The volume of significant white matter voxels within each fiber tract area is provided in cubic centimeters (cc). The areas with volume above 0.1 are listed. The percentage of the fiber tract containing significant white matter voxels is also provided. Within each fiber tract, the maximum Z value and its coordinate are provided.

Angle	L/R volume (cc)	L/R percentage (%)	L/R max $Z(x, y, z)$
Anterior limb of internal capsule	0.07/0.51	2.14/22.69	4.27(9, 0, 2)/5.53(-9, -6, -3)
Posterior limb of internal capsule	0.63/0.09	16.61/2.94	6.17(8, -5, 0)/4.52(-11, 0, 2)
Retrolenticular part of internal capsule	0.25/1.40	10.05/36.40	3.87(-29, -20, 12)/5.42(-9, -5, 0)
Posterior corona radiata	0.16/na	4.23/na	3.72 (-18, -45, 41)/na
External capsule	2.36/0.31	66.20/8.70	5.50 (-36, -9, 6)/3.41 (32, 8, 3)
Cingulum (cingulate gyrus)	0.26/0.23	9.74/9.87	3.41 (-8, 20, 30)/3.80 (6, -11, 42)
Cingulum (hippocampus)	na/0.35	na/27.81	na/3.92(20, -29, -8)
Inferior frontooccipital fasciculus	1.37/0.03	72.42/1.41	5.00(-36, 3, -3)/3.09(29, 6, -3)
Uncinate fasciculus	0.37/0.06	100/16.8	4.46(-39, 0, -15)/3.60(35, 3, -20)
Power	L/R volume (cc)	L/R percentage (%)	L/R max $Z(x, y, z)$
External capsule	0.88/0.36	10.42/24.72	5.69(-35, 8, -2)/4.28(32, 11, -2)
Cingulum (hippocampus)	na/0.13	na/10.96	na/3.60(23, -30, -12)
Inferior frontooccipital fasciculus	1.22/0.55	0.6478/28.87	5.99(-35, 8, -8)/4.26(32, 11, -3)
Uncinate fasciculus	0.31/0.35	83.64/92.92	5.42(-35, 3, -11)/4.12(33, 6, -11)

frontal gyri. The distribution lays particular emphasis on the right hemisphere with much larger volume and maximum value.

*Angle Source 3: Parietal Lobe.* This source included regions of cuneus, precuneus, and superior parietal lobule with lower gray-to-white matter ratios in patients than controls.

*Angle Source 4: Left Precentral and Postcentral Gyri.* This source showed significant difference between controls and patients, with controls having less gray and relatively more white matter partition in postcentral gyrus, precentral gyrus, superior and middle frontal gyri. The regions of both angle sources 2 and 4 mainly involve prefrontal and postfrontal gyri, with angle source 4 distributing more to the left hemisphere and angle source 2 more to the right hemisphere.

*Angle Source 5: Right Cuneus with Frontal Lobe.* More gray and less white matter partitions in healthy controls than patients were found in this source, which included middle and superior frontal gyri and the right cuneus.

*Angle Source 6: Left Cuneus with Frontal Lobe.* This also showed a significant angle difference between controls and patients, with controls having more gray matter partition in middle frontal gyrus, left lingual gyrus, and left cuneus. Both

angle source 5 and 6 occur mainly in cuneus and middle frontal gyrus, with angle sources 5 emphasizing the right and source 6 emphasizing the left cuneus.

*Power Source: Bilateral Temporal Gyrus.* The most significant source showing average concentration differences between the diagnostic groups was found in bilateral superior temporal gyri, insula, anterior cingulate, medial and inferior frontal gyri, cingulum, and uncinate fasciculus. Healthy controls consistently showed more average gray and white matter concentration than patients.

*Age and Gender Effects.* There was no significant effect of gender on any source. There was a significant effect of age on all sources at  $P < 0.005$ . The correlation plots of age versus ICA weights for the sources are presented in Figure 8. The ICA weight increases as age increases of all the angle sources according to the linear trend. For angle sources 1, 4, 5, and 6, the intercept value of controls is higher than that of patients, and the slope values of controls and patients are nearly identical. For angle source 2, the intercept value of controls is higher than that of patients, and the slope value of controls and patients are nearly the same. For angle 3, the intercept value of controls is higher than that of patients, and the slope value of controls is slightly lower than that of patients. For the power source, the ICA weight decreases as age

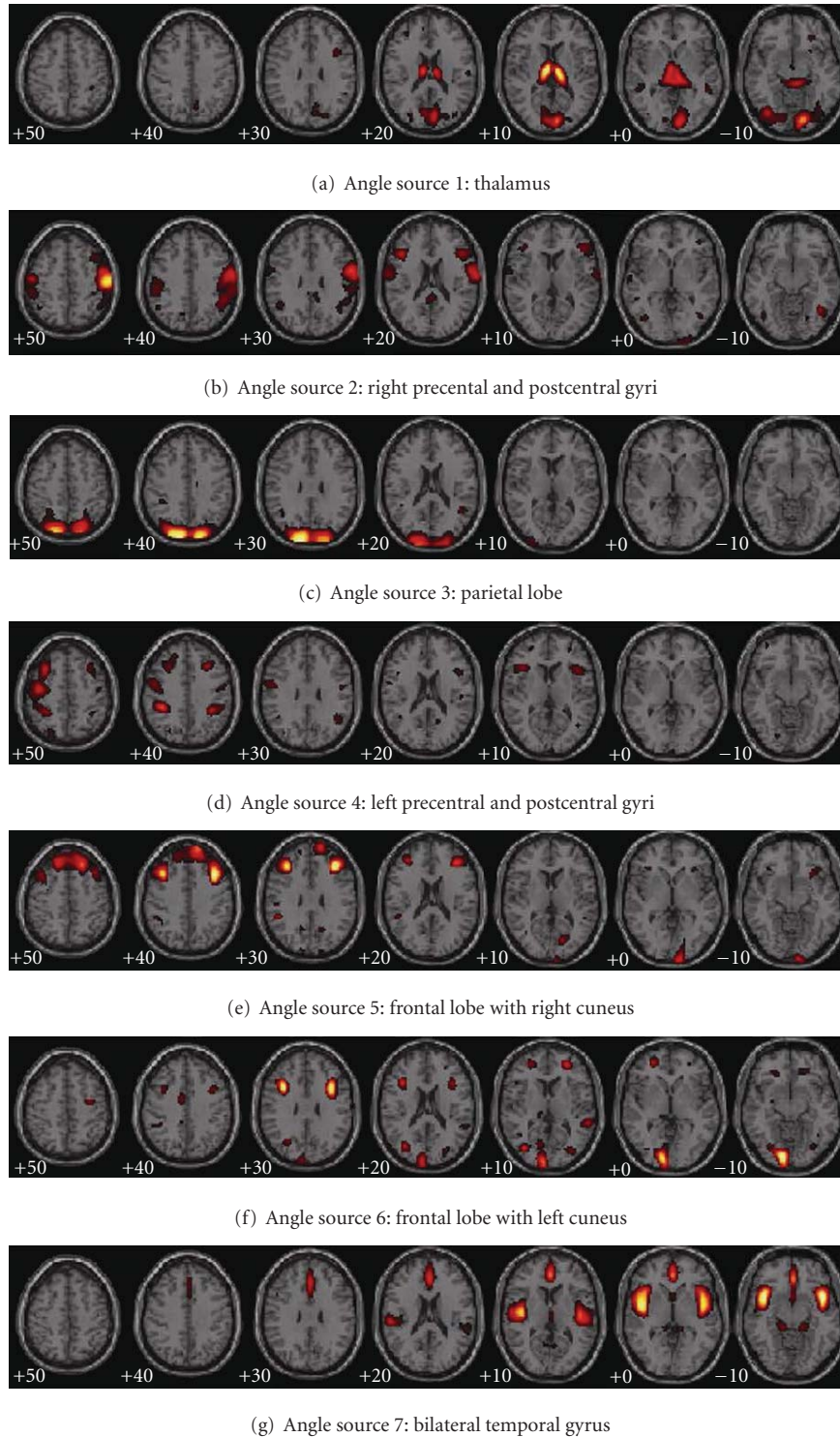


FIGURE 7: Angle and power networks detected by SBM. Six angle networks showing significant gray-to-white matter ratio abnormalities and one power network, showing significant average concentration reduction, were shown. The regions were thresholded at  $|Z| > 3.0$ .

increases. According to the linear trend, the intercept value of the controls is higher than that of patients and the negative slope value of the controls is slightly lower than that of the patients. After removing effects of age and gender, the group differences in the sources remained significant.

#### 4. Discussion

To our knowledge, this is the first study to extract interrelated features of gray and white matter for brain structural analysis. Three different analyses were applied to the angle and

TABLE 3: Talairach labels for networks detected by SBM. Voxel above a threshold of  $|Z| > 3.0$  were converted from Montreal Neurological Institute (MNI) coordinates to Talairach coordinates and entered into a database to assign anatomic labels for the left (L) and right (R) hemispheres. The concentration of voxels in each area is provided in cubic centimeters (cc). The areas with volume above 1.0 are listed. Within each area, the maximum Z value and its coordinate are provided.

	Brodmann area	L/R volume (cc)	L/R random effects: max $Z(x, y, z)$
<i>Angle source 1:</i>			
Thalamus		13.2/12.5	16.7(-10, -13, 12)/15.7(10, -15, 12)
Lingual gyrus	18, 17, 19	3.5/11.4	5.9(-16, -80, -2)/11.2(13, -83, -3)
Cuneus	18, 17, 30, 19, 7, 23	8.6/11.7	7.4(0, -84, 17)/10.4(7, -85, 11)
Inferior and middle occipital gyri	17, 19, 18, 37	8.0/5.4	7.4(-39, -73, -5)/9.3(13, -88, -7)
Culmen		1.3/1.7	7.8(-3, -32, -5)/8.2(3, -34, -5)
Precuneus	31, 7, 19	1.7/4.5	5.8(-9, -72, 23)/7.4(6, -73, 22)
Caudate		1.3/0.4	6.6(-7, -2, 15)/4.7(18, -24, 18)
Superior, Inferior and middle frontal gyri	6, 47, 11, 9, 10	2.8/7.3	6.3(-19, -11, 72)/5.4(25, 21, -16)
Parahippocampal gyrus	27, 35, 30, 36, 28	0.9/2.2	4.8(-15, -29, -6)/6.0(12, -34, -1)
Middle temporal gyrus	22, 21, 19, 39	1.3/1.7	4.6(-52, -41, 5)/5.3(49, -38, 1)
Fusiform gyrus	19, 18, 37	1.3/1.1	4.5(-39, -73, -10)/3.6(27, -84, -12)
Postcentral gyrus	3, 5	0.6/1.1	3.2(-27, -39, 66)/4.1(33, -31, 69)
<i>Angle source 2:</i>			
Postcentral gyrus	3, 1, 2, 43, 40, 5, 7	11.0/21.2	9.9(-53, -17, 60)/15.5(55, -15, 55)
Precentral gyrus	6, 4, 43, 44, 9	8.0/22.5	5.9(-53, -7, 56)/12.3(52, -10, 57)
Inferior and middle frontal gyri	9, 45, 44, 46, 13, 6, 8	6.3/23.1	7.4(-45, 24, 17)/8.2(58, 4, 23)
Inferior and superior parietal lobules	40, 7	5.8/12.9	6.1(-53, -31, 43)/5.4(49, -39, 39)
Middle and inferior occipital gyri	18, 37, 19	3.3/1.3	6.0(-27, -103, 7)/4.8(39, -68, 2)
Insula	13	0.2/0.4	4.9(-39, 24, 17)/5.9(40, 23, 17)
Supramarginal gyrus	40	0.9/2.8	4.6(-48, -49, 31)/5.9(46, -43, 37)
Cuneus	18, 19	2.4/na	5.7(-16, -104, 11)/na
Posterior cingulate	23, 30, 29	2.2/0.9	5.6(0, -38, 23)/4.7(4, -35, 25)
Inferior and superior temporal gyri	19, 20, 37, 22, 42, 39, 41	3.5/4.3	5.1(-48, -63, -4)/4.7(40, -66, -3)
Fusiform gyrus	37, 19, 20, 18	1.7/1.1	4.9(-40, -54, -7)/4.1(42, -62, -7)
Superior frontal gyrus	8, 11	na/1.7	na/4.4(40, 18, 47)
Orbital gyrus	11, 47	0.9/1.9	3.5(-16, 23, -29)/4.0(7, 45, -30)
<i>Angle source 3:</i>			
Cuneus	19, 18, 7	13.4/11.9	16.9(-19, -90, 39)/13.2(16, -90, 36)
Precuneus	19, 7, 31, 39	16.2/14.9	16.2(-21, -85, 43)/15.4(16, -88, 42)
Superior parietal lobule	7, 5	11.2/10.2	11.7(-19, -69, 57)/9.0(15, -70, 59)
Middle and superior occipital gyri	18, 19	6.5/3.3	10.5(-21, -98, 24)/7.1(27, -96, 24)
Inferior and superior temporal gyri	20, 22, 13, 39	5.4/2.2	8.1(-50, -23, -33)/5.7(52, -26, -31)
Superior frontal gyrus	11, 10	2.8/1.5	8.0(-7, 58, -27)/4.4(22, 70, -1)
Rectal gyrus	11	1.7/0.9	7.2(-1, 23, -29)/6.2(4, 25, -29)
Fusiform gyrus	20	2.6/1.5	6.3(-59, -19, -29)/5.8(58, -26, -30)
Postcentral gyrus	7, 3, 5, 2, 4	5.8/1.5	5.4(-15, -55, 65)/4.3(4, -40, 66)
Inferior parietal lobule	7, 39, 40	2.2/na	4.9(-39, -66, 45)/na
<i>Angle source 4:</i>			
Precentral gyrus	6, 4, 44, 9	20.7/6.0	19.3(-39, -7, 61)/5.4(36, -9, 57)
Middle and superior frontal gyri	6, 8, 9, 11, 46, 10	26.4/6.5	15.7(-33, -7, 61)/7.9(28, 24, 38)
Inferior parietal lobule	40	7.1/4.1	11.1(-39, -34, 39)/8.4(33, -39, 39)
Postcentral gyrus	3, 5, 2, 1	8.0/0.4	10.2(-48, -19, 64)/3.1(48, -30, 35)
Insula	13	0.4/2.6	5.6(-34, 21, 9)/6.7(40, 18, 9)

TABLE 3: Continued.

	Brodmann area	L/R volume (cc)	L/R random effects: max $Z(x, y, z)$
Inferior and medial frontal gyri	13, 44, 45, 9, 47, 6, 25	4.8/3.6	6.7(-40, 21, 7)/6.0(45, 15, 12)
Precuneus	7, 31, 19	1.7/0.4	4.9(-22, -81, 50)/5.9(30, -43, 42)
Inferior semi-lunar lobule		3.0/na	5.9(-45, -71, -46)/na
Cerebellar tonsil		1.7/na	5.6(-48, -65, -46)/na
Superior parietal lobule	7	1.3/na	5.2(-27, -69, 46)/na
cuneus	18, 17	1.1/1.1	4.5(-1, -103, 4)/4.6(1, -103, 9)
<i>Angle source 5:</i>			
Middle and superior frontal gyri	9, 10, 8, 46, 6, 11	39.6/46.9	10.0(-39, 25, 32)/11.5(34, 33, 25)
Precentral gyrus	9	0.6/1.3	9.0(-39, 21, 36)/11.1(36, 22, 35)
Cuneus	17, 18, 23, 30, 19	1.9/9.3	4.1(-13, -93, 35)/7.3(18, -72, 9)
Medial and inferior frontal gyri	9, 8, 11, 6, 47, 48	5.0/7.6	4.5(-1, 47, 42)/6.2(9, 50, 36)
Rectal gyrus	11	1.5/1.5	5.0(-3, 29, -29)/5.9(3, 29, -28)
Lingual gyrus	18, 17	0.2/2.2	3.5(-25, -59, 8)/5.7(7, -102, -9)
Inferior parietal lobule	40	2.2/na	5.6(-50, -39, 28)/na
Orbital gyrus	11	0.6/1.9	4.0(-3, 35, -31)/4.9(9, 51, -28)
Inferior temporal gyrus	20, 21	1.1/0.4	4.1(-61, -23, -17)/3.3(50, -11, -20)
<i>Angle source 6:</i>			
Lingual gyrus	17, 18, 19	10.2/0.9	12.8(-15, -86, -2)/4.6(30, -73, -4)
Middle and inferior frontal gyri	9, 46, 10, 11, 6, 8, 47, 45	8.4/10.1	10.6(-36, 13, 28)/11.6(34, 14, 27)
Orbital gyrus	11, 47	0.2/4.1	3.1(-18, 25, -23)/10.2(15, 37, -22)
Cuneus	17, 18, 19, 30, 23, 7	13.8/1.5	9.6(-12, -91, 6)/4.3(16, -71, 9)
Parahippocampal gyrus	36, 35, 28, Hippocampus, 30, Amygdala	4.3/2.4	9.3(-25, -20, -28)/7.0(21, -22, -29)
Precentral gyrus	9, 6, 4	1.7/2.6	7.5(-33, 9, 31)/9.1(36, 13, 32)
Rectal gyrus	11	na/1.9	na/8.1(10, 40, -20)
Middle occipital gyrus	18, 19	3.7/0.9	8.0(-12, -90, 13)/5.6(33, -76, 15)
Middle and superior temporal gyri	39, 19, 21, 22, 37, 13, 41, 42	3.9/4.1	7.8(-34, -72, 17)/6.0(56, -39, 13)
Superior and medial frontal gyri	10, 11, 6, 25, 9	2.4/4.8	7.5(-27, 48, 2)/5.9(24, 48, 3)
Cerebellar tonsil		16.4/6.7	7.5(-28, -47, -37)/6.4(25, -38, -31)
Cerebellar vermis		3.2/3.0	7.3(-21, -18, -31)/7.6(24, -26, -31)
Insula	13	0.9/1.1	7.3(-37, 18, 18)/4.7(50, -39, 13)
Cingulate gyrus	24, 31	1.7/na	5.7(-10, -2, 39)/na
Precuneus	31, 7, 19	0.9/1.1	4.1(-25, -62, 34)/4.5(28, -76, 19)
Posterior cingulate	30	1.1/0.6	4.5(-28, -71, 16)/3.8(18, -65, 7)
Postcentral gyrus	3, 5, 1, 2	1.7/1.1	4.4(-42, -23, 67)/3.6(71, -16, 26)
Inferior parietal lobule	40	1.5/0.2	4.2(-42, -39, 38)/3.2(52, -48, 54)
Thalamus		1.3/na	4.1(-16, -27, 7)/na
<i>Power source:</i>			
Insula	13, 40, 41, 22	8.2/10.8	11.0(-45, 7, 0)/13.8(43, 10, -7)
Superior and transverse temporal gyri	22, 38, 13, 41, 42	17.0/15.7	13.8(-46, 7, -5)/13.2(45, 4, -5)
Inferior and medial frontal gyri	47, 13, 45, 9, 11, 10, 6, 25, 8	20.1/12.1	12.6(-46, 13, -4)/12.2(42, 16, -8)
Precentral and postcentral gyri	6, 13, 44, 43, 40	5.6/2.4	12.2(-46, -7, 6)/5.5(53, -6, 6)
Anterior cingulate and cingulate gyrus	32, 24, 25, 10	11.0/3.9	9.0(-1, 42, 2)/6.1(4, 44, 3)
Clastrum		0.9/1.7	5.2(-37, -10, 7)/5.8(37, -13, 8)
Parahippocampal gyrus	30, 35, 34, 27, 28, 36, Amygdala	3.5/3.9	5.4(-15, -32, -5)/5.4(13, -34, -3)
Inferior parietal lobule	40	1.1/0.2	5.0(-61, -24, 23)/3.1(55, -31, 22)
Thalamus		1.9/0.6	4.7(0, -17, 6)/3.2(15, -33, 2)
Cerebellar vermis		2.8/3.2	4.4(-21, -34, -13)/5.9(24, 5, -22)

TABLE 4: White matter labels for networks detected by SBM. Voxels above a threshold of  $|Z| > 3.0$  were converted from Montreal Neurological Institute (MNI) coordinates to the ICBM DTI-81 coordinates and entered into a database to assign anatomic labels. The volume of significant white matter voxels within each fiber tract area is provided in cubic centimeters (cc). The areas with volume above 0.1 are listed. The percentage of the fiber tract containing significant white matter voxels is also provided. Within each fiber tract, the maximum Z value and its coordinate are provided.

Angle source 1	L/R volume (cc)	L/R percentage (%)	L/R max $Z(x, y, z)$
Fornix (column and body of fornix)	0.38	62.64	7.15(-3, -4.5, 13.5)
Retrolenticular part of internal capsule	na/0.73	na/19.04	na/6.71(-10.5, -4.5, 6)
Superior cerebellar peduncle	0.18/na	19.22/na	6.52(6, -33, -12)/na
Cingulum (hippocampus)	0.114/0.44	9.71/34.76	4.25(-18, -31.5, -7.5)/6.32(18, -33, -3)
Cerebral peduncle	0.29/0.10	12.83/10.25	6.31(12, -25.5, -6)/5.11(-6, -33, -12)
Fornix (cres)/Stria terminalis	0.003/0.17	0.30/16.24	3.16(-21, -31.5, 12)/6.28(19.5, -30, 12)
Posterior limb of internal capsule	0.49/0.02	12.90/0.55	5.97(16.5, -15, 9)/3.73(-10.5, 0, 7.5)
Anterior limb of internal capsule	na/0.22	na/9.55	na/5.01(-13.5, -25.5, -6)
b	L/R volume (cc)	L/R percentage (%)	L/R max $Z(x, y, z)$
Splenium of corpus callosum	1.75	13.70	5.41(0, -39, 22.5)
Angle source 4	L/R volume (cc)	L/R percentage (%)	L/R max $Z(x, y, z)$
Superior longitudinal fasciculus	0.47/0.21	7.21/3.20	7.68(-39, -33, 37.5)/5.61(31.5, -40.5, 36)
Angle source 5	L/R volume (cc)	L/R percentage (%)	L/R max $Z(x, y, z)$
Middle cerebellar peduncle	0.39	2.48	3.87(-24, -61.5, -30)
Angle source 6	L/R volume (cc)	L/R percentage (%)	L/R max $Z(x, y, z)$
Superior longitudinal fasciculus	0.29/0.49	4.43/7.31	8.89(-34.5, 12, 25.5)/8.60(31.5, 9, 28.5)
Middle cerebellar peduncle	1.18	7.52	5.74(25.5, -40.5, -37.5)
Cingulum (cingulate gyrus)	0.56/na	21.15/na	5.61(-10.5, -4.5, 40.5)/na
Cingulum (hippocampus)	0.13/na	11.47/na	5.10(-27, -19.5, -24)/na
Superior corona radiata	0.12/0.02	1.63/0.32	4.67(-28.5, 12, 28.5)/3.63(27, 7.5, 28.5)
Power source	L/R volume (cc)	L/R percentage (%)	L/R max $Z(x, y, z)$
Cingulum (hippocampus)	0.46/0.36	40/28.6	5.08(-18, -31.5, -9)/4.91(18, -30, -10.5)
Uncinate fasciculus	0.04/0.08	10/22.12	4.30(-39, 0, -15)/5.22(36, 3, -15)

power images. A single-subject subtraction highlighted the interrelated tissue distribution differences at the individual subject level. A univariate VBM analysis detected group level differences between healthy controls and schizophrenias, which offered statistical maps of fused gray and white matter abnormalities. A multivariate SBM analysis further filtered the noise and determined several networks showing group differences. We also evaluated age and gender effects on the networks.

*4.1. Tissue Distribution Showing Subject Differences.* The angle and power images emphasize the interrelated gray and white matter concentration. The angle image reflects the gray-to-white matter ratio and is sensitive to small changes in regions where gray matter is increasing and white matter is decreasing (or changing little), or vice versa. The power image indicates overall tissue concentration and highlights tissue presence in each voxel, especially in regions where both gray and white matter concentrations are low. Subtraction of angle/power images between healthy controls and schizophrenia patients shows tissue distribution differences

between two subjects. Results suggest richer information showing that such differences can be captured by the angle and power images. The angle value differentiation showed a smaller gray-to-white matter in patients versus controls in a wide range of areas of both gray and white matters. Power images also revealed patient/control differences in the superior temporal gyrus, suggesting that both gray and white matters are lower in this region in patients.

One of the key advantages of our approach is the ability to evaluate changes in both gray and white matters through the structural angle and power images. This provides a complementary approach to methods which work only with gray matters images. In addition, the simulation we performed suggests increased sensitivity to group changes over an approach which uses only the gray matter images. Comparison with a previous paper in which we analyzed the gray matter images with both VBM and SBM highlights the complementary nature of our proposed approach. In [22], we identified multiple SBM sources which showed group differences in patients and controls. Five sources were identified as summarized in Table 5. Though an exact match was not possible,

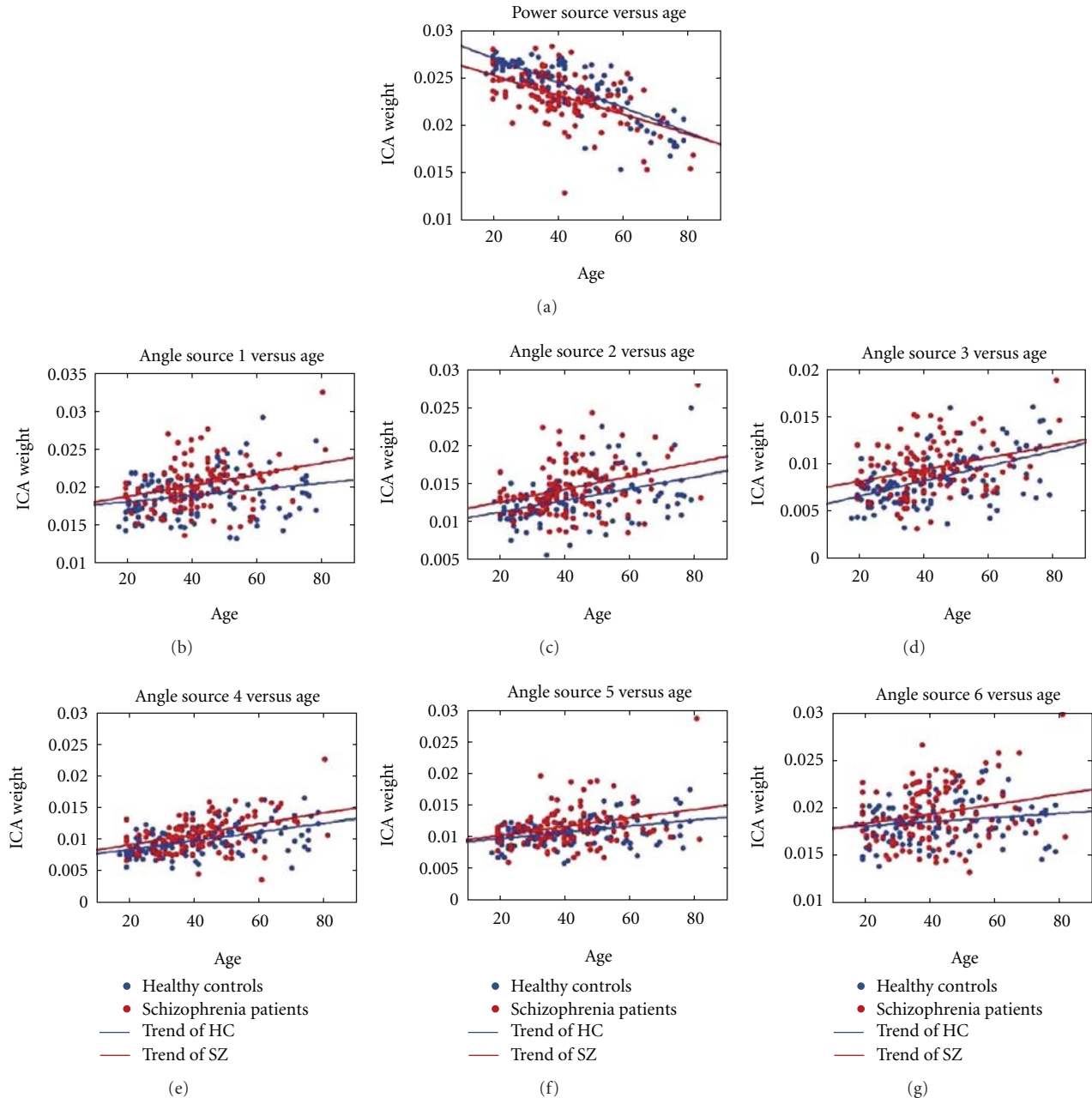


FIGURE 8: The correlation plots between age and ICA weights for angle and power sources. Red dots: correlation for the patients; blue dots: correlation for the controls; red line: trend for red dots; blue line: trend for blue dots.

since there are some differences in the regions included in the sources, an approximate match is provided in the table. We can see from this that all but one of the sources were identified in the angle and power analyses we performed in the current paper. The basal ganglia region was identified in the gray matter analysis but not the angle or power analysis. As discussed in [22], the SBM approach has some important advantages over voxel-based approaches since it groups regions which have common intersubject covariation together. In addition, noise sources are typically separated into separate sources, thus providing a sort of spatial filter to

clean up the remaining sources. In this paper, we proposed a transformation of the gray matter data into structural angle and power images. This approach has some advantages and in particular appears to be more sensitive to subtle group differences, especially where one group has high gray matter values and the other group has low gray matter values. This also includes, but is not limited to, regions where boundaries between gray matter and white matter are shifted in the two groups (e.g., where the gray matter in one group drops off faster than that in the other group). However, our approach should be seen as a complementary approach; not meant to

TABLE 5: Comparison of results with previous SBM analysis.

Region	SBM of gray matter [22]	SBM of angle	SBM of power
Bilateral temporal lobe	X		X
Thalamus	X	X	
Basal ganglia	X		
Frontal 1	X	X	
Parietal	X	X	
Frontal 2		X	
Right precentral		X	
Left precentral		X	

replace analyses of gray or white matter separately. Next, we summarize and discuss the findings in the current analysis in more detail.

*4.2. Tissue Distribution Showing Group Differences.* The VBM analysis identifies group level differences of tissue distribution by voxel-by-voxel comparison. Results indicated that white matter concentration was higher and gray matter concentration was lower in the thalamus in schizophrenia. This is consistent with previous work showing thalamic gray matter reductions [17]. Changes in the insula, which received projects from the thalamus, is also in agreement with a previous report [31]. The findings of greater white-to-gray matter in superior and middle frontal gyri was consistent with the gray matter reduction in these regions [11]. The disruption of uncinate and inferior frontal-occipital fasciculi is consistent with previous reports [32, 33] as these association fibers project to the smaller cortical regions. In addition, the results also suggest a disturbance in cuneus and precuneus underlying the disease. We also showed changes in the internal capsule that also receives thalamic projections.

Regions showing significant differences in gray and white matter average concentration also revealed a large continuous region of temporal lobe that included the bilateral superior temporal gyrus, planum temporale, transverse temporal gyrus, and insula, but little of middle or inferior temporal regions, consistent with previous reports of selective gray matter reductions in the temporal gyrus [13, 34]. Also the concentration disruption in medial and superior frontal gyri agrees with previous findings of gray matter reduction in sMRI studies [11]. Our findings also suggest that the claustrum and external capsule should be further studied as they play an important role in cortico-cortical connections.

*4.3. Tissue Distribution Showing Network Abnormalities.* The SBM analysis enables evaluation of maximally independent features which also show similar intersubject covariation which differ in degree between patients and controls. Consistent with our simulation, the structural angle feature identified the most sources showing group differences. The power angle identified an important previously identified network in which both groups have larger gray matter values. We now discuss the difference sources in more detail.

Angle source 1 suggested the abnormality of a thalamic structural network in schizophrenia. The higher thalamic white-to-gray ratio detected by SBM confirmed the evidence detected by the VBM analysis. The smaller cuneus and lingual gyrus angle agree with the lesser occipital lobe gray matter reported by others [35] and abnormalities in fornix and cingulum are also consistent with previous studies [36, 37]. Our findings suggested that the posterior thalamic projection which penetrates the retrolenticular part of internal capsule and connects to the occipital lobe through cingulum was abnormal in patients. We also suggested that the anterior thalamic projection might be affected by the fornix disruption.

Angle sources 2 and 4 were two networks comprising tissue distribution disturbances in right and left hemispheres sensory-motor cortex, respectively. The smaller gray matter partition of precentral and postcentral gyri in patients is consistent with previous studies [38, 39]. Since postcentral gyrus contains the main sensory receptive area of primary somatosensory cortex and the dorsal part of the precentral gyrus is the location of primary motor cortex, these two angle sources looked similar to a functional sensory motor pattern, one containing the left hemisphere and the other the right. Our findings suggest that these two structural sources in precentral and postcentral gyri might underlie sensory-motor disturbances in schizophrenia and that structural information associated with functional areas might be identified by these tissue distributions.

Angle source 3 was mainly located in parietal lobe. Our finding of less gray-to-white matter ratio in parietal cortex is consistent with a previous report of more regional white matter and less gray matter in schizophrenia [9]. Since cuneus, precuneus, and parietal lobule are all involved in basic visual processing [40], the structural distribution abnormality might be related to the observed disturbances in the visual stream.

Angle sources 5 and 6 were two networks focusing on frontal lobe and cuneus. The lower gray-to-white matter ratio of patients in middle frontal gyrus and cuneus agrees with previous reports [32, 41, 42]. Our findings suggest that there might be connectivity between cuneus and frontal cortex, disturbances reflecting an abnormal working memory network.

The power source showed regions consistently identified as disrupted in schizophrenia. Since the uncinate fasciculus

connects the frontal and temporal lobes and the cingulum bundle collects projections from the nearby cingulate gyrus and extends into the temporal lobe, this circuit can be considered a local area network describing frontal-temporal connectivity. Our findings agree with previous studies of frontotemporal connections [43, 44], providing supportive evidence for the disconnection hypothesis of schizophrenia.

All sources were maximally spatially independent and each revealed one network that differed significantly in schizophrenia versus controls. By examining the Talairach table and the figure of sources, some regions were shared by several sources. These overlapping regions corresponded to different structural connectivities, with patterns suggesting disruptions in higher cortical functions that appeared to be most disturbed in schizophrenia patients. For example, the lingual gyrus was shared by angle sources 1 and 6, which was part of the disturbance in both the thalamic network and cuneus network; the cingulum appears in angle source 1 and power source, which was frequently found to be structurally or functionally altered in individuals with schizophrenia [36, 45]; the middle and medial frontal gyri were in angle sources 2, 4, 5, and 6, which indicated the multifunctional roles of prefrontal cortex; the precuneus was observed in all of the angle sources, consistent with its participation in multiple functions [46] and it was likely that this region may serve as a hub of multiple naturally grouped networks.

Subject-specific loading parameters for all sources were significantly correlated with age in this cross-sectional study. For angle source 1, 4, 5, and 6, the intercept suggested that the white-to-gray matter ratios of patients and controls were similar at younger ages. However, in patients this ratio increased faster than controls with increasing age. At older ages, the gray matter partition in patients was smaller than in controls, and the white matter partition increases more in patients than in controls. For angle source 2, the white-to-gray matter ratio of patients was larger than that of controls and increases with age. For angle source 3, the intercept and slope suggested that the white-to-gray matter ratio of patients was larger than of controls at earlier ages, however, it declined faster than controls with increasing age. By age 75, the ratio reached a similar size for both patients and controls. For the power source, the average concentration in patients was less than that in controls at earlier ages and continued to decline with increasing age. At older ages, the concentration in patients and controls reached the same level.

## 5. Conclusion

In this paper, we demonstrate an approach to extract features by combining gray and white matter information in two different ways. The angle image reflects the partitions of gray and white matter within each voxel and the power image indicates the average tissue concentration. Both of them naturally capture interrelated changes in tissue distribution and are sensitive to the small changes in regions where gray and white matter concentrations are low. Three different analyses, single-subject subtraction, VBMs and SBMs were applied to the angle and power images separately to explain

the utilization of the structural angle and power images in schizophrenia and to evaluate the efficiency of the features for interrelated gray and white matter fusion. These initial experiences with structural angle and power images revealed several interesting findings in schizophrenia that were not identified by standard, separate gray or white matter analyses and demonstrate the usefulness of angle and power joint gray and white matter assessment.

## Acknowledgments

This study was funded by the National Institutes of Health grants: 1 R01 EB 000840 and 1 R01 EB 005846 (to V. Calhoun) and 2 RO1 MH43775 MERIT Award, 5 RO1 MH52886, and a NARSAD Distinguished Investigator Award (to G. Parolson).

## References

- [1] U. W. Preuss, T. Zetzsche, M. Jäger et al., "Thalamic volume in first-episode and chronic schizophrenic subjects: a volumetric MRI study," *Schizophrenia Research*, vol. 73, no. 1, pp. 91–101, 2005.
- [2] S. A. Mitelman, A. M. Brickman, L. Shihabuddin et al., "A comprehensive assessment of gray and white matter volumes and their relationship to outcome and severity in schizophrenia," *NeuroImage*, vol. 37, no. 2, pp. 449–462, 2007.
- [3] E. A. Hazlett, M. S. Buchsbaum, M. M. Haznedar et al., "Cortical gray and white matter volume in unmedicated schizotypal and schizophrenia patients," *Schizophrenia Research*, vol. 101, no. 1–3, pp. 111–123, 2008.
- [4] A. Pfefferbaum, D. H. Mathalon, E. V. Sullivan, J. M. Rawles, R. B. Zipursky, and K. O. Lim, "A quantitative magnetic resonance imaging study of changes in brain morphology from infancy to late adulthood," *Archives of Neurology*, vol. 51, no. 9, pp. 874–887, 1994.
- [5] D. Cicchetti and D. Cohen, *Developmental Psychopathology*, vol. 2 of *Developmental Neuroscience*, John Wiley & Sons, New York, NY, USA, 2006.
- [6] I. C. Wright, P. K. McGuire, J. B. Poline et al., "A voxel-based method for the statistical analysis of gray and white matter density applied to schizophrenia," *NeuroImage*, vol. 2, no. 4, pp. 244–252, 1995.
- [7] T. Schneider-Axmann, T. Kamer, M. Moroni et al., "Relation between cerebrospinal fluid, gray matter and white matter changes in families with schizophrenia," *Journal of Psychiatric Research*, vol. 40, no. 7, pp. 646–655, 2006.
- [8] S. A. Mitelman, M. S. Buchsbaum, A. M. Brickman, and L. Shihabuddin, "Cortical intercorrelations of frontal area volumes in schizophrenia," *NeuroImage*, vol. 27, no. 4, pp. 753–770, 2005.
- [9] S. A. Mitelman, E. L. Canfield, R. E. Newmark et al., "Longitudinal assessment of gray and white matter in chronic schizophrenia: a combined diffusion-tensor and structural magnetic resonance imaging study," *The Open Neuroimaging Journal*, vol. 3, pp. 31–47, 2009.
- [10] L. Xu, G. Pearlson, and V. D. Calhoun, "Joint source based morphometry identifies linked gray and white matter group differences," *NeuroImage*, vol. 44, no. 3, pp. 777–789, 2009.
- [11] M. E. Shenton, C. C. Dickey, M. Frumin, and R. W. McCarley, "A review of MRI findings in schizophrenia," *Schizophrenia Research*, vol. 49, no. 1–2, pp. 1–52, 2001.

- [12] K. J. Friston and C. D. Frith, "Schizophrenia: a disconnection syndrome?" *Clinical Neuroscience*, vol. 3, no. 2, pp. 89–97, 1995.
- [13] G. D. Pearlson, "Superior temporal gyrus and planum temporale in schizophrenia: a selective review," *Progress in Neuro-Psychopharmacology and Biological Psychiatry*, vol. 21, no. 8, pp. 1203–1229, 1997.
- [14] K. L. Davis, D. G. Stewart, J. I. Friedman et al., "White matter changes in schizophrenia evidence for myelin-related dysfunction," *Archives of General Psychiatry*, vol. 60, no. 5, pp. 443–456, 2003.
- [15] M. Walterfang, S. J. Wood, D. Velakoulis, and C. Pantelis, "Neuropathological, neurogenetic and neuroimaging evidence for white matter pathology in schizophrenia," *Neuroscience and Biobehavioral Reviews*, vol. 30, no. 7, pp. 918–948, 2006.
- [16] N. C. Andreasen, "The role of the thalamus in schizophrenia," *Canadian Journal of Psychiatry*, vol. 42, no. 1, pp. 27–33, 1997.
- [17] W. Byne, E. A. Hazlett, M. S. Buchsbaum, and E. Kemether, "The thalamus and schizophrenia: current status of research," *Acta Neuropathologica*, vol. 117, no. 4, pp. 347–368, 2008.
- [18] M. Walterfang, A. G. Wood, D. C. Reutens et al., "Morphology of the corpus callosum at different stages of schizophrenia: cross-sectional study in first-episode and chronic illness," *British Journal of Psychiatry*, vol. 192, no. 6, pp. 429–434, 2008.
- [19] D. Schretlen, G. D. Pearlson, J. C. Anthony et al., "Elucidating the contributions of processing speed, executive ability, and frontal lobe volume to normal age-related differences in fluid intelligence," *Journal of the International Neuropsychological Society*, vol. 6, no. 1, pp. 52–61, 2000.
- [20] J. K. Wing, N. Sartorius, T. Brugha et al., *Schedules for Clinical Assessment in Neuropsychiatry (SCAN) version 2.1*, World Health Organization, Geneva, Switzerland, 1996.
- [21] J. I. Nurnberger, M. C. Blehar, C. A. Kaufmann et al., "Diagnostic interview for genetic studies: rationale, unique features, and training," *Archives of General Psychiatry*, vol. 51, no. 11, pp. 849–863, 1994.
- [22] L. Xu, K. M. Groth, G. Pearlson, D. J. Schretlen, and V. D. Calhoun, "Source-based morphometry: the use of independent component analysis to identify gray matter differences with application to schizophrenia," *Human Brain Mapping*, vol. 30, no. 3, pp. 711–724, 2009.
- [23] C. D. Good, I. S. Johnsrude, J. Ashburner, R. N. A. Henson, K. J. Friston, and R. S. J. Frackowiak, "A voxel-based morphometric study of ageing in 465 normal adult human brains," *NeuroImage*, vol. 14, no. 1, pp. 21–36, 2001.
- [24] J. Ashburner and K. J. Friston, "Unified segmentation," *NeuroImage*, vol. 26, no. 3, pp. 839–851, 2005.
- [25] Y. O. Li, T. Adali, and V. D. Calhoun, "Estimating the number of independent components for functional magnetic resonance imaging data," *Human Brain Mapping*, vol. 28, no. 11, pp. 1251–1266, 2007.
- [26] V. D. Calhoun, T. Adali, G. D. Pearlson, and J. J. Pekar, "A method for making group inferences from functional MRI data using independent component analysis," *Human Brain Mapping*, vol. 14, no. 3, pp. 140–151, 2001.
- [27] C. R. Genovese, N. A. Lazar, and T. Nichols, "Thresholding of statistical maps in functional neuroimaging using the false discovery rate," *NeuroImage*, vol. 15, no. 4, pp. 870–878, 2002.
- [28] J. Talairach and P. Tournoux, *Co-Planar Stereotaxic Atlas of the Human Brain: 3-Dimensional Proportional System—An Approach to Cerebral Imaging*, Thieme Medical Publishers, New York, NY, USA, 1988.
- [29] J. L. Lancaster, M. G. Woldorff, L. M. Parsons et al., "Automated Talairach Atlas labels for functional brain mapping," *Human Brain Mapping*, vol. 10, no. 3, pp. 120–131, 2000.
- [30] S. Mori, K. Oishi, H. Jiang et al., "Stereotaxic white matter atlas based on diffusion tensor imaging in an ICBM template," *NeuroImage*, vol. 40, no. 2, pp. 570–582, 2008.
- [31] N. G. Cascella, S. C. Fieldstone, V. A. Rao, G. D. Pearlson, A. Sawa, and D. J. Schretlen, "Gray-matter abnormalities in deficit schizophrenia," *Schizophrenia Research*, vol. 120, no. 1–3, pp. 63–70, 2010.
- [32] K. L. Narr, A. W. Toga, P. Szeszko et al., "Cortical thinning in cingulate and occipital cortices in first episode schizophrenia," *Biological Psychiatry*, vol. 58, no. 1, pp. 32–40, 2005.
- [33] T. Kawashima, M. Nakamura, S. Bouix et al., "Uncinate fasciculus abnormalities in recent onset schizophrenia and affective psychosis: a diffusion tensor imaging study," *Schizophrenia Research*, vol. 110, no. 1–3, pp. 119–126, 2009.
- [34] Y. Hirayasu, R. W. McCarley, D. F. Salisbury et al., "Planum temporale and Heschl gyrus volume reduction in schizophrenia: a magnetic resonance imaging study of first-episode patients," *Archives of General Psychiatry*, vol. 57, no. 7, pp. 692–699, 2000.
- [35] N. C. Andreasen, L. Flashman, M. Flaum et al., "Regional brain abnormalities in schizophrenia measured with magnetic resonance imaging," *JAMA*, vol. 272, no. 22, pp. 1763–1769, 1994.
- [36] H. Fujiwara, C. Namiki, K. Hirao et al., "Anterior and posterior cingulum abnormalities and their association with psychopathology in schizophrenia: a diffusion tensor imaging study," *Schizophrenia Research*, vol. 95, no. 1–3, pp. 215–222, 2007.
- [37] J. Fitzsimmons, M. Kubicki, K. Smith et al., "Diffusion tractography of the fornix in schizophrenia," *Schizophrenia Research*, vol. 107, no. 1, pp. 39–46, 2009.
- [38] S. Y. Zhou, M. Suzuki, H. Hagino et al., "Volumetric analysis of sulci/gyri-defined in vivo frontal lobe regions in schizophrenia: precentral gyrus, cingulate gyrus, and prefrontal region," *Psychiatry Research*, vol. 139, no. 2, pp. 127–139, 2005.
- [39] G. García-Martí, E. J. Aguilar, J. J. Lull et al., "Schizophrenia with auditory hallucinations: a voxel-based morphometry study," *Progress in Neuro-Psychopharmacology and Biological Psychiatry*, vol. 32, no. 1, pp. 72–80, 2008.
- [40] G. Rizzolatti and M. Matelli, "Two different streams form the dorsal visual system: anatomy and functions," *Experimental Brain Research*, vol. 153, no. 2, pp. 146–157, 2003.
- [41] G. Neckelmann, K. Specht, A. Lund et al., "MR morphometry analysis of grey matter volume reduction in schizophrenia: association with hallucinations," *International Journal of Neuroscience*, vol. 116, no. 1, pp. 9–23, 2006.
- [42] P. Tanskanen, K. Ridler, K. M. Graham et al., "Morphometric Brain abnormalities in schizophrenia in a population-based sample: relationship to duration of illness," *Schizophrenia Bulletin*, vol. 36, no. 4, pp. 766–777, 2010.
- [43] M. Nakamura, R. W. McCarley, M. Kubicki et al., "Fronto-temporal disconnectivity in schizotypal personality disorder: a diffusion tensor imaging study," *Biological Psychiatry*, vol. 58, no. 6, pp. 468–478, 2005.
- [44] I. Spoletini, A. Cherubini, M. Di Paola et al., "Reduced fronto-temporal connectivity is associated with frontal gray matter density reduction and neuropsychological deficit in schizophrenia," *Schizophrenia Research*, vol. 108, no. 1–3, pp. 57–68, 2009.

- [45] P. G. Nestor, M. Kubicki, M. Niznikiewicz, R. J. Gurrera, R. W. McCarley, and M. E. Shenton, "Neuropsychological disturbance in schizophrenia: a diffusion tensor imaging study," *Neuropsychology*, vol. 22, no. 2, pp. 246–254, 2008.
- [46] A. E. Cavanna and M. R. Trimble, "The precuneus: a review of its functional anatomy and behavioural correlates," *Brain*, vol. 129, part 3, pp. 564–583, 2006.

## Review Article

# Multimodal MRI Neuroimaging Biomarkers for Cognitive Normal Adults, Amnestic Mild Cognitive Impairment, and Alzheimer's Disease

Ai-Ling Lin,<sup>1</sup> Angela R. Laird,<sup>1</sup> Peter T. Fox,<sup>1</sup> and Jia-Hong Gao<sup>2</sup>

<sup>1</sup> *Research Imaging Institute, The University of Texas Health Science Center at San Antonio, 7703 Floyd Curl Drive, San Antonio, TX 78229, USA*

<sup>2</sup> *Departments of Radiology, Psychiatry, and Behavioral Neuroscience and Brain Research Imaging Center, The University of Chicago, 5841 South Maryland, MC 2026, Chicago, IL 60637, USA*

Correspondence should be addressed to Ai-Ling Lin, [lina3@uthscsa.edu](mailto:lina3@uthscsa.edu) and Jia-Hong Gao, [jgao@uchicago.edu](mailto:jgao@uchicago.edu)

Received 16 March 2011; Revised 11 May 2011; Accepted 8 June 2011

Academic Editor: Andrea Cherubini

Copyright © 2012 Ai-Ling Lin et al. This is an open access article distributed under the Creative Commons Attribution License, which permits unrestricted use, distribution, and reproduction in any medium, provided the original work is properly cited.

Multimodal magnetic resonance imaging (MRI) techniques have been developed to noninvasively measure structural, metabolic, hemodynamic and functional changes of the brain. These advantages have made MRI an important tool to investigate neurodegenerative disorders, including diagnosis, disease progression monitoring, and treatment efficacy evaluation. This paper discusses recent findings of the multimodal MRI in the context of surrogate biomarkers for identifying the risk for AD in normal cognitive (NC) adults, brain anatomical and functional alterations in amnestic mild cognitive impairment (aMCI), and Alzheimer's disease (AD) patients. Further developments of these techniques and the establishment of promising neuroimaging biomarkers will enhance our ability to diagnose aMCI and AD in their early stages and improve the assessment of therapeutic efficacy in these diseases in future clinical trials.

## 1. Introduction

Aging is the greatest risk factor for neurodegenerative disorders in general, but specifically for Alzheimer's disease (AD). With the increasing life expectancy in developed countries, the incidence of AD, and consequently its socioeconomic impact, is growing. AD currently affects about 4.5 million Americans, which costs the USA economy more than \$100 billion each year. The number of AD patients is projected to increase to 11–16 millions by 2050, with a cost exceeding \$380 billion per year [1, 2].

To identify AD and monitor disease progression, neuropsychological tests such as the Mini-Mental State Exam (MMSE) and the cognitive subscale of the Alzheimers disease assessment (ADAS Cog) [3] are currently the most commonly used strategies. However, these tests have several limitations, as follows. MMSE is criticized by its marginal or absent assessment of some cognitive abilities that are affected early in the course of Alzheimer's disease or other dementing

disorders (e.g., limited memory and verbal fluency items and no problem solving or judgment items), and its relative insensitivity to very mild cognitive decline, particularly in highly educated individuals. ADAS Cog is limited by its relatively poor test-retest reliability, which likely reflects the influence of other factors on the patients' performance (e.g., the patients' mood). Furthermore, these tests are not able to distinguish the risk for AD in preclinical groups (cognitively normal elderly adults) or predict the conversion to AD from preclinical and mild cognitive impairment (MCI) groups.

The National Institute of Aging (NIA) has recently announced the revised clinical diagnostic criteria for AD dementia for the first time in 27 years (<http://www.nih.gov/news/health/apr2011/nia-19.htm>). Instead of addressing the disease and describing only later stages when symptoms of dementia are already evident, the updated guidelines cover the full spectrum of the disease as it gradually changes over many years. They describe (i) the earliest preclinical stages of the disease, (ii) MCI, and

(iii) dementia due to Alzheimer's pathology. Importantly, the guidelines now address the use of imaging and biomarkers in blood and spinal fluid that may help determine whether changes in the brain and those in body fluids are due to AD.

In this paper, we will focus on the imaging biomarkers as addressed in the new criteria. Specifically, we will discuss the surrogate biomarkers developed by the multimodal magnetic resonance imaging (MRI) methods for identifying the risk for AD in normal cognitive (NC) adults; brain anatomical and functional alterations in amnesic MCI (aMCI) and AD patients.

## 2. Brief Overview of Multimodal MRI Neuroimaging Biomarkers

**2.1. Structural Biomarkers.** The high spatial resolution, sensitivity, and specificity of MRI (e.g., resolution: 0.8 mm isotropic; sensitivity: 80–94%; specificity: 60–100%) have made it a powerful tool to identify structural alterations and brain atrophy using volumetric measurements of the entire brain [4, 5]. With advanced computer software, the neocortex of the brain on the MRI scans can be automatically subdivided into 32 gyral-based region of interests (ROIs) per hemisphere, including gray matter (GM), white matter (WM), and hippocampus volumes [6–8].

GM loss can also be determined by measuring cortical gray matter thickness (GMT). GMT is determined by calculating the three-dimensional distance from the outer cortical surface to the inner cortical GM-WM boundary using cortical modeling from the high-resolution MRI structural images (Figure 1). WM integrity can be assessed with diffusion tensor imaging (DTI). In brain tissues, the microscopic motion of water molecules is hindered by boundaries of tissue structure. In highly structured tissue such as WM, this motion is highly anisotropic and DTI provides directional information about it. Loss in WM structure results in the loss in anisotropy, which can be easily detected by DTI [9, 10].

**2.2. Functional Biomarkers.** Functional-based MRI can detect alterations and monitor disease progression related to brain metabolism, hemodynamics, and connectivity. Functional connectivity MRI (fcMRI) has been developed as a technique to determine the resting state brain connectivity as measured by the basal blood oxygenation-level-dependent (BOLD) signal. In its simplest form, functionally connected networks can be identified using a seed-based correlational approach, in which the average resting state time series from a region of interest is correlated with all other voxels in the brain [2, 11–14]. In contrast to this correlational method, independent component analysis (ICA) is a more advanced multivariate analysis method that allows resting state fMRI data to be decomposed into sets of independent, intrinsic brain networks [15–17]. In either approach, each functional network's neuronal activity is associated with a hemodynamic response, which consists of an increase in cerebral blood flow (CBF) and oxyhemoglobin and a rel-

ative decrease in deoxyhemoglobin. The changes in the oxyhemoglobin-deoxyhemoglobin ratio result in changes in BOLD signal.

Neuronal activity is tightly coupled with CBF (as mentioned above); therefore, another approach to assess the disease progression of AD is to measure CBF (in the units of mL/100 g/min). MR-based CBF measurements have been developed to investigate hemodynamic alteration in AD, including arterial spin labeling (ASL) [18] and dynamic contrast techniques [19]. Compared with the traditional CBF measurements using single-photon emission computed tomography (SPECT) with Tc-99m radioactive tracers [20, 21], the absence of ionizing radiation or injection and the ability to obtain high quality anatomical images within the same scanning session make MRI-based CBF techniques attractive methods for the study of AD, especially when repeated scans are needed for monitoring disease progression or assessing treatment effect.

Changes in neuronal activity during the progression of AD may be associated with the changes in brain metabolism. Brain metabolism can be measured with MR spectroscopy (MRS). Using proton ( $^1\text{H}$ ) MRS, numerous metabolites related to brain functions can be determined, including N-acetyl aspartate (NAA), myoinositol (MI), creatine, choline, glutamate, glutamine and lactate. NAA is present only within neural cell body, axons and dendrites, it is thus considered to be a marker of neuronal viability and function [22]. MI, on the other hand, has considerably higher concentration in glial cells and thus is often taken as a glial marker [23].

## 3. Preclinical-Cognitively Normal Adults

Beyond age, family history is the most significant risk factor for AD, with maternal transmission being significantly more frequent than paternal transmission [24]. Biomarkers for AD-associated pathological changes, including metabolic deficits and amyloid beta ( $A\beta$ ) load, have been observed in cognitively normal individuals who have maternal history of late-onset AD (FHm) [25, 26].

Structural MRI has been used to assess brain volume changes for cognitively intact elderly individuals with FHm, a paternal history of AD (FHp) and no parental history of AD (FH-) [27–29]. Compared with FH individuals, cognitively healthy subjects with a family history of late-onset AD had significantly decreased gray matter volume (GMV) in the precuneus, middle frontal, and superior frontal gyri (Figure 2; [27]). FHm subjects had even significantly smaller inferior frontal, middle frontal, precuneus, and lingual gyri compared with FH and FHp individuals (Figures 2 and 3) [27, 28].

Another chief known genetic factor for AD is  $\epsilon 4$  allele apolipoprotein E gene (APOE  $\epsilon 4$ ). Increasing age and carrying APOE  $\epsilon 4$  are well-established risk factors for AD. Healthy older APOE  $\epsilon 4$  carriers, particularly  $\epsilon 4$  homozygotes, have demonstrated brain structure changes related to noncarriers. In a recent study with a longitudinal cohort of 1186 healthy elderly persons (65–89 years), Crivello et al. found that an annual rate of gray matter volume loss

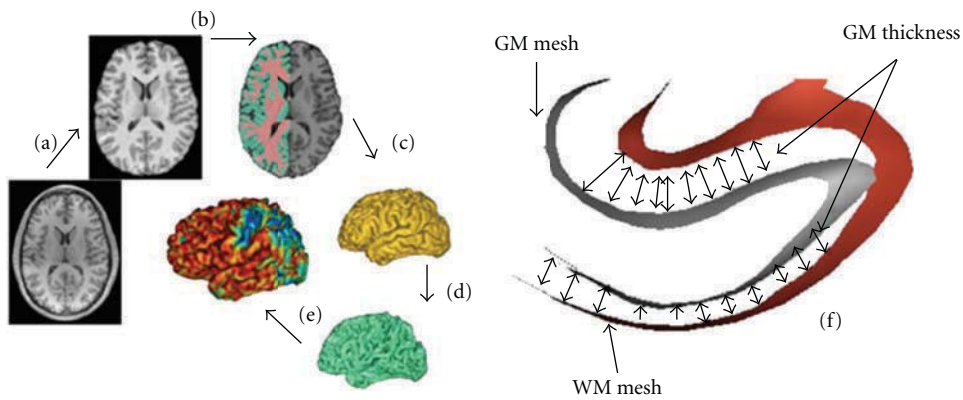


FIGURE 1: T<sub>1</sub>-weighted image processing pipeline consists of (a) skull stripping; (b) spatial normalization, RF homogeneity correction, and tissue segmentation; (c, d) extraction of GM and WM pial surfaces; (e, f) calculation of GMT.

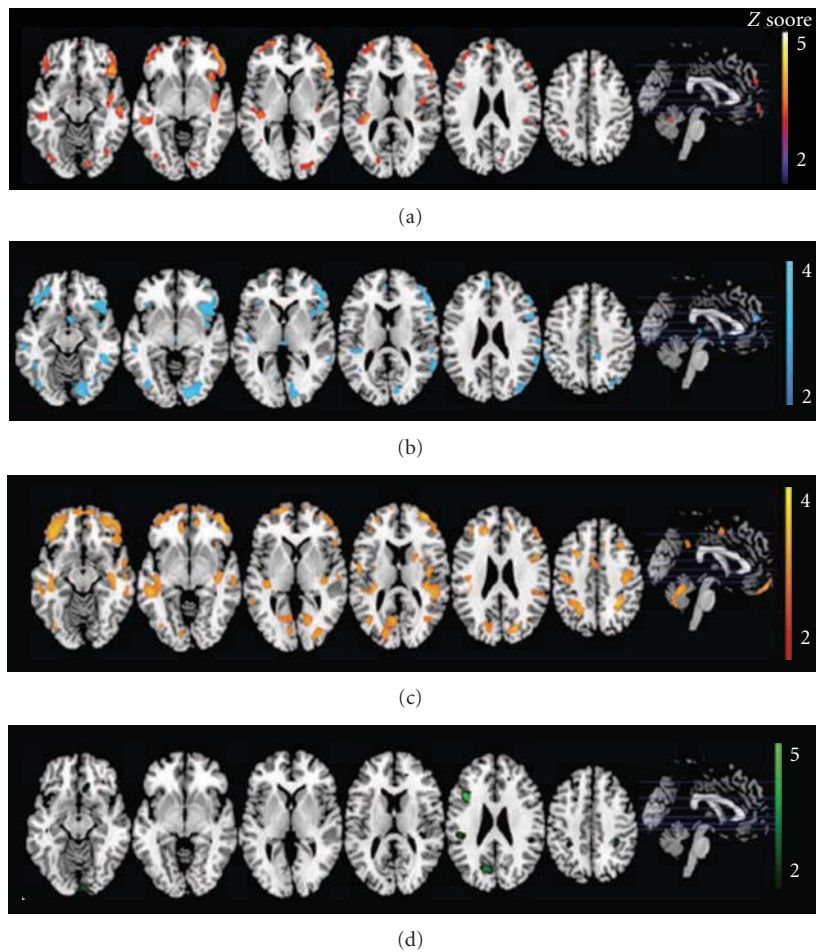


FIGURE 2: The first 2 rows display maps from subjects with a maternal family history of Alzheimer’s disease (FHm) as compared with subjects with no family history (FH-) (a) and subjects with a paternal family history (FHp) (b). Row (c) shows gray matter volume (GMV) reductions in APOE  $\epsilon$ 4-negative FHm subjects compared with APOE  $\epsilon$ 4-negative FH subjects. Statistical parametric maps showing GMV reductions in normal FHp subjects as compared with FH subjects are in row (d). Areas of GMV decrease are represented on purple-to-yellow, blue-to-light blue, dark orange-to-yellow, and green-to-light green color-coded scales for the 4 contrasts, reflecting Z scores between 2 and 5 for the upper contrast and between 2 and 4 for the lower 3 contrasts. Areas of gray matter volume decrease are displayed on a standardized spatially normalized MRI (adapted with permission from [27]).

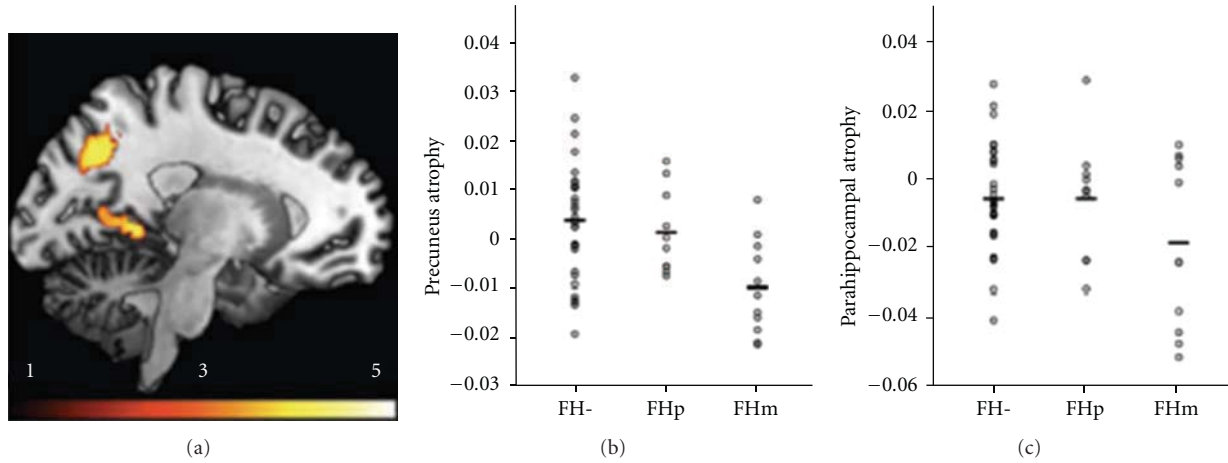


FIGURE 3: Increased regional atrophy in maternal history of Alzheimer’s disease (FHm) group compared to subjects without family history of late-onset Alzheimer’s disease (FH-) and paternal history of Alzheimer’s disease (FHp) groups (adapted with permission from [28]).

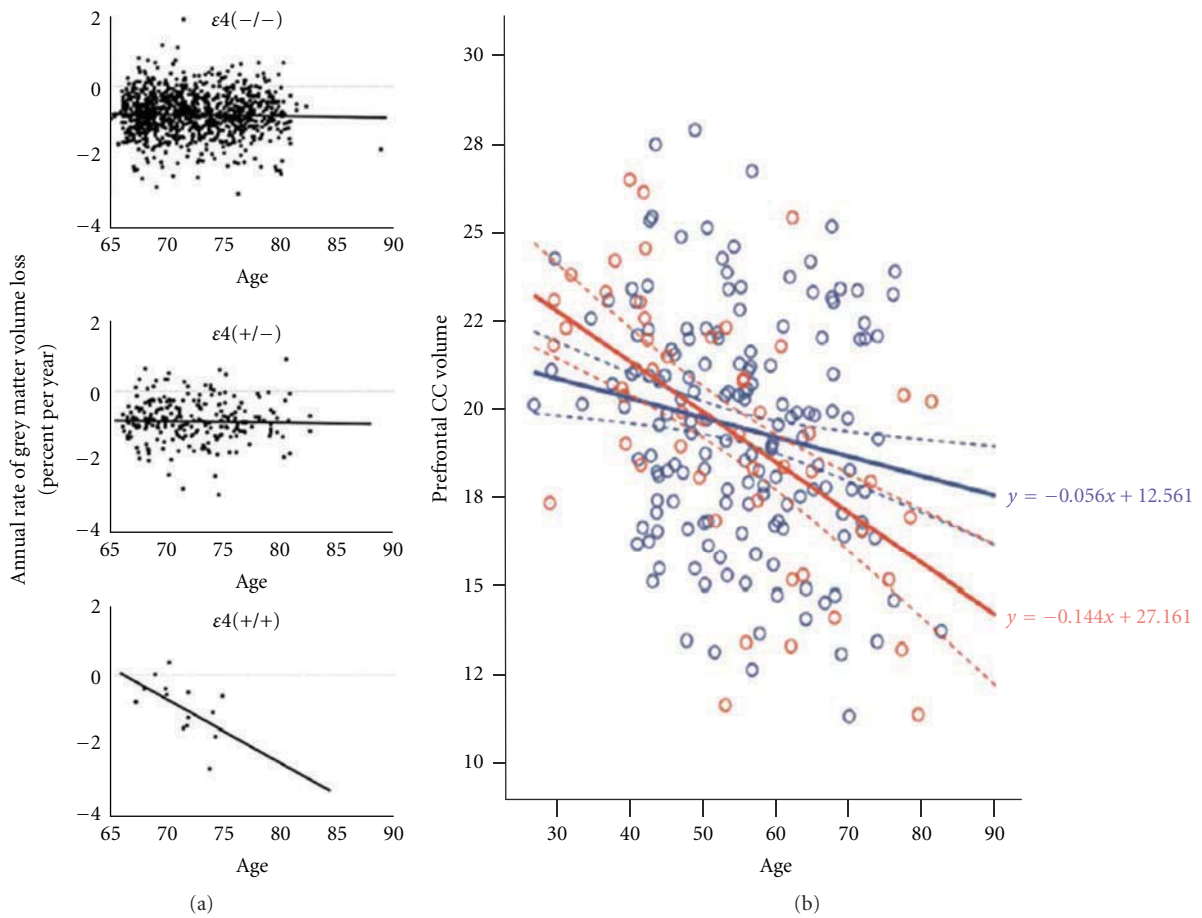


FIGURE 4: (a) Age effect on the longitudinal followup of GMV for the three APOE  $\epsilon 4$  groups, illustrating the significant interaction between age and the APOE  $\epsilon 4$ .  $\epsilon 4(-/-)$ : noncarriers for the APOE  $\epsilon 4$  allele, and  $\epsilon 4(+/-)$ : heterozygous for the APOE  $\epsilon 4$  allele,  $\epsilon 4(+/+)$ : homozygous for the APOE  $\epsilon 4$  allele (adapted with permission from [30]). (b) Regression of the normalized volume of the prefrontal callosal subregion on age in APOE  $\epsilon 4$  carriers (red) and noncarriers (blue). Thick lines show linear regression lines and dotted lines 95% mean confidence intervals of the slope. Formulas denote regression lines. Normalization was done to total intracranial volume (adapted with permission from [31]).

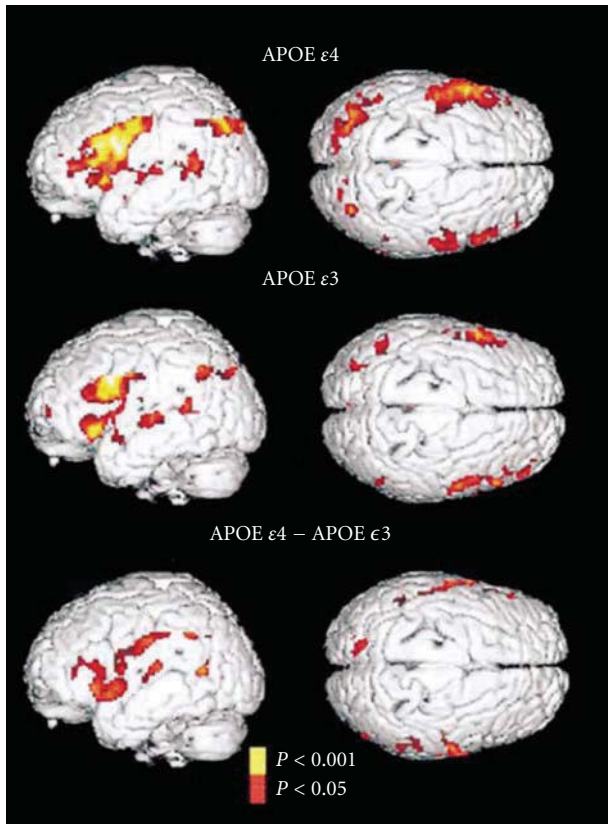


FIGURE 5: Statistical parametric maps of the brain used to assess subjects' performance on memory-activation tests in carriers of the APOE  $\epsilon 4$  allele and carriers of the APOE  $\epsilon 3$  allele. The signal intensity increased significantly in the left inferior frontal region, the right prefrontal cortex, the transverse temporal gyri bilaterally, and the left posterior temporal and inferior parietal regions in both groups. However, both the extent and the intensity of activation were greater among the carriers of the APOE  $\epsilon 4$  allele. The carriers of the APOE  $\epsilon 4$  allele also had significant increases in the left parahippocampal, the left dorsal prefrontal cortex, and in the inferior and superior parietal lobes and the anterior cingulate gyrus. Direct comparisons of the carriers of the APOE  $\epsilon 4$  allele and the carriers of the APOE  $\epsilon 3$  allele (bottom panel, which shows the difference between the carriers) further demonstrated the greater extent and magnitude of activity in the left prefrontal region and bilateral orbitofrontal, superior temporal, and inferior and superior parietal regions in the carriers of the APOE  $\epsilon 4$  allele (adapted with permission from [32]).

was seen in  $\epsilon 4$  homozygotes, whereas no age effect was seen in  $\epsilon 4$  heterozygotes and in noncarriers (Figure 4(a)) [30]. Similarly,  $\epsilon 4$  homozygotes had a significant larger rate of hippocampal volume loss than heterozygotes or noncarriers. In another anatomical study, Filippini et al. observed white matter atrophy, including corpus callosum (CC) volume and all subregions, in both APOE  $\epsilon 4$  carriers and noncarriers. However, the slope has been steeper in the APOE  $\epsilon 4$  carriers compared with the noncarriers particularly in the prefrontal region ( $P = 0.02$ ) (Figure 4(b)) [31].

In addition to structural changes, APOE  $\epsilon 4$  has also shown great impact on brain function. Memory is the first

cognitive domain to be affected by AD [42], and impairments have been found in APOE  $\epsilon 4$  carriers relative to noncarriers [43, 44]. Using functional MRI (fMRI), Bookheimer et al. observed that during a memory task in a group of healthy subjects (aged 47–82), APOE  $\epsilon 4$  carriers demonstrated significant increases in the left parahippocampal region, the left dorsal prefrontal cortex, the inferior-superior parietal lobes, and the anterior cingulate gyrus (Figure 5; [32]). In addition, the extent and the intensity of activation for the APOE  $\epsilon 4$  carriers were greater in the left inferior frontal region, the right prefrontal cortex, the transverse temporal gyri bilaterally, the left posterior temporal, and inferior parietal regions relative to the noncarriers (carriers of the APOE  $\epsilon 3$  allele). Direct comparisons of APOE  $\epsilon 4$  carriers and noncarriers further demonstrated the greater extent and magnitude of activity in the left prefrontal, bilateral orbitofrontal, and superior temporal regions. In carriers of the APOE  $\epsilon 4$  allele, it has been demonstrated in inferior and superior parietal regions.

In a younger group (mean age = 21–30), APOE  $\epsilon 4$  carriers demonstrated increased task-induced brain activation in hippocampus relative to the noncarriers [45, 46]. Overactivity of brain function has also been found in young APOE  $\epsilon 4$  carriers but disproportionately reduced with advancing age even before the onset of measurable memory impairment (Figure 6; [33]). In both age groups, a significant interaction has been found between age and APOE  $\epsilon 4$  status in the hippocampi, frontal pole, subcortical nuclei, middle temporal gyri, and cerebellum. These results have suggested that APOE genotype determines age-related changes in brain function, and greater activation reflects greater cognitive “effort” by APOE  $\epsilon 4$  carriers to obtain the same level of performance as the noncarriers, and/or reflect neuronal mechanism to compensate for processes, such as reduced synaptic plasticity, neuronal growth, or altered long-term potentiation in the carriers.

APOE  $\epsilon 4$  carriers have also shown disrupted resting state brain activity in the absence of  $A\beta$  or decreased CSF in cognitively normal elderly (mean age = 62) using functional connectivity MRI method [11–13, 47]. Similarly, young APOE  $\epsilon 4$  carriers (mean age = 21–30), although had no difference in cognition and GM volume compared to their age-mated controls, showed increase in default mode network (involving medial temporal, medial prefrontal, and retrosplenial cortical areas) coactivation [46], suggesting that the function of these areas subject to the disease process in AD is modulated by APOE  $\epsilon 4$  allele at very early stage.

Taken together, these results provide evidence that influence of the genetic effect (familial and APOE  $\epsilon 4$  allele) on neurophysiological characteristics and the risk for AD can be detected using MRI decades prior to any clinical or neuropathological expression of neurodegenerative process.

#### 4. Mild Cognitive Impairment

MCI is a transitional state between normal aging and dementia. MCI is a diagnosis given to individuals who experience memory problems greater than normally expected

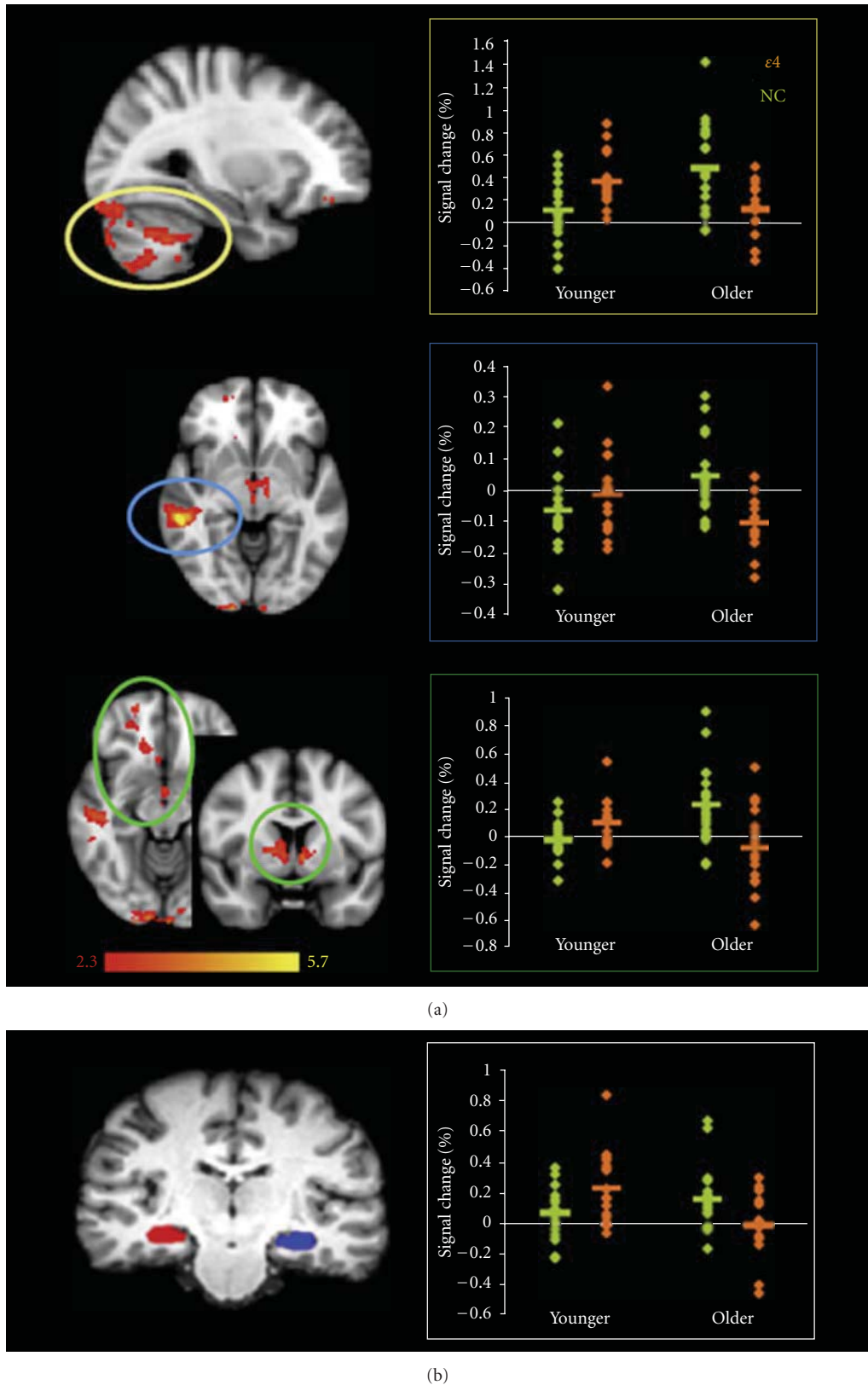


FIGURE 6: AGE by GENE interactions in the “novel versus familiar” contrast of the encoding task. (a) Regions showing significant interaction between AGE and GENE factors ( $P < 0.05$ , corrected for multiple comparisons) with plots of percentage signal change in brain regions showing group-related differences where  $\epsilon 4$  (orange) defines  $\epsilon 4$ -carriers and NC (green) defines noncarriers. (b) ROIs for the left and right hippocampi overlaid on a structural image (left) with associated plot of average hippocampal percentage signal change showing significant age-by-gene interaction (left hippocampus:  $P = 0.002$ , right hippocampus:  $P = 0.003$ ) (adapted with permission from [33]).

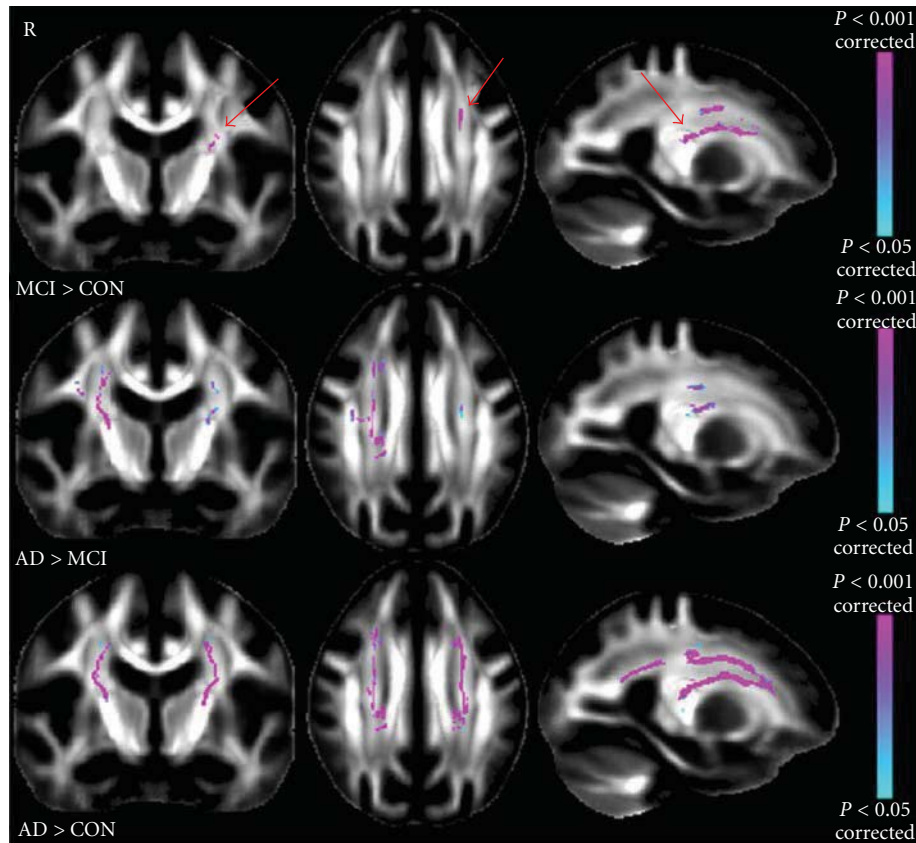


FIGURE 7: *Top.* Significant mode of atrophy (MO) results showing the contrast MCI > CON (controls; arrows). *Middle.* Significant MO results showing the contrast AD > MCI. *Bottom.* Significant MO results showing the contrast AD > CON. (adapted with permission from [34]).

with typical aging, but who do not show other symptoms of dementia, such as impaired judgment or reasoning. MCI has various clinical subtypes, including amnesic single domain (aMCI-S), amnesic multiple domain (aMCI-M), nonamnesic single domain (naMCI-S), and nonamnesic multiple domain (naMCI-M) [48]. Nonamnesic forms of MCI (naMCI, i.e., naMCI-S and naMCI-M) have had findings suggestive of vascular disease, whereas amnesic forms of MCI (aMCI, i.e., aMCI-S and aMCI-M) have appeared to have demographic, genetic, and MRI findings suggestive of AD pathology [48, 49]. Although aMCI can be defined using neuropsychiatric criteria, brain imaging studies have aimed to develop measures that are sensitive enough to distinguish aMCI from normal aging with high specificity [50]. Many other studies attempt to differentiate between aMCI subjects who will convert to AD, over a specific followup interval versus those who remain stable or ever recover [51]. In this section, we elaborate the current findings in these two areas.

**4.1. Distinguishing aMCI from Normal Aging.** Although age-related regional volume loss is apparent and widespread in nondemented individuals [5, 52], aMCI is associated with a unique pattern of structural vulnerability reflected in differential volume loss in specific regions. In a cross-sectional

study, aMCI patients were observed with a significant WM abnormality in the region of crossing fibers in the centrum semiovale in comparison to NC (Figure 7) [34]. In a ten-consecutive-year longitudinal study, 18 participants (among 138) who converted from normal to MCI showed accelerated changes (compared to normal controls) on whole brain volume, ventricular CSF (vCSF), temporal gray matter, and orbitofrontal and temporal association cortices, including the hippocampus ( $P \leq 0.04$ ) (Figure 8) [35].

Similar findings of vCSF increases in aMCI patients compared to normal controls have been reported by Vemuri et al. [53]. In this study, Vemuri and colleagues further demonstrated that changes in serial structural MRI differed by APOE  $\epsilon 4$  status overall among aMCI, with higher brain atrophy rates in APOE  $\epsilon 4$  carriers. In addition, MR-based structural biomarkers, compared with other biomarkers (e.g., CSF), showed higher correlation with concurrent change on general cognitive and functional indices in impaired subjects.

Functional abnormality has also been shown in aMCI patients. Compared with healthy controls, aMCI patients had a regional pattern of brain disconnection between the posterior cingulate cortex (PCC) and the medial prefrontal cortex and the rest of the brain. These disconnections

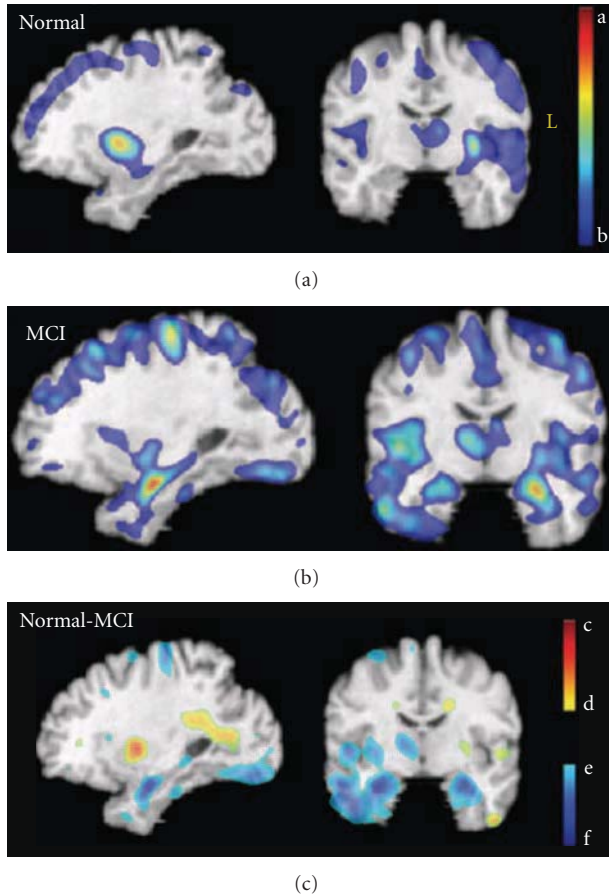


FIGURE 8: Patterns of GMV loss in MCI and normal aging. Average slopes of RAVENS maps for normal (a) and MCI (b) groups. The red-yellow color indicates greater volume loss. Bottom row: difference between the two groups; blue/green are regions in which MCI subjects showed higher rate of gray matter decrease. (c) Red/yellow colors reflect an increase of periventricular small vessel disease, which appears gray in T1-weighted images and is segmented as gray matter. The color bars display estimated regression coefficients and are defined by the following numbers, all in  $\text{mm}^3/\text{year}$  (per voxel in the template space): a =  $-0.020$ , b =  $-0.0053$ , c =  $0.026$ , d =  $0.0053$ , e =  $-0.0053$ , and f =  $-0.023$  (adapted with permission from [35]).

could be observed even in the absence of GM atrophy (Figure 9) [36].

**4.2. Conversion from aMCI to AD.** Cognitively normal elderly subjects convert to AD at a rate of only 1-2% per year, whereas aMCI subjects convert to AD at a rate of 12–15% per year [54]. Studying the similarities and differences between aMCI and AD would provide valuable information of the disease mechanism and progression. Multimodal MRI offers noninvasive methods for detection and possibly prediction of the conversion from aMCI to AD [6–8]. In a 3-year followup of 118 aMCI individuals who progressed to a diagnosis of AD, Desikan et al. reported that atrophy in the medial temporal cortex (as measured by hippocampal volume, entorhinal cortex thickness, amygdala volume, temporal

pole thickness, and parahippocampal gyrus thickness) can accurately and reliably predict time to disease progression [6, 7]. They demonstrated that aMCI individuals with significant atrophy of the medial temporal factor regions are three times as likely to progress to AD, compared with aMCI individuals with preserved medial temporal factor regions. Their results also demonstrated that amygdala and temporal pole may be additional important structures for predicting the conversion from aMCI to AD. Similar observations were found in a meta-analysis involving 40 studies of imaging data from 1351 patients, suggesting that atrophy in the (trans) entorhinal area and hippocampus most reliably predict the progression from aMCI to AD [55]. These data provide strong evidence that AD-related volume losses are most readily detected in the medial temporal lobe in aMCI. The reduction in medial temporal lobe volume is therefore an important indicator in predicting the transition of aMCI to AD.

MR-based ASL techniques provide a functional biomarker (perfusion) to predict the progression from MRI to AD. In a longitudinal study ( $2.7 \pm 1.0$  years), Chao et al. reported that the MCI individuals who converted to dementia displayed hypoperfusion in the right precuneus, right inferior parietal cortex, and right middle frontal cortex [56]. A similar finding was reported in the Schroeter et al. meta-analytic study (involving 1351 patients) in which hypoperfusion in the inferior parietal lobules was found to most reliably predict the progression from aMCI to AD [55]. Furthermore, baseline perfusion from the right precuneus predicted subsequent declines in clinical dementia rating sum of boxes, functional activities questionnaire and selective attention (Stroop Switching), and baseline perfusion from the right middle frontal cortex predicted subsequent episodic memory decline. These results suggest that hypoperfusion as detected by ASL MRI can predict progression from MCI to AD.

## 5. Alzheimer's Disease

AD is histopathologically characterized by the formation of  $\beta$ -amyloid ( $A\beta$ ) plaques and neurofibrillary tangles (NFT). Progressions of the  $A\beta$  plaques and NFT pathology of AD correlate closely with loss of neurons and synapses [57]. These losses further result in gross atrophy, including cortical gray matter loss, reduced subcortical gray, and white matter volumes, as well as expanding ventricular and sulcal cerebrospinal fluid (CSF) spaces [37, 38] (Figure 10; similar regions of  $A\beta$ /NFT deposition and brain atrophy in AD). In AD, this brain atrophy is localized to the medial temporal limbic cortex during its earliest states. At later stages of disease, it progresses to paralimbic cortical regions and the neocortex [57]. The temporal limbic cortex has essential roles in episodic memory. Since memory impairment is the earliest symptom of AD, the temporal limbic cortex (including entorhinal cortex and hippocampus) has been an attractive target for structural neuroimaging studies [58–62].

Using brain volumetric measurements, patients with mild AD showed significantly smaller brain regions of

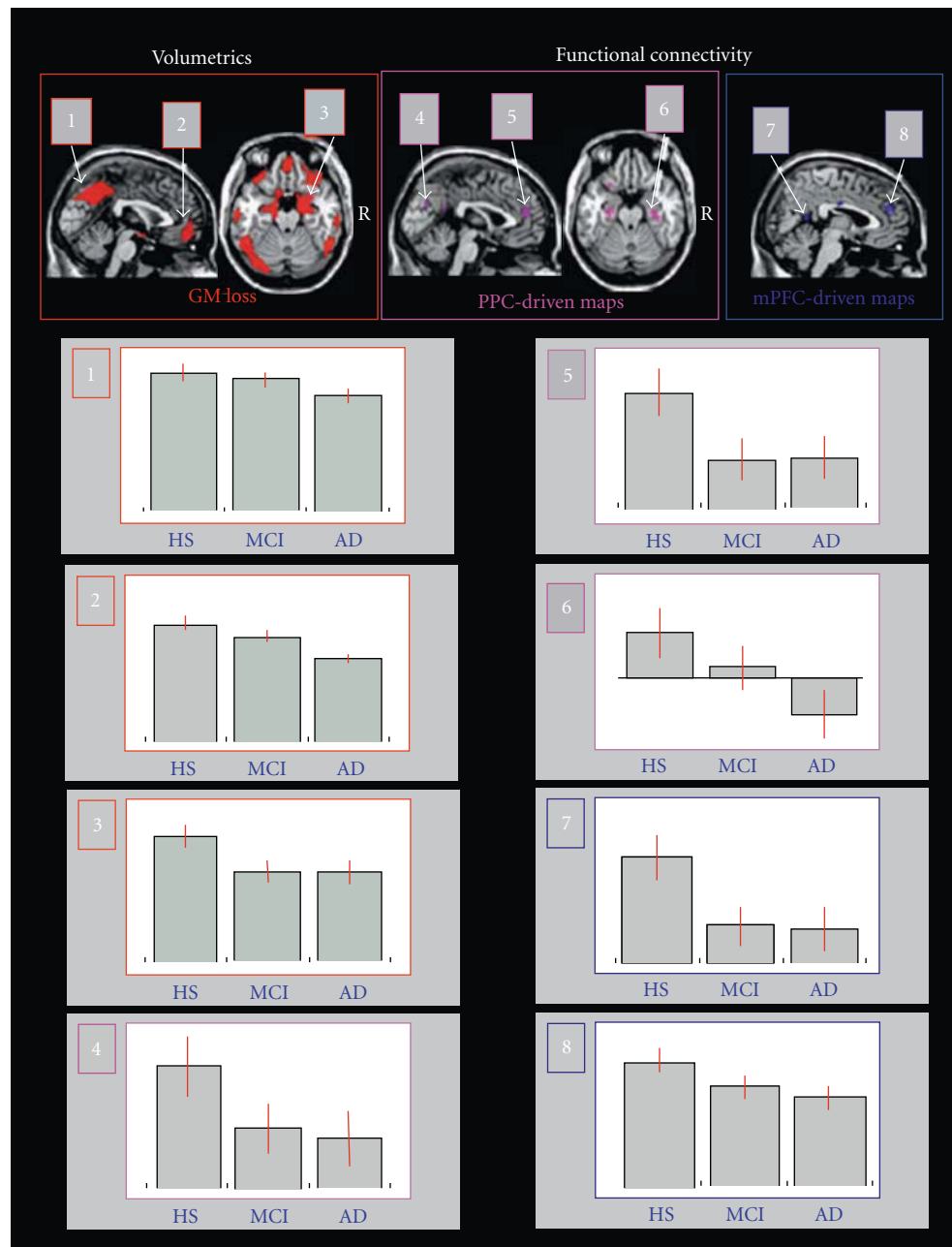


FIGURE 9: Distribution of reduced regional GMV (top panel on the left) and functional connectivity (top panel on the right) observed in patients with fully developed dementia (AD) compared with healthy subjects (HS). Changes of functional connectivity were assessed using both posterior cingulate (PCC) and medial prefrontal cortex (mPFC) driven connectivity maps (adapted with permission from [36]).

hippocampus (25%) and entorhinal cortex (37%) than healthy elderly controls [58–62]. In a number of longitudinal studies, significantly higher rates of brain atrophy were observed in AD [63–66]. The global atrophy rate in normal aging typically increases from 0.3% to 0.5% per year at age 70–80 but increases from 2% to 3% per year in AD [67–69]. Similar regional observations have also been found in hippocampus (controls, 1.0% to 1.7% per year; AD, 3.0% to 5.9% per year) and in entorhinal cortex (controls, 1.4% to 2.9% per year; AD, 7.15 to 8.4% per year) [2, 70, 71].

MR-based volume measures, particularly for the hippocampus, have been shown to be a strong structural biomarker for AD, as follows [72–74]. First, it has been demonstrated that a significant correlation exists between MRI and histological-based hippocampal volumes ( $r = 0.97$ ,  $P < 0.001$ ); the difference in the hippocampal volumes between normal and AD groups was 42% for the MRI data, and 40% for the histology data after adjusting for tissue shrinkage during specimen processing. Moreover, both the histological and MRI hippocampal volume measurements

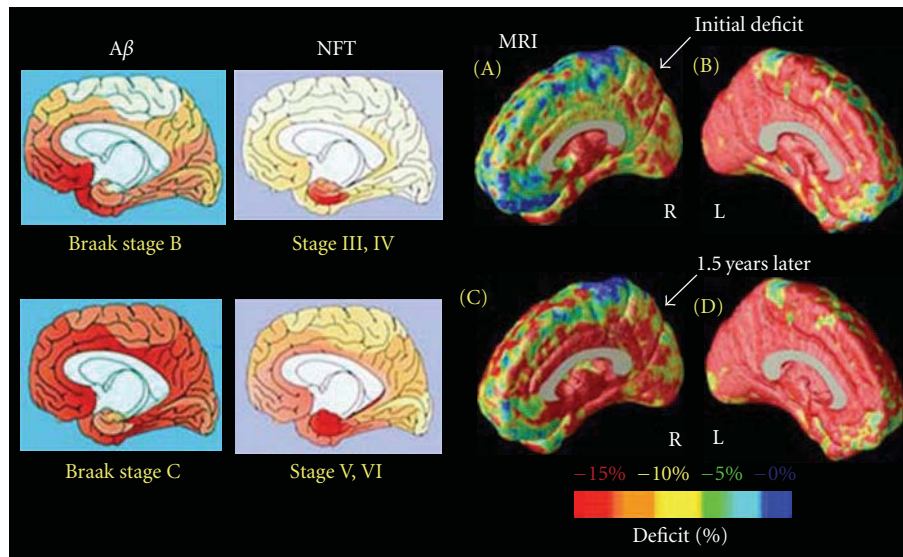


FIGURE 10: Gray matter deficits spread through the limbic system in moderate AD. Average maps of gray matter density in patients and controls were subtracted at their first scan (A and B) and at their followup scan 1.5 years later (C and D). Colors show the average percentage loss of gray matter relative to the control average. Profound loss engulfs the left medial wall (>15%; B and D). On the right, however, the deficits in temporoparietal and entorhinal territory (A) spread forward into the cingulate gyrus 1.5 years later (C). Limbic and frontal zones clearly show different degrees of impairment (C). MRI-based changes, in living patients, agree strongly with the spatial progression of  $\beta$ -amyloid ( $A\beta$ ) and NFT pathology observed after mortem (Braak Stages B, C, and III to VI), (adapted with permission from [37, 38]).

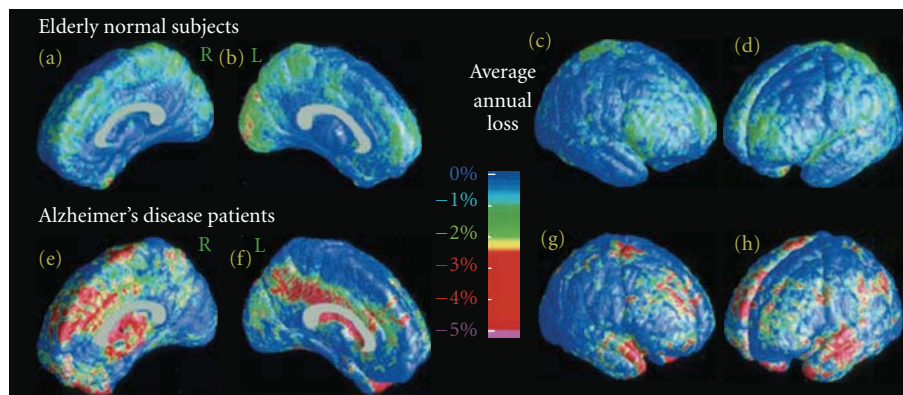


FIGURE 11: Average gray matter loss rates in healthy aging and AD. The maps show the average local rates of loss for gray matter, in groups of controls (top, (a)–(d)) and patients with AD (bottom, (e)–(h)). Loss rates are <1% per year in controls. They are significantly higher in AD and strongest in frontal and temporal regions (g, h) at this stage of AD. (adapted with permission from [39]).

were significantly associated with the number of hippocampal neurons ( $r = 0.91$ ,  $P < 0.001$  and  $r = 0.90$ ,  $P < 0.01$ ). Second, when compared with a temporal lobe neocortical reference volume, the hippocampal volume showed an anatomically unique correlation to memory performance such as delayed verbal recall [72–74].

With GMT measurements, mild-to-moderate AD subjects have cortices that are an average of 18% thinner relative to healthy controls (AD =  $3.1 \pm 0.28$  mm, controls =  $3.74 \pm 0.32$  mm) [75]. Significant GMT declines in AD were found in temporal, orbitofrontal, and parietal regions. The most pronounced changes occur in the allocortical region of the medial temporal lobes, which outlines the parahippocampal gyrus representing a loss of >1.25 millimeters of cortical

thickness [75, 76]. In a followup study 1.5 years later, patients with AD lost significant GM ( $P < 0.05$  for overall annual loss of gray matter) (Figures 11(e)–11(h); [39]) at a significantly higher rate than controls ( $P < 0.042$ ), with a total gray matter loss rate of  $5.03 \pm 2.28\%$  per year (left hemisphere  $5.43 \pm 3.29\%$  per year; right hemisphere  $4.64 \pm 3.31\%$  per year, whereas few regions in healthy controls exceeded a 1% annual gray matter loss). Regions with a prominent 4–5% annual loss included the right cingulate, temporal, and frontal cortices bilaterally (Figure 11, bottom row).

GMT changes are strong structural biomarkers for AD. Highly significant linkage was found relating greater GMT deficits to lower cognitive scores on the MMSE (Figure 12; [39]). These correlations were observed in all

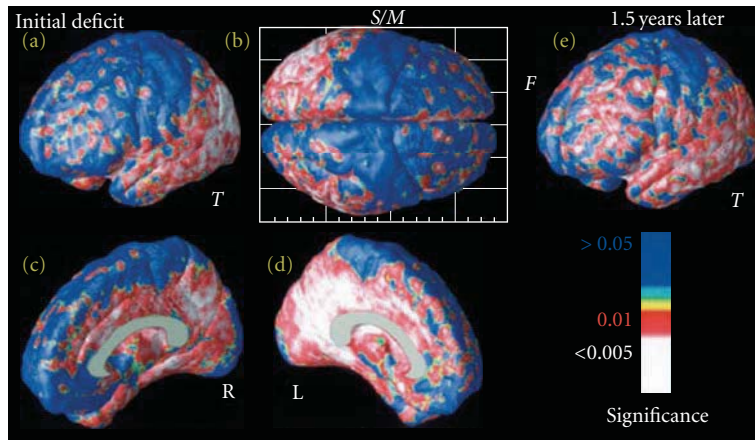


FIGURE 12: Mapping links between cognitive performance and changing brain structure. These maps show the significance of the linkage between gray matter reductions and cognition, as measured by MMSE score. Variations in temporal, parietal, and ultimately frontal (e) tissue are linked with cognitive status. Less gray matter is strongly correlated with worse cognitive performance, in all regions with prominent deficits. Linkages are detected most strongly in the left hemisphere medial temporoparietal zones (d). As expected, no linkages are found with sensorimotor gray matter variation (b), which was not in significant deficit in late AD (adapted with permission from [39]).

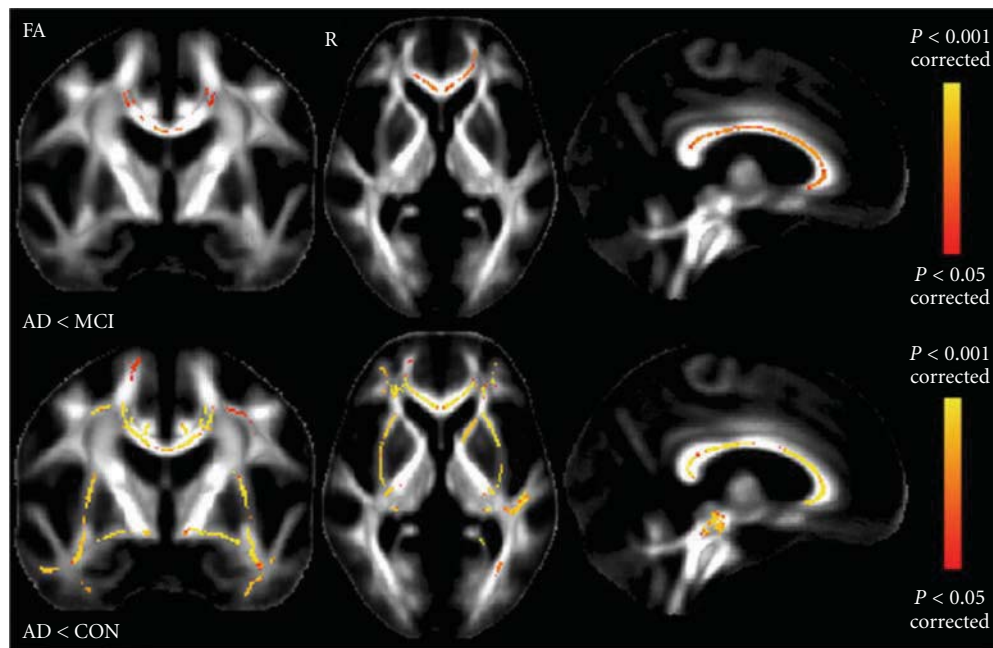


FIGURE 13: First row: significant FA results showing the contrast MCI > AD; second row: significant FA results showing CON (controls) > AD (adapted with permission from [34]).

brain regions, including the temporal, parietal, and limbic cortices. Correlations were also found between frontal gray matter reduction and lower MMSE scores, but only at the later time point, when frontal gray matter was in significant deficit (Figure 12(e)). No correlations were found between gray matter differences in sensory and motor cortices and cognitive performance (Figure 12(b), blue, S/M). These results support the theory that the relationship between brain structure and cognition is regionally specific in AD,

at least initially (Figure 12(b)). Correlations were observed to be strongest in regions with greatest average loss, such as the left cingulate and left temporal and parietal cortices (Figure 12(d)).

WM degeneration has also been considered an important indicator of AD. In a comparison of healthy young versus older adults, WM has been found to decline in volume with increasing age but is further reduced in AD, with parahippocampal, entorhinal, inferior parietal, and rostral

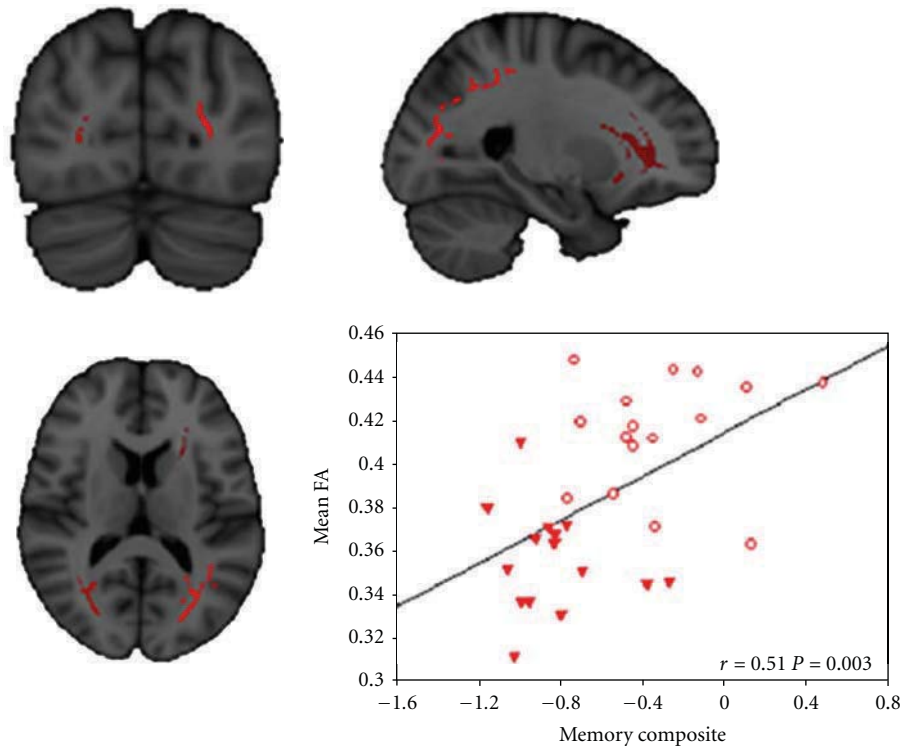


FIGURE 14: Significant correlations between regional alterations of FA in patients and the composite memory scores (adapted with permission from [40]).

middle frontal areas showing the strongest AD-associated reductions in WM [77]. AD patients, similar to aMCI patients (but more severe), have shown significant increase in diffusion atrophy in the region of crossing fibers in the centrum semiovale (Figure 6; [34]). They have further shown regionally specific shape abnormalities and reduction in fractional anisotropy (FA) in the corpus callosum, anterior commissure, uncinate fasciculus, cingulum tract, and sagittal stratum tract (these have not observed in aMCI patients in comparison to NC; Figure 13; [34, 78, 79]). These results suggest that disruption in the white matter tracts near the temporal lobe may represent the secondary consequence of the medial temporal lobe pathology in AD. This is consistent with the observation that FA values are significantly related to memory performance among AD patients (Figure 14; [40]).

Structural imaging is able to detect AD only at a stage in which the disease has progressed so far that neurons are already irreversibly lost. Ideally, AD should be diagnosed at an earlier stage in which neurons are impaired by the disease process, but not yet fully damaged, and thus can be potentially salvaged [2, 13]. In contrast, alterations of neuronal activity, metabolism, and hemodynamics are accompanied by the impairment of neurons and usually precede neuronal death prior to any cognitive deficits. Functional MRI has shown great promise in the detection of AD at this very early stage of disease, as well as during disease progression.

Disrupted functional connectivity has been observed in patients with AD in the default mode network, which is

associated with autobiographical memory retrieval [80, 81]. Similar to aMCI, functional connectivity abnormalities were observed in the PCC and a set of default mode regions, including the medial prefrontal cortex, hippocampus, inferior temporal cortex, bilateral visual cortices, and the precuneus in AD patients [82]. This disruption of connectivity was observed to intensify during aMCI and AD disease progression (Figure 15; [41]). With concurrent fMRI and structural MRI measurements, the PCC showed reduced connectivity in patients progressing into AD even in the absence of GM atrophy (Figure 9; [36]). This indicates that functional connectivity abnormalities precede GM atrophy in the PCC and supports the hypothesis that GM atrophy in specific regions of AD brains likely reflects a long-term effect of brain disconnection.

In AD patients, significant declines of CBF have been found in frontal, parietal, and temporal regions ( $P < 0.001$ ), with more marked reductions in those patients with severe dementia. Covariance analysis revealed that aging and disease severity have a pronounced effect on CBF, especially that of the left parietal region. Significant decreases of CBF have been detected with ASL-MRI in temporal, parietal, and frontal cortex and the posterior cingulate in patients with AD, compared to the healthy elderly controls. The observations have been consistent with those observed using SPECT. Using dynamic contrast method, CBF has been found significantly reduced in insular cortex [83, 84]. Because the insula is an important brain structure for the

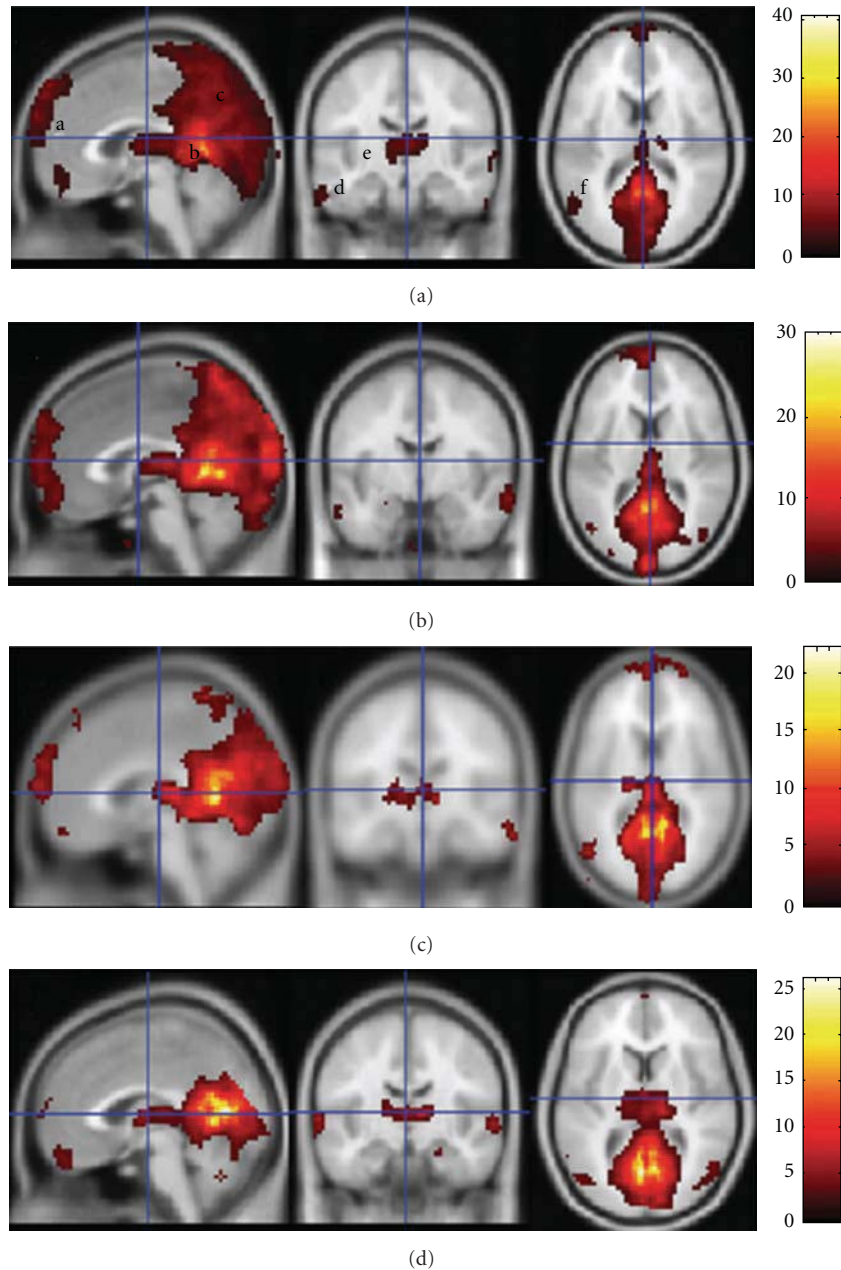


FIGURE 15: (a–d) Left to right: sagittal, coronal, and axial views of T1-weighted MNI canonical brain templates show intragroup maps of the default mode network (DMN) based on the seed of the PCC in, (a), control group, (b), mild AD group, (c), moderate AD group, and (d), severe AD group. The regions involved in the DMN are labeled as follows in (a): a = ventral MPFC, b = PCC, c = precuneus and/or cuneus, d = ITC, e = thalamus, and f = inferior parietal cortex. Color scale =  $t$  values (adapted with permission from [41]).

autonomic control of blood pressure and heart rate, the observations suggested that AD pathology has effect on ventral autonomic cardiorespiratory dysfunction.

In AD patients, significant N-acetyl aspartate (NAA) reductions have been found in various brain areas, including PCC, hippocampus, and GM of the temporal, parietal, and sometimes the frontal as well as occipital cortices [23, 85]. Decrease in NAA reflects a combination of losses of neuronal cells/dendritic structures, reduced myelination, and

decreased neuronal metabolism. As a result, the degree of cognitive impairment has been well correlated with the degree of NAA decrease; poor performance on memory tests correlated with lower gray matter NAA level [86]. In contrast to NAA, myo-inositol (MI), a glial biomarker, has been found to be dramatically increased in AD. Elevated MI is most likely due to the increase of gliosis in AD. Taken together, NAA and MI are important and useful metabolic biomarkers to distinguish AD from normal aging.

## 6. Future Directions

Mitochondrial dysfunction is a well-known biomarker of AD. Mitochondria are the predominate source (>98%) of energy production in mammals, yielding ATP through oxidative phosphorylation of glucose. In the brain, oxidative metabolism ( $O_2$  consumption) is the predominant source of energy (ATP generation), supporting baseline demands and maintaining viability, as well as responding rapidly and in a highly regional manner to changes in neuronal activity induced by task performance. Failure to maintain adequate levels of tissue oxygenation rapidly results in tissue death as observed of brain atrophy in AD patients.

To identify the integrity of the mitochondrial function, cerebral metabolic rate of glucose ( $CMR_{Glc}$ ) and oxygen ( $CMRO_2$ ) are the most-well known indicators [87].  $CMR_{Glc}$  measurements in AD research have been well established with positron emission tomography (PET) methods. For instance, significant decreases of glucose metabolism have been found in young APOE  $\epsilon 4$  carriers (30 years old) in brain areas associated with AD pathology [88]. In contrast,  $CMRO_2$  measurements are not feasible using PET methods, especially for AD patients, due to the difficulties of obtaining arterial blood samples. In addition, the radioactive nature of PET allows less repetitive scans, which limits the monitoring of the disease progress. Therefore, considerable efforts have been made to develop MRI-based, noninvasive,  $CMRO_2$  measurements. Baseline  $CMRO_2$  and task-induced changes in  $CMRO_2$  determinations have been proposed by several methods, including  $T_2$ -relaxation-under-spin-tagging (TRUST) and quantitative BOLD (qBOLD) techniques [89–93]. These MR-based metabolic imaging methods, in addition to MRS, are expected to be very useful as diagnostic and prognostic biomarkers in AD. However, future studies allowing for rigorous assessment of test-retest reliability and power calculation compared to the established imaging techniques are necessary before these  $CMRO_2$  methods can be accepted as other complementary and/or established functional neuroimaging biomarkers for AD.

The development and validation of structural and functional biomarkers will enable MRI to be utilized as a powerful tool for evaluation of therapeutic efficacy in AD in large-scale clinical trials. For example, Jack et al. estimated that in each arm of a therapeutic trial with conventional volumetric measures for hippocampal volume, only 21 subjects would be required to detect 50% reduction in the rate of decline. This compares 241 subjects if MMSE scores were used; 320 subjects if ADAS Cog scores were used [54]. Combining with other biomarkers (e.g.,  $CMR_{Glc}$  by PET and  $A\beta$ /NFT CSF), surrogate markers for AD progress can be identified and used for clinical/cognitive tests in clinical trials. Nonetheless, these surrogate markers must be validated to be reproducible in the treatment setting, across various types of treatments, across imaging centers, and across time. A multicenter AD research project, known as the Alzheimer's Disease Neuroimaging Initiative (ANDI) (<http://adni.loni.ucla.edu/>), was launched in 2004 to meet this goal.

## 7. Conclusions

The incidence of Alzheimer's disease is increasing with the extended lifespan in developed countries. The development of neuroimaging biomarkers is a pressing need to detect the early risk of AD (from NC), predict and monitor disease progression (from aMCI). Multimodal MRI methods have been developed to meet this demand by providing useful and important structural and functional biomarkers in AD. The validation of the surrogate biomarkers will have profound implications in AD clinical trials, including the prevention and deceleration of AD onset, as well as the evaluation of treatment efficacy.

## References

- [1] L. E. Hebert, P. A. Scherr, J. L. Bienias, D. A. Bennett, and D. A. Evans, "Alzheimer disease in the US population: prevalence estimates using the 2000 census," *Archives of Neurology*, vol. 60, no. 8, pp. 1119–1122, 2003.
- [2] S. G. Mueller, M. W. Weiner, L. J. Thal et al., "Ways toward an early diagnosis in Alzheimer's disease: the Alzheimer's disease neuroimaging initiative (ADNI)," *Alzheimer's and Dementia*, vol. 1, no. 1, pp. 55–66, 2005.
- [3] R. C. Mohs, D. Marin, and V. Haroutunian, "Early clinical and biological manifestations of Alzheimer's disease: implications for screening and treatment," in *Drug Discovery and Development for Alzheimer's Disease*, H. Fillit and A. W. O'Connell, Eds., Springer, New York, NY, USA, 2002.
- [4] G. B. Frisoni, "Structural imaging in the clinical diagnosis of Alzheimer's disease: problems and tools," *Journal of Neurology Neurosurgery and Psychiatry*, vol. 70, no. 6, pp. 711–718, 2001.
- [5] P. Kochunov, J. F. Mangin, T. Coyle et al., "Age-related morphology trends of cortical sulci," *Human Brain Mapping*, vol. 26, no. 3, pp. 210–220, 2005.
- [6] R. S. Desikan, H. J. Cabral, F. Settecase et al., "Automated MRI measures predict progression to Alzheimer's disease," *Neurobiology of Aging*, vol. 31, no. 8, pp. 1364–1374, 2010.
- [7] R. S. Desikan, H. J. Cabral, C. P. Hess et al., "Automated MRI measures identify individuals with mild cognitive impairment and Alzheimers disease," *Brain*, vol. 132, no. 8, pp. 2048–2057, 2009.
- [8] W. Yang, R. L.M. Lui, J. -H. Gao et al., "Independent component analysis-based classification of Alzheimer's disease MRI data," *Journal of Alzheimer's Disease*, vol. 24, no. 4, pp. 775–783, 2011.
- [9] P. Kochunov, P. M. Thompson, J. L. Lancaster et al., "Relationship between white matter fractional anisotropy and other indices of cerebral health in normal aging: tract-based spatial statistics study of aging," *NeuroImage*, vol. 35, no. 2, pp. 478–487, 2007.
- [10] P. Kochunov, D. E. Williamson, J. Lancaster et al., "Fractional anisotropy of water diffusion in cerebral white matter across the lifespan," *Neurobiology of Aging*. In press.
- [11] B. Biswal, F. Z. Yetkin, V. M. Haughton, and J. S. Hyde, "Functional connectivity in the motor cortex of resting human brain using echo-planar MRI," *Magnetic Resonance in Medicine*, vol. 34, no. 4, pp. 537–541, 1995.
- [12] D. Cordes, V. M. Haughton, K. Arfanakis et al., "Mapping functionally related regions of brain with functional connectivity MR imaging," *American Journal of Neuroradiology*, vol. 21, no. 9, pp. 1636–1644, 2000.

- [13] S. I. Rapoport, "Coupled reductions in brain oxidative phosphorylation and synaptic function can be quantified and staged in the course of Alzheimer disease," *Neurotoxicity Research*, vol. 5, no. 6, pp. 385–397, 2003.
- [14] J. Xiong, L. M. Parsons, J. H. Gao, and P. T. Fox, "Interregional connectivity to primary motor cortex revealed using MRI resting state images," *Human Brain Mapping*, vol. 8, no. 2-3, pp. 151–156, 1999.
- [15] C. F. Beckmann, M. DeLuca, J. T. Devlin, and S. M. Smith, "Investigations into resting-state connectivity using independent component analysis," *Philosophical Transactions of the Royal Society B*, vol. 360, no. 1457, pp. 1001–1013, 2005.
- [16] J. S. Damoiseaux, S. A. R. B. Rombouts, F. Barkhof et al., "Consistent resting-state networks across healthy subjects," *Proceedings of the National Academy of Sciences of the United States of America*, vol. 103, no. 37, pp. 13848–13853, 2006.
- [17] V. Kiviniemi, J. H. Kantola, J. Jauhiainen, A. Hyvärinen, and O. Tervonen, "Independent component analysis of nondeterministic fMRI signal sources," *NeuroImage*, vol. 19, no. 2, pp. 253–260, 2003.
- [18] J. A. Detre, J. S. Leigh, D. S. Williams, and A. P. Koretsky, "Perfusion imaging," *Magnetic Resonance in Medicine*, vol. 23, no. 1, pp. 37–45, 1992.
- [19] H. L. Liu, Y. Pu, Y. Liu et al., "Cerebral blood flow measurement by dynamic contrast MRI using singular value decomposition with an adaptive threshold," *Magnetic Resonance in Medicine*, vol. 42, no. 1, pp. 167–172, 1999.
- [20] W. J. Jagust, "Functional imaging patterns in Alzheimer's disease: relationships to neurobiology," *Annals of the New York Academy of Sciences*, vol. 777, pp. 30–36, 1996.
- [21] G. Waldemar, "Functional brain imaging with SPECT in normal aging and dementia: methodological, pathophysiological, and diagnostic aspects," *Cerebrovascular and Brain Metabolism Reviews*, vol. 7, no. 2, pp. 89–130, 1995.
- [22] M. L. Simmons, C. G. Frondoza, and J. T. Coyle, "Immunocytochemical localization of N-acetyl-aspartate with monoclonal antibodies," *Neuroscience*, vol. 45, no. 1, pp. 37–45, 1991.
- [23] K. Kantarci, R. C. Petersen, B. F. Boeve et al., "1H MR spectroscopy in common dementias," *Neurology*, vol. 63, no. 8, pp. 1393–1398, 2004.
- [24] E. Gómez-Tortosa, M. S. Barquero, M. Barón et al., "Variability of age at onset in siblings with familial Alzheimer disease," *Archives of Neurology*, vol. 64, no. 12, pp. 1743–1748, 2007.
- [25] L. Mosconi, R. Mistur, R. Switalski et al., "Declining brain glucose metabolism in normal individuals with a maternal history of Alzheimer disease," *Neurology*, vol. 72, no. 6, pp. 513–520, 2009.
- [26] L. Mosconi, J. O. Rinne, W. H. Tsui et al., "Increased fibrillar amyloid- $\beta$  burden in normal individuals with a family history of late-onset Alzheimer's," *Proceedings of the National Academy of Sciences of the United States of America*, vol. 107, no. 13, pp. 5949–5954, 2010.
- [27] R. A. Honea, R. H. Swerdlow, E. D. Vidoni, J. Goodwin, and J. M. Burns, "Reduced gray matter volume in normal adults with a maternal family history of Alzheimer disease," *Neurology*, vol. 74, no. 2, pp. 113–120, 2010.
- [28] R. A. Honea, R. H. Swerdlow, E. D. Vidoni, and J. M. Burns, "Progressive regional atrophy in normal adults with a maternal history of Alzheimer disease," *Neurology*, vol. 76, no. 9, pp. 822–829, 2011.
- [29] S. DeBette, P. A. Wolf, A. Beiser et al., "Association of parental dementia with cognitive and brain MRI measures in middle-aged adults," *Neurology*, vol. 73, no. 24, pp. 2071–2078, 2009.
- [30] F. Crivello, H. Lemaitre, C. Dufouil et al., "Effects of ApoE- $\epsilon$ 4 allele load and age on the rates of grey matter and hippocampal volumes loss in a longitudinal cohort of 1186 healthy elderly persons," *NeuroImage*, vol. 53, no. 3, pp. 1064–1069, 2010.
- [31] N. Filippini, M. Zarei, C. F. Beckmann et al., "Regional atrophy of transcallosal prefrontal connections in cognitively normal APOE  $\epsilon$ 4 carriers," *Journal of Magnetic Resonance Imaging*, vol. 29, no. 5, pp. 1021–1026, 2009.
- [32] S. Y. Bookheimer, M. H. Strojwas, M. S. Cohen et al., "Patterns of brain activation in people at risk for Alzheimer's disease," *New England Journal of Medicine*, vol. 343, no. 7, pp. 450–456, 2000.
- [33] N. Filippini, K. P. Ebmeier, B. J. MacIntosh et al., "Differential effects of the APOE genotype on brain function across the lifespan," *NeuroImage*, vol. 54, no. 1, pp. 602–610, 2011.
- [34] G. Douaud, S. Jbabdi, T. E. J. Behrens et al., "DTI measures in crossing-fibre areas: increased diffusion anisotropy reveals early white matter alteration in MCI and mild Alzheimer's disease," *NeuroImage*, vol. 55, no. 3, pp. 880–890, 2011.
- [35] I. Driscoll, C. Davatzikos, Y. An et al., "Longitudinal pattern of regional brain volume change differentiates normal aging from MCI," *Neurology*, vol. 72, no. 22, pp. 1906–1913, 2009.
- [36] T. Gili, M. Cercignani, L. Serra et al., "Regional brain atrophy and functional disconnection across Alzheimer's disease evolution," *Journal of Neurology, Neurosurgery and Psychiatry*, vol. 82, no. 1, pp. 58–66, 2011.
- [37] P. M. Thompson, K. M. Hayashi, R. A. Dutton et al., "Tracking Alzheimer's disease," *Annals of the New York Academy of Sciences*, vol. 1097, pp. 183–214, 2007.
- [38] P. M. Thompson, K. M. Hayashi, G. I. De Zubicaray et al., "Mapping hippocampal and ventricular change in Alzheimer disease," *NeuroImage*, vol. 22, no. 4, pp. 1754–1766, 2004.
- [39] P. M. Thompson, K. M. Hayashi, G. De Zubicaray et al., "Dynamics of gray matter loss in Alzheimer's disease," *Journal of Neuroscience*, vol. 23, no. 3, pp. 994–1005, 2003.
- [40] B. Bosch, E. M. Arenaza-Urquijo, L. Rami et al., "Multiple DTI index analysis in normal aging, amnesic MCI and AD. Relationship with neuropsychological performance," *Neurobiology of Aging*. In press.
- [41] H. Y. Zhang, S. J. Wang, B. Liu et al., "Resting brain connectivity: changes during the progress of Alzheimer disease," *Radiology*, vol. 256, no. 2, pp. 598–606, 2010.
- [42] R. G. Morris and M. D. Kopelman, "The memory deficits in Alzheimer-type dementia: a review," *Quarterly Journal of Experimental Psychology Section A*, vol. 38, no. 4, pp. 575–602, 1986.
- [43] R. J. Caselli, A. C. Dueck, D. Osborne et al., "Longitudinal modeling of age-related memory decline and the APOE  $\epsilon$ 4 effect," *New England Journal of Medicine*, vol. 361, no. 3, pp. 255–263, 2009.
- [44] I. J. Deary, M. C. Whiteman, A. Pattie et al., "Ageing: cognitive change and the APOE  $\epsilon$ 4 allele," *Nature*, vol. 418, no. 6901, p. 932, 2002.
- [45] N. A. Dennis, J. N. Browndyke, J. Stokes et al., "Temporal lobe functional activity and connectivity in young adult APOE  $\epsilon$ 4 carriers," *Alzheimer's and Dementia*, vol. 6, no. 4, pp. 303–311, 2010.
- [46] N. Filippini, B. J. MacIntosh, M. G. Hough et al., "Distinct patterns of brain activity in young carriers of the APOE- $\epsilon$ 4 allele," *Proceedings of the National Academy of Sciences of the United States of America*, vol. 106, no. 17, pp. 7209–7214, 2009.
- [47] Y. I. Sheline, J. C. Morris, A. Z. Snyder et al., "APOE4 allele disrupts resting state fMRI connectivity in the absence

- of amyloid plaques or decreased CSF A $\beta$ 42," *Journal of Neuroscience*, vol. 30, no. 50, pp. 17035–17040, 2010.
- [48] B. Winblad, K. Palmer, M. Kivipelto et al., "Mild cognitive impairment—beyond controversies, towards a consensus: report of the international working group on mild cognitive impairment," *Journal of Internal Medicine*, vol. 256, no. 3, pp. 240–246, 2004.
- [49] J. He, S. Farias, O. Martinez, B. Reed, D. Mungas, and C. DeCarli, "Differences in brain volume, hippocampal volume, cerebrovascular risk factors, and apolipoprotein E4 among mild cognitive impairment subtypes," *Archives of Neurology*, vol. 66, no. 11, pp. 1393–1399, 2009.
- [50] J. T. Becker, S. W. Davis, K. M. Hayashi et al., "Three-dimensional patterns of hippocampal atrophy in mild cognitive impairment," *Archives of Neurology*, vol. 63, no. 1, pp. 97–101, 2006.
- [51] L. G. Apostolova, C. A. Steiner, G. G. Akopyan et al., "Three-dimensional gray matter atrophy mapping in mild cognitive impairment and mild Alzheimer disease," *Archives of Neurology*, vol. 64, no. 10, pp. 1489–1495, 2007.
- [52] P. Kochunov, A. E. Ramage, J. L. Lancaster et al., "Loss of cerebral white matter structural integrity tracks the gray matter metabolic decline in normal aging," *NeuroImage*, vol. 45, no. 1, pp. 17–28, 2009.
- [53] P. Vemuri, H. J. Wiste, S. D. Weigand et al., "Serial MRI and CSF biomarkers in normal aging, MCI, and AD," *Neurology*, vol. 75, no. 2, pp. 143–151, 2010.
- [54] C. R. Jack, M. Slomkowski, S. Gracon et al., "MRI as a biomarker of disease progression in a therapeutic trial of milameline for AD," *Neurology*, vol. 60, no. 2, pp. 253–260, 2003.
- [55] M. L. Schroeter, T. Stein, N. Maslowski, and J. Neumann, "Neural correlates of Alzheimer's disease and mild cognitive impairment: a systematic and quantitative meta-analysis involving 1351 patients," *NeuroImage*, vol. 47, no. 4, pp. 1196–1206, 2009.
- [56] L. L. Chao, S. T. Buckley, J. Kornak et al., "ASL perfusion MRI predicts cognitive decline and conversion from MCI to dementia," *Alzheimer Disease and Associated Disorders*, vol. 24, no. 1, pp. 19–27, 2010.
- [57] H. Braak and E. Braak, "Neuropathological staging of Alzheimer-related changes," *Acta Neuropathologica*, vol. 82, no. 4, pp. 239–259, 1991.
- [58] A. T. Du, N. Schuff, D. Amend et al., "Magnetic resonance imaging of the entorhinal cortex and hippocampus in mild cognitive impairment and Alzheimer's disease," *Journal of Neurology Neurosurgery and Psychiatry*, vol. 71, no. 4, pp. 441–447, 2001.
- [59] D. J. A. Callen, S. E. Black, F. Gao, C. B. Caldwell, and J. P. Szalai, "Beyond the hippocampus: MRI volumetry confirms widespread limbic atrophy in AD," *Neurology*, vol. 57, no. 9, pp. 1669–1674, 2001.
- [60] C. R. Jack Jr., R. C. Petersen, Y. C. Xu et al., "Medial temporal atrophy on MRI in normal aging and very mild Alzheimer's disease," *Neurology*, vol. 49, no. 3, pp. 786–794, 1997.
- [61] Y. Xu, C. R. Jack, P. C. O'Brien et al., "Usefulness of MRI measures of entorhinal cortex versus hippocampus in AD," *Neurology*, vol. 54, no. 9, pp. 1760–1767, 2000.
- [62] S. De Santi, M. J. De Leon, H. Rusinek et al., "Hippocampal formation glucose metabolism and volume losses in MCI and AD," *Neurobiology of Aging*, vol. 22, no. 4, pp. 529–539, 2001.
- [63] N. C. Fox, S. Cousens, R. Scahill, R. J. Harvey, and M. N. Rossor, "Using serial registered brain magnetic resonance imaging to measure disease progression in Alzheimer disease: power calculations and estimates of sample size to detect treatment effects," *Archives of Neurology*, vol. 57, no. 3, pp. 339–344, 2000.
- [64] C. R. Jack Jr., R. C. Petersen, Y. Xu et al., "Rate of medial temporal lobe atrophy in typical aging and Alzheimer's disease," *Neurology*, vol. 51, no. 4, pp. 993–999, 1998.
- [65] J. A. Kaye, T. Swihart, D. Howieson et al., "Volume loss of the hippocampus and temporal lobe in healthy elderly persons destined to develop dementia," *Neurology*, vol. 48, no. 5, pp. 1297–1304, 1997.
- [66] M. P. Laakso, M. Lehtovirta, K. Partanen, P. J. Riekkinen, and H. Soininen, "Hippocampus in Alzheimer's disease: a 3-year follow-up MRI study," *Biological Psychiatry*, vol. 47, no. 6, pp. 557–561, 1999.
- [67] S. M. Resnick, D. L. Pham, M. A. Kraut, A. B. Zonderman, and C. Davatzikos, "Longitudinal magnetic resonance imaging studies of older adults: a shrinking brain," *Journal of Neuroscience*, vol. 23, no. 8, pp. 3295–3301, 2003.
- [68] N. C. Fox and J. M. Schott, "Imaging cerebral atrophy: normal ageing to Alzheimer's disease," *The Lancet*, vol. 363, no. 9406, pp. 392–394, 2004.
- [69] J. L. Gunter, M. M. Shiung, A. Manduca, and C. R. Jack, "Methodological considerations for measuring rates of brain atrophy," *Journal of Magnetic Resonance Imaging*, vol. 18, no. 1, pp. 16–24, 2003.
- [70] A. T. Du, N. Schuff, J. H. Kramer et al., "Higher atrophy rate of entorhinal cortex than hippocampus in AD," *Neurology*, vol. 62, no. 3, pp. 422–427, 2004.
- [71] C. R. Jack Jr., M. M. Shiung, J. L. Gunter et al., "Comparison of different MRI brain atrophy rate measures with clinical disease progression in AD," *Neurology*, vol. 62, no. 4, pp. 591–600, 2004.
- [72] M. J. De Leon, S. Desanti, R. Zinkowski et al., "MRI and CSF studies in the early diagnosis of Alzheimer's disease," *Journal of Internal Medicine*, vol. 256, no. 3, pp. 205–223, 2004.
- [73] A. Convit, M. J. De Leon, C. Tarshish et al., "Specific hippocampal volume reductions in individuals at risk for Alzheimer's disease," *Neurobiology of Aging*, vol. 18, no. 2, pp. 131–138, 1997.
- [74] J. Golomb, A. Kluger, M. J. de Leon et al., "Hippocampal formation size in normal human aging: a correlate of delayed secondary memory performance," *Learning Memory*, vol. 1, no. 1, pp. 45–54, 1994.
- [75] J. P. Lerch, J. C. Pruessner, A. Zijdenbos, H. Hampel, S. J. Teipel, and A. C. Evans, "Focal decline of cortical thickness in Alzheimer's disease identified by computational neuroanatomy," *Cerebral Cortex*, vol. 15, no. 7, pp. 995–1001, 2005.
- [76] D. Tosun, P. Mojabi, M. W. Weiner, and N. Schuff, "Joint analysis of structural and perfusion MRI for cognitive assessment and classification of Alzheimer's disease and normal aging," *NeuroImage*, vol. 52, no. 1, pp. 186–197, 2010.
- [77] D. H. Salat, D. N. Greve, J. L. Pacheco et al., "Regional white matter volume differences in nondemented aging and Alzheimer's disease," *NeuroImage*, vol. 44, no. 4, pp. 1247–1258, 2009.
- [78] J. S. Damoiseaux, S. M. Smith, M. P. Witter et al., "White matter tract integrity in aging and Alzheimer's disease," *Human Brain Mapping*, vol. 30, no. 4, pp. 1051–1059, 2009.
- [79] A. Qiu, K. Oishi, M. I. Miller, C. G. Lyketsos, S. Mori, and M. Albert, "Surface-based analysis on shape and fractional anisotropy of white matter tracts in Alzheimer's disease," *PLoS one*, vol. 5, no. 3, article e9811, 2010.

- [80] R. N. Spreng, R. A. Mar, and A. S. N. Kim, "The common neural basis of autobiographical memory, prospection, navigation, theory of mind, and the default mode: a quantitative meta-analysis," *Journal of Cognitive Neuroscience*, vol. 21, no. 3, pp. 489–510, 2009.
- [81] R. L. Buckner, J. R. Andrews-Hanna, and D. L. Schacter, "The brain's default network: anatomy, function, and relevance to disease," *Annals of the New York Academy of Sciences*, vol. 1124, pp. 1–38, 2008.
- [82] M. D. Greicius, G. Srivastava, A. L. Reiss, and V. Menon, "Default-mode network activity distinguishes Alzheimer's disease from healthy aging: evidence from functional MRI," *Proceedings of the National Academy of Sciences of the United States of America*, vol. 101, no. 13, pp. 4637–4642, 2004.
- [83] D. Royall, J. H. Gao, X. Zhao, M. J. Polk, and D. Kellogg, "Asymmetric insular function predicts positional blood pressure in nondemented elderly," *Journal of Neuropsychiatry and Clinical Neurosciences*, vol. 21, no. 2, pp. 173–180, 2009.
- [84] D. R. Royall, J. H. Gao, and D. L. Kellogg, "Insular Alzheimer's disease pathology as a cause of "age-related" autonomic dysfunction and mortality in the non-demented elderly," *Medical Hypotheses*, vol. 67, no. 4, pp. 747–758, 2006.
- [85] L. L. Chao, N. Schuff, J. H. Kramer et al., "Reduced medial temporal lobe N-acetylaspartate in cognitively impaired but nondemented patients," *Neurology*, vol. 64, no. 2, pp. 282–289, 2005.
- [86] A. Pfefferbaum, E. Adalsteinsson, D. Spielman, E. V. Sullivan, and K. O. Lim, "In vivo brain concentrations of N-acetyl compounds, creatine, and choline in Alzheimer disease," *Archives of General Psychiatry*, vol. 56, no. 2, pp. 185–192, 1999.
- [87] K. Nagata, Y. Kondoh, R. Atchison et al., "Vascular and metabolic reserve in Alzheimer's disease," *Neurobiology of Aging*, vol. 21, no. 2, pp. 301–307, 2000.
- [88] E. M. Reiman, R. J. Caselli, K. Chen, G. E. Alexander, D. Bandy, and J. Frost, "Declining brain activity in cognitively normal apolipoprotein E  $\epsilon$ 4 heterozygotes: a foundation for using positron emission tomography to efficiently test treatments to prevent Alzheimer's disease," *Proceedings of the National Academy of Sciences of the United States of America*, vol. 98, no. 6, pp. 3334–3339, 2001.
- [89] H. An and W. Lin, "Quantitative measurements of cerebral blood oxygen saturation using magnetic resonance imaging," *Journal of Cerebral Blood Flow and Metabolism*, vol. 20, no. 8, pp. 1225–1236, 2000.
- [90] H. Lu and Y. Ge, "Quantitative evaluation of oxygenation in venous vessels using T2-relaxation-under-spin-tagging MRI," *Magnetic Resonance in Medicine*, vol. 60, no. 2, pp. 357–363, 2008.
- [91] D. A. Yablonskiy, "Quantitation of intrinsic magnetic susceptibility-related effects in a tissue matrix. Phantom study," *Magnetic Resonance in Medicine*, vol. 39, no. 3, pp. 417–428, 1998.
- [92] X. He and D. A. Yablonskiy, "Quantitative BOLD: mapping of human cerebral deoxygenated blood volume and oxygen extraction fraction: default state," *Magnetic Resonance in Medicine*, vol. 57, no. 1, pp. 115–126, 2007.
- [93] X. He, M. Zhu, and D. A. Yablonskiy, "Validation of oxygen extraction fraction measurement by qBOLD technique," *Magnetic Resonance in Medicine*, vol. 60, no. 4, pp. 882–888, 2008.

## Research Article

# DTI and MR Volumetry of Hippocampus-PC/PCC Circuit: In Search of Early Micro- and Macrostructural Signs of Alzheimers's Disease

**F. Palesi,<sup>1,2</sup> P. Vitali,<sup>1</sup> P. Chiarati,<sup>1</sup> G. Castellazzi,<sup>1,3</sup> E. Caverzasi,<sup>1</sup> A. Pichiecchio,<sup>1</sup> E. Colli-Tibaldi,<sup>1</sup> F. D'Amore,<sup>1</sup> I. D'Errico,<sup>1</sup> E. Sinforiani,<sup>4</sup> and S. Bastianello<sup>1,5</sup>**

<sup>1</sup>Neuroradiology Unit, IRCCS Foundation National Neurological Institute C. Mondino, 27100 Pavia, Italy

<sup>2</sup>Department of Physics "A. Volta", University of Pavia, 27100 Pavia, Italy

<sup>3</sup>Department of Computer Engineering and Systems Science, University of Pavia, 27100 Pavia, Italy

<sup>4</sup>Neurology Unit, IRCCS Foundation National Neurological Institute C. Mondino, 27100 Pavia, Italy

<sup>5</sup>Department of Radiology, University of Pavia, 27100 Pavia, Italy

Correspondence should be addressed to F. Palesi, fulvia.palesi@unipv.it

Received 15 March 2011; Accepted 7 April 2011

Academic Editor: Patrice Peran

Copyright © 2012 F. Palesi et al. This is an open access article distributed under the Creative Commons Attribution License, which permits unrestricted use, distribution, and reproduction in any medium, provided the original work is properly cited.

Hippocampal damage, by DTI or MR volumetry, and PET hypoperfusion of precuneus/posterior cingulate cortex (PC/PCC) were proposed as biomarkers of conversion from preclinical (MCI) to clinical stage of Alzheimer's disease (AD). This study evaluated structural damage, by DTI and MR volumetry, of hippocampi and tracts connecting hippocampus to PC/PCC (hipp-PC/PCC) in 10 AD, 10 MCI, and 18 healthy controls (CTRL). Normalized volumes, mean diffusivity (MD), and fractional anisotropy (FA) were obtained for grey matter (GM), white matter (WM), hippocampi, PC/PCC, and hipp-PC/PCC tracts. In hippocampi and hipp-PC/PCC tracts, decreased volumes and increased MD were found in AD versus CTRL ( $P < .001$ ). The same results with lower significance ( $P < .05$ ) were found in MCI versus CTRL. Verbal memory correlated ( $P < .05$ ) in AD with left hippocampal and hipp-PC/PCC tract MD, and in MCI with FA of total WM. Both DTI and MR volumetry of hippocampi and hipp-PC/PCC tracts detect early signs of AD in MCI patients.

## 1. Background

Preclinical detection of Alzheimer's disease (AD) is important to start an early therapeutic treatment, and it will be even more crucial in the next few years, as soon as new drugs will be available. Mild cognitive impairment (MCI) is often the preclinical stage of AD. However, some patients with MCI revert to normal cognitive status, while others, with slow disease progression, remain in this prodromic stage without presenting dementia in their life [1].

To detect which patients with MCI will convert in AD in the immediate future, an in vivo biomarker is not currently available. CSF tau, phospho-tau, and amyloid measurements are in development [2, 3] but require lumbar puncture; therefore, a noninvasive imaging marker is more appealing for screening outpatients without hospital admission. With

this purpose, volumetric MRI measures of mesiotemporal atrophy demonstrated to have some prognostic value [4, 5]. Compared to these volumetric measures of macrostructural damage, diffusion tensor imaging (DTI) indexes of microstructural damage within mesiotemporal lobe have shown to better discriminate MCI from controls [6, 7] and to better detect MCI converters [8–10].

DTI is sensitive to both grey and white matter subtle abnormalities. While in AD degeneration mainly affects grey matter [11], recent evidences also found an early white matter involvement [12, 13]. It is a matter of debate whether degeneration directly affects the myelin, but a secondary wallerian degeneration certainly drives disconnection of associative cortical areas from the medial temporal lobe. In MCI, the earliest affected area by disconnection seems to be the precuneus/posterior cingulate cortex (PC/PCC), consistently

TABLE 1: Demographic and neuropsychological features of CTRL, MCI, and AD patients.

Characteristics	CTRL (N = 18)	MCI (N = 10)	AD (N = 10)	*P value	Student's <i>t</i> -test		
					CTRL versus MCI	CTRL versus AD	MCI versus AD
Gender female (n, %)	13, 0.72	5, 0.50	8, 0.80	.325	—	—	—
Age (years)	69.1 ± 5.5	70.8 ± 5.9	72.1 ± 4.8	.273	—	—	—
Verbal memory	11.5 ± 2.2	7.3 ± 3.9	4.7 ± 3.2	<.001	0.001	<0.001	n.s.
MMSE	28.8 ± 1.1	25.5 ± 2.3	22.1 ± 2.7	<.001	<0.001	<0.001	0.007

\* Statistical analysis: Kruskal-Wallis nonparametric comparison;  $P < .05$  is considered significant. Values are expressed in mean ± SD. CTRL: healthy controls; MCI: mild cognitive impairment; AD: Alzheimer's disease; MMSE: mini-mental state examination.

found hypoperfused by many PET studies [14] and related to the conversion in AD [15]. A recent study combining PET and volumetric MRI showed that PC/PCC hypoperfusion follows medial temporal atrophy through posterior cingulum white matter degeneration [16]. Furthermore, several studies using resting state fMRI showed a functional disconnection between hippocampus and PC/PCC [17, 18].

In this study, to identify sensitive *in vivo* biomarkers of risk for conversion from MCI to AD, the microstructural damage was measured by DTI in the hippocampus and in the white matter between hippocampus and PC/PCC. The DTI indexes of microstructural damage were compared to volumetric indexes of macrostructural damage in MCI and AD patients, using as control a group of healthy elderly volunteers.

## 2. Methods

**2.1. Subjects.** Twenty patients were consecutively recruited through the Memory Clinic of the Neurological Institute C. Mondino, Pavia, Italy, among patients suffering from subjective or objective memory complaint.

Exclusion criteria were age > 80, a history of overt depression [19] or other psychiatric diseases, significant cerebrovascular disease [20], and lack of any daily living activity. In this small patients group, exclusion of subjects over 80 years minimizes the contribution of confounding variables of age and of age-related diseases, particularly cerebrovascular disease.

Neuropsychology examination by a standardised battery evaluated different cognitive domain [21]. In this study, we only considered the global measure of cognitive impairment as expressed by MMSE [22], and verbal memory as expressed by short story recall [21].

After clinical and neuropsychological examinations, 10 patients were diagnosed with amnesic mild cognitive impairment [1] and 10 with mild probable Alzheimer's disease (NINCDS2-ARDA criteria [23]) (Table 1).

Twenty elderly subjects were recruited on a volunteer base through a local recreational association ("Argento Vivo," i.e., "Live silver," Bereguardo, PV). After clinical and neuropsychological examinations, two volunteers affected by vascular cognitive impairment were excluded. The remaining 18 healthy volunteers were included as control group (CTRL) and underwent the MRI session.

**2.2. MRI Acquisition.** All data were acquired on a 1.5 Tesla MRI scanner (Intera, Philips Gyroscan, Koninklijke, The Netherlands) using an eight-channel head (SENSE) third-party coil.

All subjects were scanned with a structural MRI protocol, including a dual turbo spin echo (TSE) sequence (proton density and T2), a volumetric T1-weighted sequence, and diffusion tensor imaging (DTI) data. Functional MRI data during resting state are not considered in this study. Additional FLAIR images were acquired only in patients with some punctuate lesions on PD-T2 images. While most patients and volunteers showed some punctuate lesions, only few showed confluent lesions, in any case never involving more than a third of total white matter. Although subtle cerebrovascular disease may be a factor concurring to cognitive impairment in MCI and AD, for the purpose of this study the total lesion load was not assessed.

Diffusion tensor imaging (DTI) data were acquired using a single-shot EPI spin echo sequence (TR/TE = 11800/70 ms) with a *b*-value of 900 s/mm<sup>2</sup>, applying diffusion gradients along 15 directions. Sixty axial slices with no slice gap were acquired (FOV = 224 mm, acquisition matrix = 88 × 90, reconstruction matrix = 96 × 96, 2.5 mm isotropic voxel, number of averages = 3).

Volumetric T1-weighted data was collected using a fast field echo sequence (TR/TE = 8.6/4 ms, flip angle 8°) and one hundred seventy sagittal slices with a thickness of 1.2 mm (FOV = 240 mm, matrix = 192 × 192, in-plane resolution 1.25 × 1.25 mm, reconstruction matrix = 256 × 256).

**2.3. MR Imaging Analysis.** Image analysis was performed on a workstation with Linux Ubuntu 9.10, running SPM8 (Wellcome Department of Cognitive Neurology, <http://www.fil.ion.ucl.ac.uk/>) on MATLAB 7.9 (The MathWorks, Natick, Mass, USA <http://www.mathworks.com/>), FreeSurfer (<http://surfer.nmr.mgh.harvard.edu/>), and FSL (FMRIB Software Library, <http://www.fmrib.ox.ac.uk/fsl/>) software (Figure 1).

A nonparametric nonuniformity intensity normalization was applied on volumetric T1-weighted images [24, 25] using FreeSurfer. Then using FSL [26], the following tools were applied sequentially: brain extraction by the BET [27] tool to clear noncerebral voxels; segmentation by the FAST [28] tool into grey matter (GM), white matter (WM), and cerebrospinal fluid (CSF); segmentation by the FIRST tool

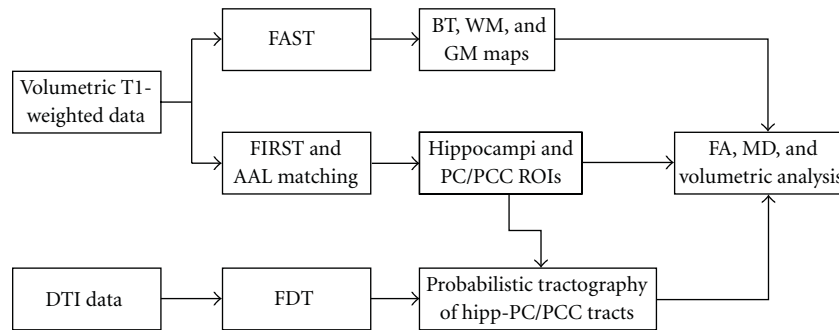


FIGURE 1: Study design schematic. DTI data were preprocessed by FDT (FSL) to obtain MD and FA maps. Structural T1 data were corrected in intensity by FreeSurfer and segmented in brain, grey and white matter volumes by FAST (FSL). Hippocampi and PC/PCC were segmented automatically by FIRST and AAL template registration and then registered on DTI maps. Tracts connecting hippocampus to PC/PCC (hipp-PC/PCC) were identified by probabilistic tractography within FDT and then registered back on structural T1 data. Normalized volumes, MD, and FA values were obtained for GM, WM, hippocampi, PC/PCC, and hipp-PC/PCC tracts.

of left and right hippocampi [29]. Left and right precuneus (PC) and posterior cingulate cortex (PCC) were obtained by an inversion of the nonlinear transformation between the volumetric images and the MNI152 template, on which the AAL template was superimposed.

Diffusion-weighted images were corrected for motion and eddy current distortion by the FDT tool. After brain extraction, diffusion tensor was reconstructed using an iterative least square algorithm (Marquardt-Levenberg nonlinear fit) to calculate mean diffusivity (MD) and fractional anisotropy (FA) maps.

A probabilistic tractography of the tract connecting the hippocampus with PC/PCC (Hipp-PC/PCC) was performed on each hemisphere by the FDT tool [30, 31]; first, volumetric T1-weighted image, ROIs of hippocampi, and PC/PCC were coregistered onto diffusion-weighted images, then coregistered hippocampi were used as seed ROI, and coregistered PC/PCC were used as target ROI. Reconstructed tracts were thresholded at 30.

B0 images were normalized onto the EPI template in stereotaxic MNI152 space for each subject. Normalization transformation was applied to all reconstructed tracts. Normalized nonthresholded tracts were binarized, averaged for the three different groups (CTRL, MCI, and AD patients), and then smoothed with a 5 mm Gaussian kernel.

A voxelwise statistical analysis was performed using the general linear model framework implemented in SPM8 [32]. The resulting t-statistic maps, after family-wise error (FWE) correction for multiple comparisons, were thresholded at  $P < .05$ .

The FA and MD maps were co-registered (with a full affine transformation, FLIRT tool [33]) on volumetric brain-extracted images, then this affine transformation was applied to reconstructed thresholded tracts.

Eventually, average FA and MD were calculated for brain tissue (BT), white matter (WM), grey matter (GM), hippocampi, PC/PCC, and tracts connecting hippocampi with PC/PCC. Absolute volume ( $\text{mm}^3$ ) and relative volume, expressed as ratio between absolute volume ( $\text{mm}^3$ ) and

intracranial volume ( $\text{mm}^3$ ), were calculated for BT, WM, GM, hippocampi, PC/PCC, and tracts connecting hippocampi with PC/PCC.

**2.4. Statistical Analysis.** Statistical analysis was performed using SPSS. Average FA values, average MD, values and volumetric values were statistically compared using a Student *t*-test for nonpaired (independent) data between AD and CTRL, between MCI and CTRL, and between MCI and AD. The significant level was set at  $P \leq .05$  for each test. Finally, a Pearson's correlation analysis was performed between MRI data and cognitive scores (MMSE and verbal memory).

### 3. Results

**3.1. Volumetry Analysis.** Average group values, with respective standard deviations, were reported in Table 2 for relative volumes of each investigated structure. In AD compared to CTRL, volumes of total BT, total GM, and left PC/PCC were significantly decreased ( $P < .05$ ), but even more significantly ( $P = .001$  or less) at the level of both hippocampi and tracts connecting hippocampi with PC/PCC. In MCI compared to CTRL, volumes of both hippocampi and tract connecting right hippocampus with PC/PCC were significantly decreased ( $P < .05$ ) compared to CTRL. In AD compared to MCI, volumes of left PC/PCC and tract connecting left hippocampus with PC/PCC were significantly decreased ( $P < .05$ ) (Figure 2(b)).

**3.2. DTI Analysis.** Average group values, with respective standard deviations, were reported in Table 3 for MD of each investigated structure. In AD compared to CTRL, MD of total BT, total WM, and right PC/PCC were significantly increased ( $P < .05$ ), but more significantly increased ( $P < .001$ ) were MD of total GM, left PC/PCC, both hippocampi and both tracts connecting hippocampi with PC/PCC. In MCI compared to CTRL, MD of both hippocampi and both tracts connecting hippocampi with PC/PCC were significantly increased ( $P < .05$ ). In AD compared to MCI,

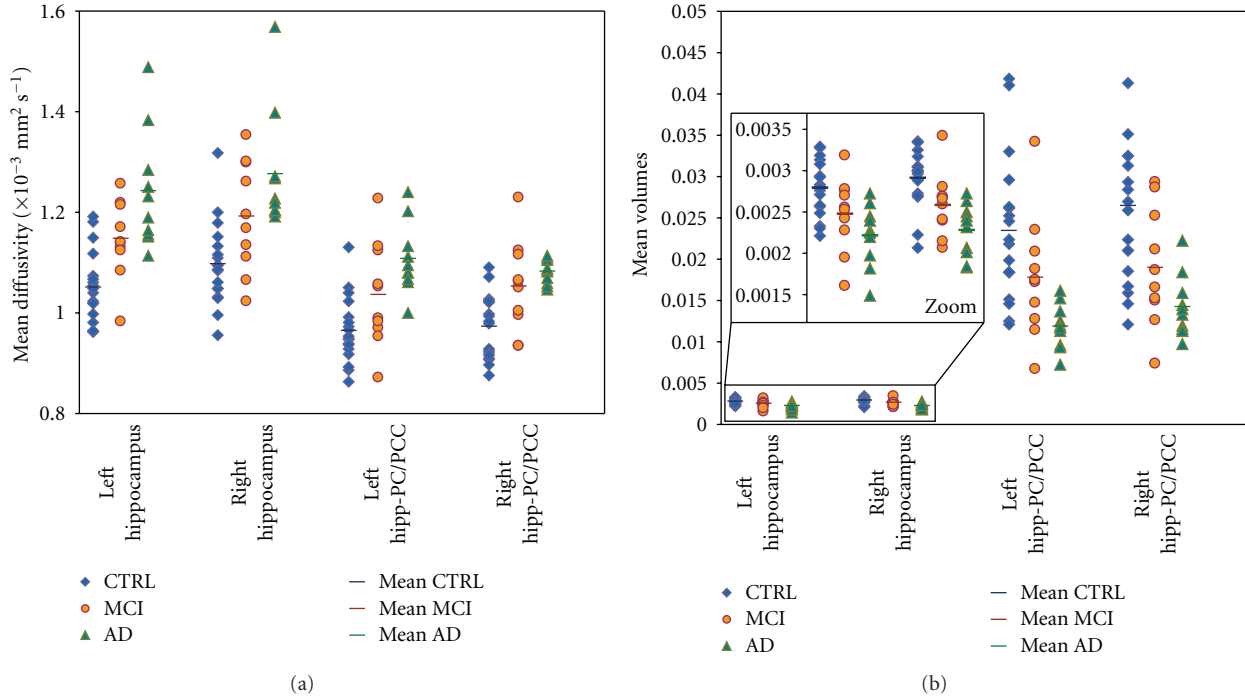


FIGURE 2: Individual data plotting of MD and relative volumes in hippocampi and correlated structures, in order to estimate the ability of the techniques to discriminate AD, MCI, and healthy controls. (a) Plot of MD values for each subject in left and right hippocampus and in left and right tracts connecting hippocampus to PC/PCC for healthy controls (blue), MCI (orange), and AD (green) subjects. Average MD value is represented by a different color line for each group. (b) Plot of relative volumes values for each subject in left and right hippocampus and in left and right tracts connecting hippocampus to PC/PCC for healthy controls (blue), MCI (orange), and AD (green) subjects. Average relative volume value is represented by a different color line for each group.

TABLE 2: Relative volumes in CTRL, MCI, and AD patients.

	CTRL ( <i>N</i> = 18)		MCI ( <i>N</i> = 10)		AD ( <i>N</i> = 10)		Student <i>t</i> -test*		
	Mean	(SD)	Mean	(SD)	Mean	(SD)	CTRL versus MCI	CTRL versus AD	MCI versus AD
Brain tissue	0.7635	(0.0188)	0.7550	(0.0250)	0.6733	(0.1791)	n.s.	0.041	n.s.
White matter	0.3951	(0.0194)	0.3841	(0.0274)	0.3385	(0.0881)	n.s.	n.s.	n.s.
Grey matter	0.3684	(0.0151)	0.3709	(0.0131)	0.3349	(0.0927)	n.s.	0.013	n.s.
Left PC/PCC	0.0141	(0.0009)	0.0145	(0.0016)	0.0132	(0.0012)	n.s.	0.033	0.046
Right PC/PCC	0.0128	(0.0009)	0.0126	(0.0015)	0.0120	(0.0011)	n.s.	n.s.	n.s.
Left hippocampus	0.0028	(0.0003)	0.0025	(0.0004)	0.0022	(0.0004)	0.045	<0.001	n.s.
Right hippocampus	0.0029	(0.0003)	0.0026	(0.0004)	0.0023	(0.0003)	0.029	<0.001	n.s.
Left hipp-PC/PCC	0.0234	(0.0087)	0.0178	(0.0075)	0.0119	(0.0027)	n.s.	<0.001	0.031
Right hipp-PC/PCC	0.0265	(0.0099)	0.0190	(0.0071)	0.0143	(0.0038)	0.047	0.001	n.s.

\* Statistical analysis: Student *t*-test for independent sample; *P* < .05 is considered significant.

Values are expressed in mean (SD). CTRL: healthy controls; MCI: mild cognitive impairment; AD: Alzheimer's disease; n.s.: not significant; Hipp-PC/PCC: hippocampus to PC/PCC tract.

MD of total BT, total GM, and left hippocampus were significantly increased (*P* < .05) (Figure 2(a)).

Average group values, with respective standard deviations, were reported in Table 4 for FA of each investigated structure. In AD compared to CTRL, FA of right hippocampus and tract connecting right hippocampus with PC/PCC were significantly decreased (*P* < .05), but more significantly decreased (*P* < .001 or less) were FA of left hippocampus and

tract connecting left hippocampus with PC/PCC. In MCI compared to CTRL, FA of left hippocampus was the only significantly decreased (*P* < .05) compared to CTRL. In AD compared to MCI, FA of tract connecting left hippocampus with PC/PCC was the only significantly decreased (*P* < .05).

Results of group analysis for tract connecting each hippocampus with homologous PC/PCC are reported in Figures 3 and 4. Figure 3 shows reconstructed tracts in CTRL,

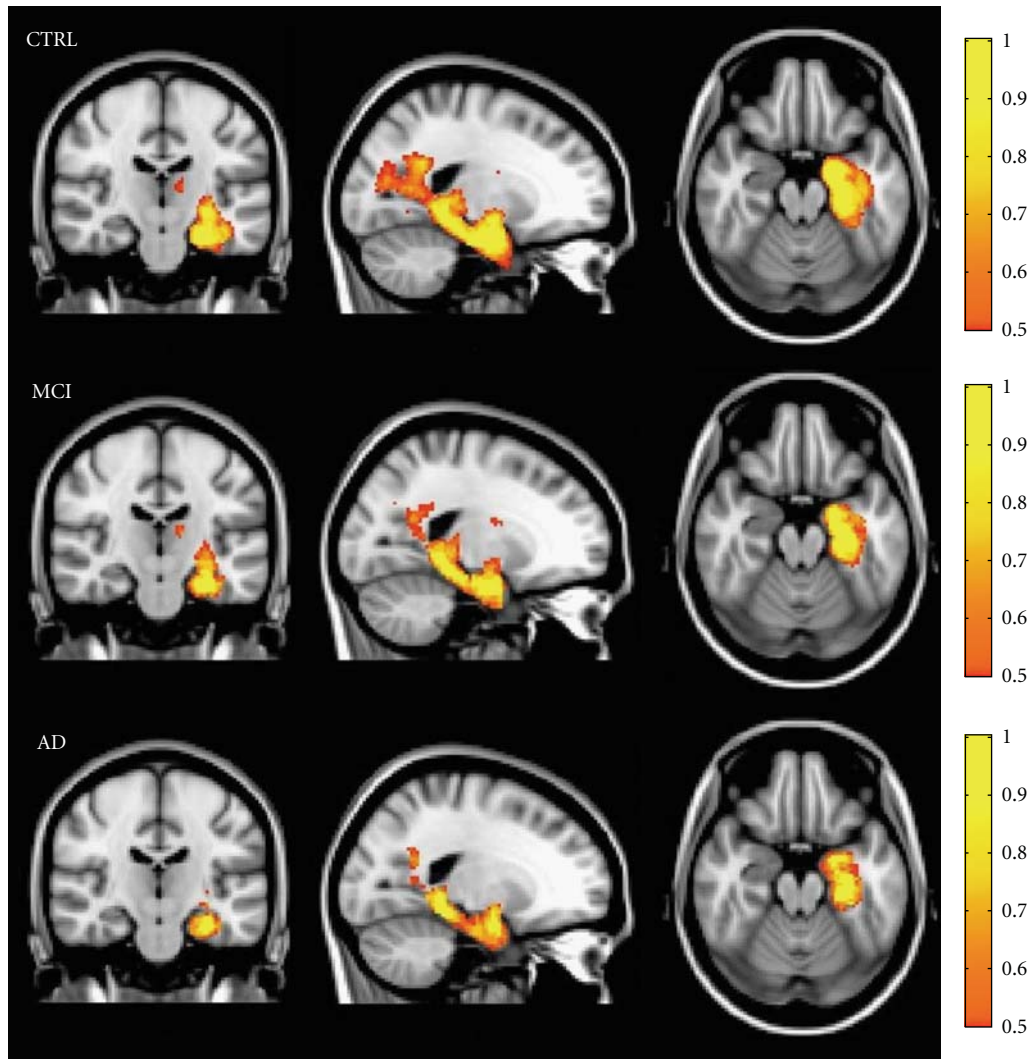


FIGURE 3: Variability maps for the tract connecting hippocampus with PC/PCC (on MNI152 T1-weighted template) in each subjects group. The color intensity indicates the percentage of subjects in whom the tract passes through each voxel. A yellow color scale indicates the higher degree of overlap among subjects; a red-orange color scale indicates that tract is present only in half of the subjects.

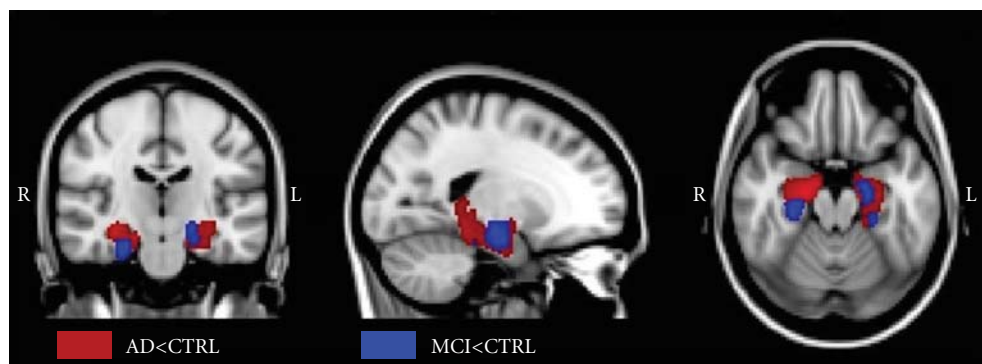


FIGURE 4: Nonparametric statistical results of voxelwise analysis in SPM8, on probability distribution of the tract connecting hippocampus with PC/PCC in MCI patients, AD patients, and healthy controls ( $P < .05$ , FWE correction). The red regions represent the areas in which tract connecting hippocampus with PC/PCC is significantly degenerated in AD patients compared to CTRL. The blue regions represent the areas in which this tract is significantly degenerated in MCI patients compared to CTRL.

TABLE 3: Mean Diffusivity ( $\times 10^{-3} \text{ mm}^2 \text{ s}^{-1}$ ) in CTRL, MCI, and AD patients.

	CTRL ( $N = 18$ )		MCI ( $N = 10$ )		AD ( $N = 10$ )		Student $t$ -test*		
	Mean	(SD)	Mean	(SD)	Mean	(SD)	CTRL versus MCI	CTRL versus AD	MCI versus AD
Brain tissue	0.949	(0.038)	0.967	(0.031)	0.996	(0.026)	n.s.	0.002	0.035
White matter	0.809	(0.030)	0.825	(0.023)	0.833	(0.018)	n.s.	0.025	n.s.
Grey matter	0.979	(0.042)	1.006	(0.037)	1.053	(0.036)	n.s.	<0.001	0.011
Left PC/PCC	1.071	(0.045)	1.097	(0.110)	1.170	(0.078)	n.s.	<0.001	n.s.
Right PC/PCC	1.036	(0.045)	1.077	(0.086)	1.128	(0.096)	n.s.	0.002	n.s.
Left hippocampus	1.051	(0.071)	1.147	(0.078)	1.242	(0.117)	0.003	<0.001	0.047
Right hippocampus	1.097	(0.083)	1.191	(0.110)	1.275	(0.120)	0.016	<0.001	n.s.
Left hipp-PC/PCC	0.965	(0.065)	1.036	(0.104)	1.107	(0.070)	0.034	<0.001	n.s.
Right hipp-PC/PCC	0.972	(0.064)	1.052	(0.091)	1.081	(0.024)	0.011	<0.001	n.s.

\* Statistical analysis: Student  $t$ -test for independent sample;  $P < .05$  is considered significant.

Values are expressed in mean (SD). CTRL: healthy controls; MCI: mild cognitive impairment; AD: Alzheimer's disease; n.s.: not significant; Hipp-PC/PCC: hippocampus to PC/PCC tract.

TABLE 4: Fractional anisotropy in CTRL, MCI, and AD patients.

	CTRL ( $N = 18$ )		MCI ( $N = 10$ )		AD ( $N = 10$ )		Student $t$ -test*		
	Mean	(SD)	Mean	(SD)	Mean	(SD)	CTRL versus MCI	CTRL versus AD	MCI versus AD
Brain tissue	0.207	(0.009)	0.205	(0.008)	0.205	(0.007)	n.s.	n.s.	n.s.
White matter	0.308	(0.017)	0.301	(0.013)	0.305	(0.011)	n.s.	n.s.	n.s.
Grey matter	0.143	(0.007)	0.142	(0.007)	0.139	(0.006)	n.s.	n.s.	n.s.
Left PC/PCC	0.185	(0.017)	0.175	(0.028)	0.174	(0.029)	n.s.	n.s.	n.s.
Right PC/PCC	0.204	(0.021)	0.189	(0.032)	0.190	(0.032)	n.s.	n.s.	n.s.
Left hippocampus	0.134	(0.011)	0.124	(0.012)	0.116	(0.015)	0.032	0.001	n.s.
Right hippocampus	0.133	(0.014)	0.128	(0.012)	0.120	(0.008)	n.s.	0.019	n.s.
Left hipp-PC/PCC	0.215	(0.022)	0.210	(0.025)	0.182	(0.024)	n.s.	0.001	0.019
Right hipp-PC/PCC	0.222	(0.028)	0.205	(0.027)	0.194	(0.019)	n.s.	0.009	n.s.

\* Statistical analysis: Student  $t$ -test for independent sample;  $P < .05$  is considered significant.

Values are expressed in mean (SD). CTRL: healthy controls; MCI: mild cognitive impairment; AD: Alzheimer's disease; n.s.: not significant; Hipp-PC/PCC: hippocampus to PC/PCC tract.

MCI, and AD patients. Variability maps for these tracts show progressive decrease of volume and consistency from CTRL to AD patients.

In Figure 4 are shown the results of voxelwise analysis on probability distribution of the tract connecting each hippocampus with homologous PC/PCC in MCI and AD patients compared with CTRL ( $P < .05$ , FWE correction). In AD (red blobs) patients, probability of connection between hippocampus and PC/PCC was decreased in the whole parahippocampal WM, symmetrically in the two hemispheres. In MCI (blue blobs), probability of connection between hippocampus and PC/PCC was decreased in restricted areas of anterior parahippocampal WM, asymmetrically in the two hemispheres.

**3.3. Correlation between Volumetric and Diffusion MR Indexes (Table 5).** Volume and MD of total BT and total GM were correlated in CTRL and in MCI, not in AD.

Volume and MD, of hippocampi and PC/PCC were correlated in MCI, not in CTRL, and in AD only of the left hippocampus and the right PC/PCC.

Volume, MD and FA of hipp-PC/PCC tracts were correlated in CTRL and in MCI, but in AD, only volume and MD of the left tract.

**3.4. Correlation with Cognitive Scores (Table 6).** In AD, volumes of total BT, volumes of total WM, MD of left hippocampus, and MD of left tract connecting hippocampus with PC/PCC correlate significantly ( $P < .05$ ) with verbal memory scores. MD of left tract connecting hippocampus with PC/PCC was the only parameter correlating also with MMSE score. In MCI, FA of total WM was the only parameter correlating significantly ( $P < .05$ ) with verbal memory. No correlation was found between volumetric or DTI parameters and cognitive scores in CTRL.

## 4. Discussion

The aim of the study was to identify sensitive in vivo biomarkers of Alzheimer's disease, to be employed in clinical setting in single patients and to predict the risk for conversion from MCI to AD. The DTI indexes of microstructural damage showed to be at least as sensitive as volumetric indexes of structural damage to identify mesiotemporal damage in differentiating AD and MCI patients from CTRL. The poor correlation between volume and DTI indexes in AD group suggests that macrostructural and microstructural damage may occur in different times in the course of the disease thus may be differently sensitive.

TABLE 5: Pearson's correlation between volumetric and diffusion MR indexes.

Volumetric variable	Diffusion variable	CTRL ( $N = 18$ )	MCI ( $N = 10$ )	AD ( $N = 10$ )
Volume brain tissue	MD brain tissue	0.001	<0.001	n.s.
Volume grey matter	MD grey matter	0.001	0.008	n.s.
Volume left PC/PCC	MD left PC/PCC	n.s.	0.014	n.s.
Volume right PC/PCC	MD right PC/PCC	n.s.	0.004	0.004
Volume left hippocampus	MD left hippocampus	n.s.	0.001	0.002
Volume right hippocampus	MD right hippocampus	n.s.	0.003	n.s.
	FA right hippocampus	0.036	n.s.	n.s.
Volume left hipp-PC/PCC	MD left hipp-PC/PCC	<0.001	<0.001	0.002
	FA left hipp-PC/PCC	<0.001	0.015	n.s.
Volume right hipp-PC/PCC	MD right hipp-PC/PCC	<0.001	<0.001	n.s.
	FA right hipp-PC/PCC	0.004	0.002	n.s.

Statistical analysis: 2-tailed Pearson's correlation;  $P < .05$  is considered significant.

Only significant correlations were reported. MCI: mild cognitive impairment; AD: Alzheimer's Disease; n.s.: not significant; Hipp-PC/PCC: hippocampus to PC/PCC tract.

TABLE 6: Pearson's Correlation between MR indexes and cognitive scores.

	MCI ( $N = 10$ )		AD ( $N = 10$ )	
	Verbal memory	MMSE	Verbal memory	MMSE
Relative BT volume	n.s.	n.s.	0.031	n.s.
Relative WM volume	n.s.	n.s.	0.019	n.s.
MeanFA BT	0.045	n.s.	n.s.	n.s.
MeanMD left hippocampus	n.s.	n.s.	0.048	n.s.
MeanMD left hipp-PC/PCC	n.s.	n.s.	0.029	0.037

Statistical analysis: 2-tailed Pearson's correlation;  $P < .05$  is considered significant.

Only significant correlations were reported. MCI: mild cognitive impairment; AD: Alzheimer's disease; n.s.: not significant; MMSE: mini-mental state examination; Hipp-PC/PCC: hippocampus to PC/PCC tract.

In AD, and to less extent in MCI, atrophy and MD increases were found not only in both hippocampi, but also very significant in white matter tracts connecting hippocampi with precuneus/posterior cingulate cortex. To our knowledge, no study assessed simultaneously atrophy and diffusivity in both hippocampus and parahippocampal-posterior cingulum tract.

We observed also a significant decrease of FA in the hipp-PC/PCC tracts in AD the left tract significantly more than in MCI. The volume of this left hipp-PC/PCC tract, and the volume of left PC/PCC were also found more significantly decreased in AD than in MCI. These results could be explained by a degenerative damage in hipp-PC/PCC tracts, secondary to hippocampal damage. This degenerative damage in hipp-PC/PCC tracts, in agreement with the Villain model, could drive the PC/PCC dysconnection, thus causing in these cortical areas first hypoperfusion in MCI (as found commonly by PET studies, included Villain et al.) and later MD increase and atrophy in AD (as found in the present study, mainly in the left hemisphere). The portion of

cingulate tract identified by Villain is included in the tract connecting hippocampi with precuneus/posterior cingulate cortex in our study.

These significant DTI differences between MCI and CTRL groups are not consistently found in literature. Among several DTI studies in MCI, hippocampal MD increase in MCI was found only by few authors [6, 7, 10]. Some studies also found that hippocampal MD detects MCI converters better than hippocampal atrophy [8, 10]. Compared to Muller and Scola, our approach uses a more precise segmentation, specifically of the whole hippocampus as performed in Ray, 2006. While Ray, 2006, used a manual segmentation, our approach with automatic segmentation, still capable to detect early abnormalities in hippocampus of MCI patients, may be more feasible in a clinical setting. Among DTI studies in MCI focusing on white matter tracts, an MD increase in parahippocampal-posterior cingulum was found by few recent studies [34, 35].

It is not known whether damage of parahippocampal-posterior cingulum is the crucial abnormality in MCI converting to AD or not. In the present study, although MD of total BT and total GM differentiated AD from MCI, other significant differences between AD and MCI were found in MD of left hippocampus, FA and volume of left hipp-PC/PCC tract, and volume of left PC/PCC. Therefore, the hippocampus-PC/PCC circuit seems to be specifically involved in AD. While a study using a voxelwise approach [36] failed to find significant MD increase in any white matter region in MCI, the main white matter region with MD increase in early AD was the parahippocampal tract. Another study of the same group, using an ROI-based approach, found that the occipital white matter was found to be the region differentiating better MCI converters from MCI non converters [10]. In that study, however, posterior cingulum and parahippocampal tract were not investigated.

About clinical relevance of volumetric and DTI abnormalities, we looked at correlations with cognitive variables, verbal memory, and MMSE scores. Verbal memory impairment is the earlier crucial deficit in MCI and AD. In this study, in AD the verbal memory score correlated with indexes

of global atrophy (total BT, total WM) and at mesiotemporal level only with MD increase, not with atrophy, of left hippocampus and tract connecting left hippocampus with PC/PCC. The clinical relevance of MD increases is also supported by the finding that MD of the tract connecting left hippocampus with PC/PCC was the only variable correlating also with scale of global cognitive status, as expressed by MMSE. In this study, in MCI the verbal memory score correlated only with FA of total WM. Because all MCI patients in this cohort were amnesic MCI, verbal memory was affected in them all, but only few are likely to develop AD in the next years. Therefore, in MCI the correlation of verbal memory score with FA of total WM may reflect a pathological mechanism not specifically related to the Alzheimer's pathology, for instance, to a generic WM damage due to a subtle cerebrovascular disease.

## 5. Conclusions

Both MR volumetric measure of macrostructural damage and DTI measure of microstructural damage, both in grey and white matter, are candidates to be sensitive in vivo biomarkers of mesiotemporal damage predicting conversion from MCI to AD.

DTI abnormalities, especially MD increase, seem to be more clinically relevant than atrophy.

Only the clinical followup of MCI patients will show which is the most sensitive parameter to be employed to predict the conversion rate on single patients in a clinical setting.

## Acknowledgments

The authors thank Federica Negri and all volunteers of the local recreational association "Argento Vivo" (i.e., "Live silver") in Bereguardo, PV, Italy, particularly their president, Rampi Teresita, for the enthusiastic support to this study.

## References

- [1] R. C. Petersen, G. E. Smith, S. C. Waring, R. J. Ivnik, E. G. Tangalos, and E. Kokmen, "Mild cognitive impairment: clinical characterization and outcome," *Archives of Neurology*, vol. 56, no. 3, pp. 303–308, 1999.
- [2] B. Palumbo, D. Siepi, I. Sabalich, C. Tranfaglia, and L. Parnetti, "Cerebrospinal fluid neuron-specific enolase: a further marker of Alzheimer's disease?" *Functional Neurology*, vol. 23, no. 2, pp. 93–96, 2008.
- [3] A. Caroli and G. B. Frisoni, "The dynamics of Alzheimer's disease biomarkers in the Alzheimer's disease neuroimaging initiative cohort," *Neurobiology of Aging*, vol. 31, no. 8, pp. 1263–1274, 2010.
- [4] P. Calvini, A. Chincarini, G. Gemme et al., "Automatic analysis of medial temporal lobe atrophy from structural MRIs for the early assessment of Alzheimer disease," *Medical Physics*, vol. 36, no. 8, pp. 3737–3747, 2009.
- [5] L. K. McEvoy, C. Fennema-Notestine, J. C. Roddey et al., "Alzheimer disease: quantitative structural neuroimaging for detection and prediction of clinical and structural changes in mild cognitive impairment," *Radiology*, vol. 251, no. 1, pp. 195–205, 2009.
- [6] M. J. Müller, D. Greverus, C. Weibrich et al., "Diagnostic utility of hippocampal size and mean diffusivity in amnesic MCI," *Neurobiology of Aging*, vol. 28, no. 3, pp. 398–403, 2007.
- [7] K. M. Ray, H. Wang, Y. Chu et al., "Mild cognitive impairment: apparent diffusion coefficient in regional gray matter and white matter structures," *Radiology*, vol. 241, no. 1, pp. 197–205, 2006.
- [8] A. Fellgiebel, P. R. Dellani, D. Greverus, A. Scheurich, P. Stoeter, and M. J. Müller, "Predicting conversion to dementia in mild cognitive impairment by volumetric and diffusivity measurements of the hippocampus," *Psychiatry Research—Neuroimaging*, vol. 146, no. 3, pp. 283–287, 2006.
- [9] K. Kantarci, R. C. Petersen, B. F. Boeve et al., "DWI predicts future progression to Alzheimer disease in amnesic mild cognitive impairment," *Neurology*, vol. 64, no. 5, pp. 902–904, 2005.
- [10] E. Scola, M. Bozzali, F. Agosta et al., "A diffusion tensor MRI study of patients with MCI and AD with a 2-year clinical follow-up," *Journal of Neurology, Neurosurgery and Psychiatry*, vol. 81, no. 7, pp. 798–805, 2010.
- [11] H. Braak and E. Braak, "Diagnostic criteria for neuropathologic assessment of Alzheimer's disease," *Neurobiology of Aging*, vol. 18, no. 4, pp. S85–S88, 1997.
- [12] G. Bartzokis, "Age-related myelin breakdown: a developmental model of cognitive decline and Alzheimer's disease," *Neurobiology of Aging*, vol. 25, no. 1, pp. 5–18, 2004.
- [13] X. J. Sun, Q. C. Lu, and Y. Cai, "Effect of cholecystokinin on experimental neuronal aging," *World Journal of Gastroenterology*, vol. 11, no. 4, pp. 551–556, 2005.
- [14] K. Herholz, S. F. Carter, and M. Jones, "Positron emission tomography imaging in dementia," *British Journal of Radiology*, vol. 80, no. 2, pp. S160–S167, 2007.
- [15] S. Morbelli, A. Piccardo, G. Villavecchia et al., "Mapping brain morphological and functional conversion patterns in amnesic MCI: a voxel-based MRI and FDG-PET study," *European Journal of Nuclear Medicine and Molecular Imaging*, vol. 37, no. 1, pp. 36–45, 2010.
- [16] N. Villain, M. Fouquet, J. C. Baron et al., "Sequential relationships between grey matter and white matter atrophy and brain metabolic abnormalities in early Alzheimer's disease," *Brain*, vol. 133, no. 11, pp. 3301–3314, 2010.
- [17] M. D. Greicius, G. Srivastava, A. L. Reiss, and V. Menon, "Default-mode network activity distinguishes Alzheimer's disease from healthy aging: evidence from functional MRI," *Proceedings of the National Academy of Sciences of the United States of America*, vol. 101, no. 13, pp. 4637–4642, 2004.
- [18] C. Sorg, V. Riedl, R. Pernecky, A. Kurz, and A. M. Wohlschläger, "Impact of Alzheimer's disease on the functional connectivity of spontaneous brain activity," *Current Alzheimer Research*, vol. 6, no. 6, pp. 541–553, 2009.
- [19] M. Hamilton, "Development of a rating scale for primary depressive illness," *The British Journal of Social and Clinical Psychology*, vol. 6, no. 4, pp. 278–296, 1967.
- [20] V. C. Hachinski, L. D. Iliff, and E. Zilhka, "Cerebral blood flow in dementia," *Archives of Neurology*, vol. 32, no. 9, pp. 632–637, 1975.
- [21] H. Spinnler and G. Tognoni, "Taratura e standardizzazione italiana di test neuropsicologici," *Italian Journal of Neurological Sciences*, supplement 8, pp. 1–120, 1987.
- [22] M. F. Folstein, S. E. Folstein, and P. R. McHugh, "Mini mental state". A practical method for grading the cognitive state of

- patients for the clinician,” *Journal of Psychiatric Research*, vol. 12, no. 3, pp. 189–198, 1975.
- [23] G. McKhann, D. Drachman, and M. Folstein, “Clinical diagnosis of Alzheimer’s disease: report of the NINCDS-ADRDA work group under the auspices of department of health and human services task force on alzheimer’s disease,” *Neurology*, vol. 34, no. 7, pp. 939–944, 1984.
- [24] J. G. Sled, A. P. Zijdenbos, and A. C. Evans, “A nonparametric method for automatic correction of intensity nonuniformity in mri data,” *IEEE Transactions on Medical Imaging*, vol. 17, no. 1, pp. 87–97, 1998.
- [25] W. Zheng, M. W. L. Chee, and V. Zagorodnov, “Improvement of brain segmentation accuracy by optimizing non-uniformity correction using N3,” *NeuroImage*, vol. 48, no. 1, pp. 73–83, 2009.
- [26] S. M. Smith, M. Jenkinson, M. W. Woolrich et al., “Advances in functional and structural MR image analysis and implementation as FSL,” *NeuroImage*, vol. 23, supplement 1, pp. S208–S219, 2004.
- [27] S. M. Smith, “Fast robust automated brain extraction,” *Human Brain Mapping*, vol. 17, no. 3, pp. 143–155, 2002.
- [28] Y. Zhang, M. Brady, and S. Smith, “Segmentation of brain MR images through a hidden Markov random field model and the expectation-maximization algorithm,” *IEEE Transactions on Medical Imaging*, vol. 20, no. 1, pp. 45–57, 2001.
- [29] B. Patenaude, S. M. Smith, D. N. Kennedy, and M. Jenkinson, “A Bayesian model of shape and appearance for subcortical brain segmentation,” *NeuroImage*. In press.
- [30] T. E. J. Behrens, H. J. Berg, S. Jbabdi, M. F. S. Rushworth, and M. W. Woolrich, “Probabilistic diffusion tractography with multiple fibre orientations: what can we gain?” *NeuroImage*, vol. 34, no. 1, pp. 144–155, 2007.
- [31] T. E. J. Behrens, M. W. Woolrich, M. Jenkinson et al., “Characterization and propagation of uncertainty in diffusion-weighted MR imaging,” *Magnetic Resonance in Medicine*, vol. 50, no. 5, pp. 1077–1088, 2003.
- [32] O. Ciccarelli, A. T. Toosy, G. J. M. Parker et al., “Diffusion tractography based group mapping of major white-matter pathways in the human brain,” *NeuroImage*, vol. 19, no. 4, pp. 1545–1555, 2003.
- [33] M. Jenkinson and S. Smith, “A global optimisation method for robust affine registration of brain images,” *Medical Image Analysis*, vol. 5, no. 2, pp. 143–156, 2001.
- [34] I. L. H. Choo, D. Y. Lee, J. S. Oh et al., “Posterior cingulate cortex atrophy and regional cingulum disruption in mild cognitive impairment and Alzheimer’s disease,” *Neurobiology of Aging*, vol. 31, no. 5, pp. 772–779, 2010.
- [35] K. Kiuchi, M. Morikawa, T. Taoka et al., “Abnormalities of the uncinate fasciculus and posterior cingulate fasciculus in mild cognitive impairment and early Alzheimer’s disease: a diffusion tensor tractography study,” *Brain Research*, vol. 1287, pp. 184–191, 2009.
- [36] F. Agosta, M. Pievani, S. Sala et al., “White matter damage in Alzheimer disease and its relationship to gray matter atrophy,” *Radiology*, vol. 258, no. 3, pp. 853–863, 2011.

## Review Article

# Understanding the Pathophysiology of Alzheimer's Disease and Mild Cognitive Impairment: A Mini Review on fMRI and ERP Studies

**Takao Yamasaki,<sup>1,2</sup> Hiroyuki Muranaka,<sup>3</sup> Yumiko Kaseda,<sup>4</sup> Yasuyo Mimori,<sup>5</sup> and Shozo Tobimatsu<sup>1</sup>**

<sup>1</sup> Department of Clinical Neurophysiology, Neurological Institute, Graduate School of Medical Sciences, Kyushu University, 3-1-1 Maidashi, Higashi-ku, Fukuoka 812-8582, Japan

<sup>2</sup> Department of Neurology, Minkodo Minohara Hospital, 3553 Kanaide, Sasaguri-machi, Kasuya-gun, Fukuoka 811-2402, Japan

<sup>3</sup> Department of Radiology, Hiroshima City General Rehabilitation Center, 1-39-1 Tomo-minami, Asaminami-ku, Hiroshima 731-3168, Japan

<sup>4</sup> Department of Neurology, Hiroshima City General Rehabilitation Center, 1-39-1 Tomo-minami, Asaminami-ku, Hiroshima 731-3168, Japan

<sup>5</sup> Department of Physical Therapy, Faculty of Health Sciences, Hiroshima International University, 555-36 Gakuennndai, Kurose, Higashihiroshima, Hiroshima 739-2695, Japan

Correspondence should be addressed to Takao Yamasaki, yamasa@neurophy.med.kyushu-u.ac.jp

Received 15 March 2011; Revised 11 May 2011; Accepted 15 May 2011

Academic Editor: Antonio Cerasa

Copyright © 2012 Takao Yamasaki et al. This is an open access article distributed under the Creative Commons Attribution License, which permits unrestricted use, distribution, and reproduction in any medium, provided the original work is properly cited.

The prevalence of Alzheimer's disease (AD) is predicted to increase rapidly in the coming decade, highlighting the importance of early detection and intervention in patients with AD and mild cognitive impairment (MCI). Recently, remarkable advances have been made in the application of neuroimaging techniques in investigations of AD and MCI. Among the various neuroimaging techniques, functional magnetic resonance imaging (fMRI) has many potential advantages, noninvasively detecting alterations in brain function that may be present very early in the course of AD and MCI. In this paper, we first review task-related and resting-state fMRI studies on AD and MCI. We then present our recent fMRI studies with additional event-related potential (ERP) experiments during a motion perception task in MCI. Our results indicate that fMRI, especially when combined with ERP recording, can be useful for detecting spatiotemporal functional changes in AD and MCI patients.

## 1. Introduction

Dementia is one of the most serious conditions associated with longevity, and represents a pressing public health problem. Alzheimer's disease (AD) is the most common form of dementia, affecting millions of people around the world. AD is a progressive neurodegenerative disorder, resulting in a gradual, irreversible loss of memory and cognitive function [1]. Recently recognized as the prodromal stage of AD, mild cognitive impairment (MCI) represents a transitional period between normal aging and AD [2, 3]. MCI pathology can reveal the early stages of AD, including neuritic plaques, neurofibrillary tangles, and loss

of basal forebrain cholinergic neurons [4]. As a subtype of MCI, amnesic MCI constitutes a syndrome presenting with cognitive decline that is more pronounced than expected for the individual's age and educational level, but does not fulfill the criteria for AD. Patients with amnesic MCI have a high risk of AD progression, with a 10–15% yearly transition rate [5]. In addition, large numbers of novel compounds, which have the potential to modify the course of AD and slow its progression, are currently under development. However, there is currently no cure for the disease. For this reason, there is an urgent need for biomarkers to detect MCI.

In the past two decades, several functional imaging techniques have been used to investigate changes in brain

function in patients with AD and MCI. Functional magnetic resonance imaging (fMRI), positron emission tomography (PET) and single-photon emission computed tomography (SPECT) are effective methods. Among these techniques, fMRI has a number of potential advantages for examining patients with AD and MCI, since it is noninvasive, does not require the injection of contrast agent, and has much higher spatial resolution than PET or SPECT. Furthermore, fMRI can be conducted many times over the course of a longitudinal study, and thus lends itself as an appropriate measure in clinical drug trials. Therefore, fMRI is likely to be particularly useful for detecting alterations in brain function that may be present very early in the course of AD and MCI. The measurement of event-related potentials (ERPs) represents a useful objective tool, and has been employed extensively in studying the physiology and pathophysiology of human brain function [6]. ERPs are characterized by extremely high temporal resolution, and can allow non-invasive assessment of synaptic dysfunction in the human brain [7]. Thus, the use of fMRI and ERPs together can provide a powerful tool for examining functional brain abnormalities in AD and MCI.

In this article, we first review previous fMRI studies on AD and MCI. We then present the findings of our recent fMRI studies with additional ERP recording experiments during a motion perception task in MCI patients.

## 2. fMRI Findings in AD and MCI

fMRI has been used to investigate abnormalities in patterns of regional brain activation during a variety of cognitive tasks in patients with AD and MCI. In particular, difficulty in the formation and retention of new episodic memories is typically the earliest and most salient clinical symptom of AD [8–10]. Even in the early stages of the disease, many patients with AD also exhibit visuospatial deficits [11–13]. A large number of fMRI studies have examined memory and visual tasks relative to other types of cognitive task. Furthermore, the recently developed method of measuring resting-state (rs-)fMRI has been used to examine resting brain function in AD and MCI patients [14–16]. Below we review studies using task-related (i.e., during memory and visual tasks) fMRI, as well as rs-fMRI studies in patients with AD and MCI.

**2.1. Memory Networks.** The term “memory” represents a simplified summarization of a wide-ranging set of different associated functions, including short-term, long-term, procedural, declarative, semantic, and episodic memory. Memory can be subdivided into functions related either to the encoding or retrieval of information. The term “declarative memory” refers to the aspect of human memory involved in the storage of facts and experiences, which can be explicitly discussed or declared by the individual. Declarative memory is subdivided into semantic memory (noncontext specific fact, word and object memory) and episodic memory (memory of events, including time, place, and associated emotions). In patients with AD, episodic memory is among the earliest affected functions [8–10]. AD typically results

in a deficit in the establishment of new episodic memories whereas events dating from more remote periods in the past are better preserved. In the later stages of AD, most other memory domains are also affected. As such, memory impairment is also a fundamental criterion of the diagnosis of AD [17].

The functional neuroanatomy of memory is currently widely believed that many memory functions are tightly linked to distributed regions in the brain. In particular, a neural system in the medial temporal lobe (MTL), including the hippocampal region, and the adjacent perirhinal, entorhinal and parahippocampal cortices, is thought to be involved in encoding and retrieving episodic memory [18–20]. In addition, the prefrontal cortical regions, temporoparietal junction, posterior cingulate cortex, and the cerebellum have been identified as contributing to episodic memory [20, 21]. In general, brain regions in the left hemisphere (particularly the hippocampus) appear to be more involved in encoding while the right hemisphere (particularly the prefrontal cortex) appears to be more engaged in the retrieval of episodic memory [22]. A specific set of regions, termed the “default mode network” (DMN) has been recently proposed to play a key role in memory, on the basis of rs-fMRI findings [23, 24]. The DMN includes the posterior cingulate, extending into the precuneus, lateral parietal, and medial prefrontal regions. This network has been shown to be more metabolically active at rest, decreasing its activity during challenging cognitive tasks. Interestingly, recent fMRI studies have suggested that the DMN needs to be disengaged or “deactivated” during successful memory formation [25, 26].

In patients with AD, a number of fMRI studies have reported decreased activation in the MTL region compared with older healthy subjects during episodic encoding tasks [27–29] (for a review, see Sperling and colleagues [8–10, 30]). A recent quantitative meta-analysis [31] demonstrated decreased activation of memory encoding-related regions (hippocampal formation, ventrolateral prefrontal cortex, precuneus, cingulate gyrus, and lingual gyrus) in AD patients. Other fMRI studies have also suggested that the DMN exhibits markedly abnormal responses during memory tasks in AD patients [32, 33]. Interestingly, the regions demonstrating aberrant DMN activity overlap anatomically with regions showing a high amyloid burden in early AD [34].

Regarding MCI patients, fMRI results have been markedly variable, ranging from findings of hyperactivation [27, 35] to hypoactivation [36, 37] of the MTL region. This variability in the results of previous studies is thought to be closely related to two factors; first, differences in subjects’ ability to perform the fMRI task, and second, differences in the severity of the cognitive impairment along a continuum between normal aging and dementia [30]. MTL hyperactivation may be a compensatory response to maintain memory performance in the setting of early AD pathology [30]. As in AD, there is evidence that areas of the DMN are significantly affected in subjects with MCI relative to controls [32, 38]. A more recent study using a face-name memory task reported that a quantitative goodness-of-fit index of DMN connectivity was able to distinguish MCI

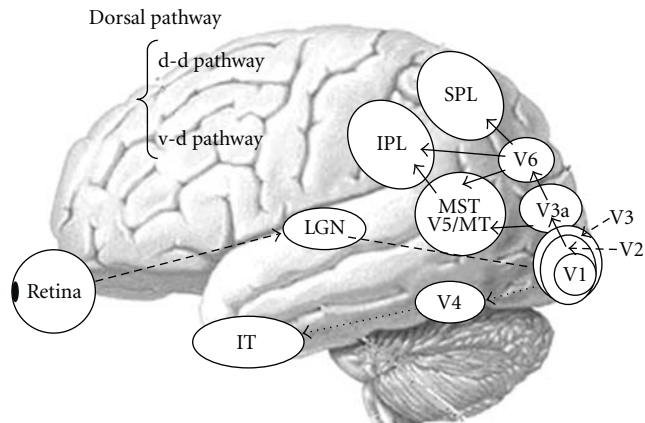


FIGURE 1: The parallel visual pathways in humans. Abbreviations in this and subsequent figures: d-d pathway, dorsodorsal pathway; v-d pathway, ventrodorsal pathway; LGN: lateral geniculate nucleus; V1, 2, 3, 4, and 6, primary, secondary, tertiary, quaternary, and senary visual cortices; V3a, V3 accessory; V5/MT: quinary visual cortex/middle temporal area; MST: medial superior temporal area; IPL, inferior parietal lobule, SPL: superior parietal lobule; IT: inferior temporal cortex.

patients who converted to AD from those who remained stable over a 2- to 3-year follow-up period [39].

**2.2. Visuospatial Perception.** Besides impairment of episodic memory, higher visual dysfunction is one of the cognitive hallmarks of AD [40]. Various visual functions, including the perception of objects, faces, words, and visuospatial stimuli are impaired in AD. However, deficits of visuospatial perception (i.e., the perception of space and motion) are the most prominent. Such deficits play a critical role in the navigational impairment found in AD and MCI [41–43].

Visual information is processed via parallel channels, namely, the parvocellular (P) and magnocellular (M) pathways [44] (for review, see Tobimatsu and Celesia [6]). Both systems begin in the retina and project to the primary visual cortex (V1) via the lateral geniculate nucleus. From V1, the P-pathway projects to the ventral stream, which includes V4 and the inferior temporal cortex. This system is responsible for processing form and color [6, 44]. Conversely, after V1, the M-pathway projects to the dorsal stream, which includes V3a, V5/MT+ (V5/MT and MST), V6, and the posterior parietal lobule. This system plays an important role in detecting space and motion information [6, 44]. Recently, one study reported that the dorsal stream is divided into two functional streams: the dorsodorsal (d-d) and ventrodorsal (v-d) streams [45]. The former consists of V6 and the superior parietal lobule (SPL) whereas the latter is formed by V5/MT and the inferior parietal lobule (IPL). Another series of studies demonstrated that macaque V6 is connected with visual areas including V1-3, V3a, V5/MT+, SPL, and IPL [46, 47]. A schematic diagram of the parallel visual pathways is shown in Figure 1. The distribution of neurofibrillary tangles and amyloid deposits in the visual system in typical AD has been described. Neurofibrillary tangles have been found in the visual association areas while amyloid plaques were

reported to be uniformly distributed across the primary and association visual areas [4, 48–51]. In areas along the dorsal pathway, there is a significant loss of long corticocortical projections from early visual areas to V5 [52]. Thus, it is likely that the dorsal visual pathway is more susceptible to putative AD-related neuropathological changes than in the ventral pathway.

Based on the findings mentioned above, several fMRI studies have been conducted to elucidate the neural basis of visuospatial impairment in AD patients [53–55]. Information regarding motion perception is independently described in the next section (Section 2.3). Thulborn et al. [53] demonstrated a reduction in right parietal activation while perceiving a visual saccade task. Similarly, Prvulovic et al. [54] reported reduced activation in the SPL, and compensatory recruitment of occipitotemporal cortex (ventral pathway) during the angle discrimination task. Bokde et al. [55] investigated the function of the parallel visual pathways in healthy controls and AD patients, finding that the control group exhibited selective activation of the ventral and dorsal pathways during face- and location-matching tasks. However, no such selective activation was observed in the AD group. Instead, the AD group recruited additional activation in the parietal and frontal lobes during the location-matching task. In contrast, there was no significant difference in activation between the two groups during the face-matching task. These fMRI results thus support the notion that the dorsal visual pathway is more susceptible to putative AD-related neuropathological changes than in the ventral pathway.

In a study of MCI patients, Bokde et al. [57] measured activation changes in the parallel visual pathways using face matching and location-matching tasks. The healthy control group but not the MCI group exhibited selective activation of the ventral and dorsal pathways during the face- and location-matching tasks. During the face-matching task, there was no significant difference in activation between the two groups. However, both visual pathways were activated in the MCI group, possibly reflecting a compensatory mechanism, and increased activation was observed in the left frontal lobe during the location-matching task. Vannini et al. [58] investigated visuospatial processing in progressive and stable MCI patients during an angle discrimination task with varying task demands. Compared with stable MCI patients and controls, progressive MCI patients exhibited a stronger relationship between task demand and brain activity in the left SPL. The authors concluded that increased parietal activation in progressive MCI patients could reflect a reduction in neuronal efficacy in the dorsal pathway due to accumulating AD pathology.

**2.3. Motion Perception.** To our knowledge, there have been two fMRI studies investigating motion perception in AD (but not MCI) patients [59, 60]. Thiyagesh et al. [59] used depth and motion stimuli, reporting that an AD group exhibited hypoactivation in V5, SPL, parietooccipital cortex, and the premotor cortices, as well as greater compensatory activation in IPL. Thiyagesh et al. [60] also examined the treatment effects of acetylcholinesterase inhibitors in AD

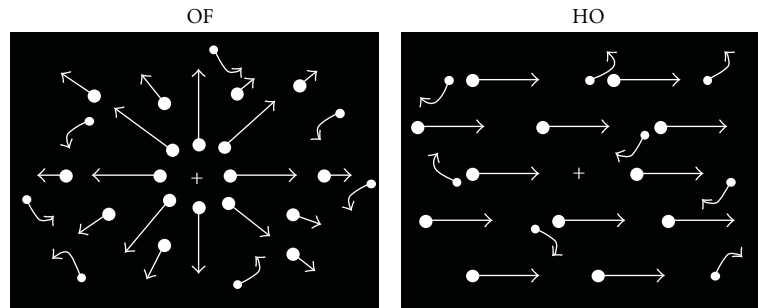


FIGURE 2: Visual motion stimuli. Four hundred white square dots (visual angle,  $0.2 \times 0.2^\circ$ ; luminance,  $48 \text{ cd/m}^2$ ) were randomly presented on a black background (visual angle,  $50 \times 48^\circ$ ; luminance,  $0.1 \text{ cd/m}^2$ ). The contrast level was 99.6%. The white dots moved at a velocity of  $5.0^\circ/\text{s}$ . When the white dots move incoherently, random motion stimulation is created. When the white dots move coherently, OF and HO are perceived. Abbreviations in this and subsequent figures: HO: horizontal motion; OF: optic flow (adapted from Yamasaki et al., in press [56]).

patients, recording fMRI while subjects performed motion perception tasks. They reported increased activation in the left precuneus, left cuneus, left supramarginal gyrus, right parieto-temporal cortex and right IPL after treatment. Furthermore, increased activation in the left precuneus was found to correlate significantly with improved functioning in terms of activities of daily living. These findings suggest that fMRI scanning during motion perception tasks could be useful for monitoring the efficacy of disease modifying therapies. However, further fMRI studies are necessary to elucidate the neural basis of impaired motion perception in patients with AD and MCI.

Motion information is mainly processed by the dorsal stream including V3a, V5/MT+ (V5/MT and MST), V6, and the posterior parietal lobule [6, 44–47, 61]. In particular, the lateral motion area V5/MT+ (V5/MT and MST) and medial motion area V6 have been recently considered key structures in extrastriate motion processing [61]. Human V5/MT+ is functionally and anatomically located in the depths of the anterior occipital sulcus (the ascending limb of the inferior temporal sulcus) and the anterior portions of either the inferior lateral occipital or the inferior occipital sulcus. V5/MT has a high density of motion-sensitive neurons. V1 neurons have small receptive fields that can detect local motion. The properties of V5/MT neurons include larger receptive fields than V1, center-surround interactions, integration of different directions, and sensitivity to motion coherence. Taken together, these findings suggest that V5/MT integrates local motion signals from V1 into the more global representations of motion needed as a basis for perceptual performance. Projections from V5/MT into the neighboring MST area and into the parietal lobe appear to provide a good neural substrate for the use of visual motion in the control of eye movements and other actions (for review, see Tobimatsu and Celesia [6]; Yamasaki et al. [56]).

Recent findings have led to V6 being considered an additional medial motion area [61], located in the parieto-occipital sulcus of macaques and humans. In macaques, V6 abuts the end (the representation of the far periphery) of V3 and V3a. It has a clear retinotopic organization, representing the contralateral hemifield. Most of its cells are visually

responsive, and approximately 75% are direction sensitive. Similar to V5/MT+ cells, the receptive field of cells in V6 is much larger than that of cells in V1. Adjacent area V6a, which occupies the dorsal/anterior portion of the sulcus, has no obvious retinotopic organization and only around 60% of the neurons are visually responsive. Visual neurons are again predominantly motion sensitive. These findings suggest that macaque V6 and V6a play a pivotal role in providing visual motion information to the motor system. Similarly, human V6 is confined to the dorsal portion of the parieto-occipital sulcus, occupying the fundus and posterior bank of the sulcus. This area contains a complete representation of the contralateral hemifield, with the lower field located medially and more anterior to V3/V3a, extending dorsally to the upper field. As in primates, human V6 responds to coherent more than incoherent motion (for review, see Fattori et al. [46]).

Many types of motion stimuli have been applied to examine motion processing in healthy humans and several neurological disorders. In particular, coherent motion stimuli using random dots have been widely used in psychophysical, electrophysiological, and neuroimaging studies to investigate global motion processing [62–64]. There are several types of global motion, including radial optic flow (OF) and horizontal motion (HO; Figure 2). Radial OF, the visual motion perceived during observer self-movement, is particularly important for daily life because it provides cues about the direction and three-dimensional structure of the visual environment [65, 66] (for review, see Tobimatsu and Celesia [6]; Yamasaki et al. [56]). In primates, MST and posterior parietal neurons have been found to selectively respond to OF [67, 68] while V5/MT neurons do not appear to exhibit such specific selectivity [69]. Several neuropsychological studies have reported that patients with AD exhibited impaired radial OF perception, associated with visuospatial disorientation, but preserved HO perception [70, 71]. Some patients with MCI have also been found to exhibit selective impairments in OF perception [43]. These findings suggest differential processing of OF and HO. fMRI studies with healthy subjects have demonstrated that several areas within the dorsal streams are activated by OF [64, 72–74]. However, it remains unknown how OF and HO are differentially processed within

the two distinct dorsal streams (the v-d and d-d streams) in healthy subjects as well as in patients with cognitive decline.

**2.4. Brain Connectivity in the Resting State.** As mentioned above, a number of fMRI studies have revealed that patterns of activation or deactivation during task performance are altered in AD and MCI patients. However, these task-based imaging paradigms require the active participation of subjects, which may be difficult for some AD and MCI patients, depending on the task demands involved. This problem can be resolved by the development of rs-fMRI, a technique that has attracted substantial research attention. rs-fMRI signals are thought to reflect spontaneous neuronal activity and/or the endogenous/background neurophysiological processes of the brain in the resting state [75–77]. Because no stimulation or task-related responses are required, this method has practical advantages for clinical applications and can be used easily even for patients with severe dementia [14]. Various methods exist for analyzing rs-fMRI data: seed region of interest (ROI) based on functional connectivity analysis, independent components analysis, clustering, pattern classification, graph theoretical analysis, and “local” methods, including the measurement of regional homogeneity. The characteristics of each of these methods have been described in detail elsewhere (for a review, see Margulies et al. [78]).

Spontaneous brain activity is thought to be organized by synchronized oscillations at different temporal and spatial scales [79]. Temporal correlations between low-frequency oscillations of fMRI signals derived from distinct brain areas at rest reflect the spatial aspects of this organization. Biswal et al. [75] reported the first such findings of at-rest functional connectivity in the somatomotor system in healthy subjects. Since then, rs-networks have been reported for many functional systems, including the motor, primary sensory, language, attention, and DMN systems [80–84]. In the past several years, many researchers have begun to study the pathophysiology of AD and MCI by investigating changes in rs-fMRI signals (for a review see Liu et al. [14], Sorg et al. [15], and Filippi and Agosta [16]). An rs-fMRI study using seed ROI analysis demonstrated disrupted left-right hippocampal connectivity in AD patients [85]. Other seed-ROI rs-fMRI studies of AD patients reported altered connectivity between the hippocampus and several neocortical regions including the posterior cingulate cortex (PCC), lateral temporal cortex, medial, and lateral prefrontal cortices, and inferior parietal cortex [86–88]. A study of MCI patients revealed decreased functional connectivity between the PCC and temporal cortex compared to controls [89]. Whole-brain analyses of MCI patients have also reported diffuse alterations of connectivity in the DMN compared with healthy elderly controls [90, 91]. For example, Sorg et al. [90] revealed decreased DMN connectivity not only in the PCC and the bilateral parietal cortex, but also in the right medial prefrontal cortex. Qi et al. [91] reported decreased functional activity in regions associated with the DMN, including the bilateral precuneus/PCC, right IPL and left fusiform gyrus, and a trend towards decreased right medial temporal lobe activity. In contrast, enhanced rs-functional connectivity in frontal regions has been reported

in AD patients [92–94]. Increased functional connectivity between regions of the DMN and frontal areas has also been reported in AD [93] and MCI patients [89, 91]. These findings suggest that patients with AD may rely on increased prefrontal connectivity to compensate for reduced temporal lobe function.

Disruption of global functional organization has also been reported in AD [92, 94]. Wang et al. [94] found that AD patients exhibited decreased positive correlations of activity between the prefrontal and parietal lobes, but increased positive correlations within the prefrontal, parietal, and occipital lobes. These findings provide further evidence for the notion that anterior-posterior disconnection and increased within-lobe functional connectivity occur in AD. Supekar et al. [92] investigated small-world properties in the brain, namely, the clustering coefficients and characteristic path lengths of 90 brain nodes in AD patients, as indices of global functional organization. Clustering coefficients are considered a measure of local network connectivity, and networks with high average clustering coefficients are characterized by densely connected local clusters. The characteristic path length is a measure of how well connected a network is. A network with a low characteristic path length exhibits short distances between any two nodes. Small-world networks are characterized by a high clustering coefficient and a low characteristic path length. Based on graph theoretical analysis, AD patients were found to exhibit a loss of small-world properties in the brain, with a significant reduction in the clustering coefficient. This finding suggests the involvement of disrupted local connectivity in the disease [92]. In addition, a trend towards randomness in brain networks in AD was recently reported by Sanz-Arigita et al. [95] using graph analysis. A post hoc analysis of regional synchronization revealed increased synchronization in AD involving the frontal cortices and occipital regions. This translates into a global reduction of functional long-distance links between frontal and caudal brain regions.

Recently, Chen et al. [96] succeeded in classifying patients as AD, MCI, and cognitively normal subjects using a large-scale network analysis. The altered connectivity patterns among the cortical networks were significantly correlated with the results of cognitive tests. Zhang et al. [97] investigated alterations in PCC functional connectivity by comparing a healthy control group with three separate AD groups (mild, moderate, and severe AD) using a method of temporal correlation. They found that modulation of the DMN with abnormal PCC connectivity was able to change along with AD stage progression. Thus, changes in functional connectivity of the resting brain may provide an imaging marker for monitoring AD progression.

### **3. fMRI with Additional ERP Recording in Motion Perception**

fMRI is characterized by excellent spatial resolution, but low temporal resolution. Thus, it can only discriminate between events that are separated by several seconds. In contrast, the temporal resolution of ERPs is in the order of milliseconds,

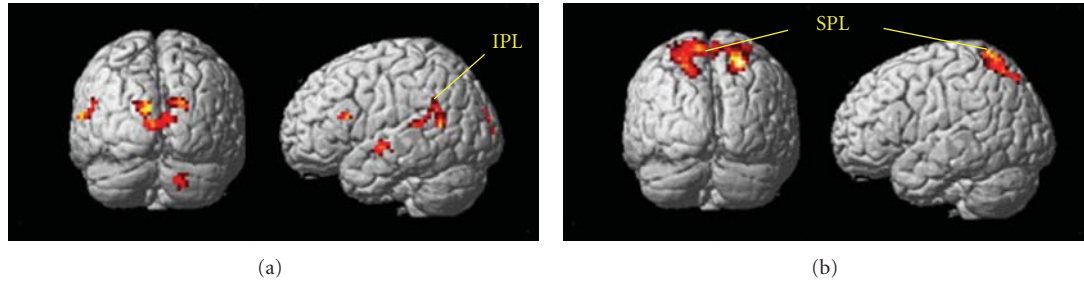


FIGURE 3: fMRI responses in healthy young adults. (a) Activations of the v-d pathway including the IPL (BA 39/40) are found in the OF minus HO condition. (b) The HO minus OF condition shows the activation of the d-d pathway, including the SPL (BA 7; adapted from Yamasaki et al., in press [56]).

which is far superior to that of other neuroimaging methods including fMRI. However, ERPs offer poor spatial resolution compared with fMRI. Based on these characteristics, the combined use of fMRI and ERPs is considered to be an extremely useful technique for evaluating the spatiotemporal functional changes in AD and MCI in detail. In the following section, we summarize the findings of our studies using fMRI and separate ERP measurement during the performance of motion perception tasks in healthy controls and MCI patients [56, 98–102].

**3.1. Two Distinct Motion Pathways.** As stated in Section 2.3, it is currently unclear how coherent OF and HO are differently processed in the v-d and d-d streams in humans. We first examined the neural basis of motion perception in healthy young adults by measuring fMRI and visual ERPs during the perception of coherent OF and HO stimuli [56, 98–102]. In our fMRI experiments, we used a block design rather than an event-related design to detect subtle differences in BOLD signals between the responses to the two types of motion stimuli. To complement temporal information associated with neural activity, high-density 128-channel ERPs were separately recorded. Our visual stimuli consisted of 400 white square dots randomly presented on a black background. The white dots moved at a velocity of 5.0 degrees of visual angle per second. The dots in the HO stimuli moved leftward or rightward while those in the OF stimuli moved radially in an outward pattern (Figure 2). The coherence level was 90% for both types of stimuli. We used random motion (RM) as a baseline in our analysis to suppress the neural activity of nondirectional neurons. When fMRI was recorded during OF and HO perception, the OF stimulus significantly activated the v-d stream, including the IPL (BA 39/40) in the OF minus RM-baseline and OF minus HO contrasts (Figure 3(a)). There was no significant activation in other motion areas, such as V3a, V5/MT+, V6, and the d-d stream (SPL) in either contrast. On the contrary, the d-d stream, including the SPL (BA 7) was significantly activated during perception of the HO stimulus in the HO minus RM-baseline and the HO minus OF contrasts (Figure 3(b)). However, significant activations of V3a, V5/MT+, and the v-d stream (IPL) were not observed in either contrast. These findings indicate that OF and HO motions are processed differently within the dorsal stream. The d-d stream (SPL) appears to

be more closely related to HO motion processing while the v-d stream (IPL) is important for OF motion processing [56, 98, 102]. In addition, the lack of activation in V3a, V5/MT+ and V6 suggests that these brain regions do not distinguish between RM (or incoherent), coherent OF, and HO motion. Previous studies have reported that the v-d stream, including the IPL, plays crucial roles in high-level motion perception, space perception, and action organization [45, 103, 104]. Conversely, the SPL is highly responsive to unidirectional coherent motion stimuli [105]. Therefore, the IPL appears to play an important role in complex OF processing while activity in the SPL is related to the processing of simple unidirectional motion.

Using the same motion stimuli, we conducted several experiments using high-density 128-channel ERP recording. The results revealed that perception of these stimuli was associated with two major ERP components (N170, P200; Figure 4). The occipitotemporal N170 had a V5/MT origin, and was evoked by both types of stimuli [56, 98]. In contrast, the parietal P200 originated in IPL (BA 40) and was only elicited by OF stimuli [56, 98]. These findings indicate that the N170 component is a nonspecific, motion-related component originating from V5/MT, while the P200 is an OF-specific component generated by the IPL [56, 98]. Thus, our ERP studies provided further evidence suggesting a close relationship between the v-d stream (IPL) and OF perception. On the basis of these findings, we conclude that different types of spatiotemporal processing are driven by OF and HO motion stimuli within two distinct dorsal streams in healthy young adults.

**3.2. Effects of Aging and Cognitive Decline on Motion Perception.** Based on our previous fMRI and ERP findings in healthy young adults [56, 98], we conducted a preliminary investigation of motion perception in healthy older elderly adults and MCI patients. In fMRI, healthy elderly adults showed similar activation patterns to healthy young adults. That is, OF stimulus perception dominantly activated the v-d stream (IPL) while the d-d stream (SPL) was more strongly activated by HO stimuli. Interestingly, in MCI patients, IPL activation in response to OF stimuli was decreased compared to healthy elderly adults. In contrast, there was no apparent difference in SPL activation for HO between healthy old adults and MCI patients. These results imply that

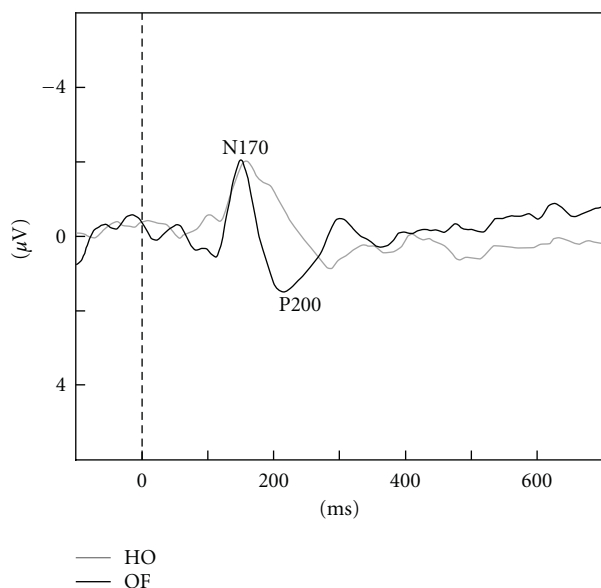


FIGURE 4: ERP responses in healthy young adults. Two major components (N170, P200) were observed. The N170 was evoked by both HO and OF stimuli while the P200 was only elicited by OF stimuli (adapted from Yamasaki et al., in press [56]).

the function of the v-d stream (IPL) is selectively impaired in MCI while d-d (SPL) function appears to be preserved.

Two major ERP components (N170, P200) were detected during this task in both healthy old adults and MCI patients, as observed in healthy young adults [98]. MCI patients exhibited prolonged OF-specific P200 latencies compared to healthy elderly adults, but no differences were found in N170 latency. This finding suggests that the function of the v-d stream (IPL) related to OF perception is selectively impaired in MCI patients, consistent with fMRI findings. These results are in accord with the functional importance of the IPL in MCI patients [106]. Taken together, our findings provide evidence that fMRI with additional ERP recording can be useful for detecting spatiotemporal functional changes in the brain, including the IPL, in MCI patients.

#### 4. Conclusion

The most prominent symptoms of MCI and AD are memory loss and visuospatial impairments. The task-related fMRI studies discussed in this review demonstrated specific alterations of several brain functions, such as memory networks and visuospatial perception. Decreased activation in the distributed networks including the MTL and DMN has been observed during the encoding of new memories. Alteration of memory networks can distinguish AD converters of MCI from nonconverters. During visuospatial perception, the activation of the dorsal pathway was reduced in conjunction with compensatory activation in the ventral pathway and frontal regions. Repeated fMRI scanning during a visuospatial task revealed enhanced activation in the dorsal stream after treatment. This activation was correlated with improvements on neuropsychological assessments. Studies utilizing

the recent development of rs-fMRI have also demonstrated altered functional connectivity within the hippocampus, DMN, and larger-scale networks. Changes in the functional connectivity of the resting brain have been successfully used in the classification of patients with AD, MCI, and the healthy elderly. Taken together, the studies reviewed above indicate that fMRI is useful as an early diagnostic aid for AD and MCI patients. Furthermore, fMRI is a potentially useful method for monitoring the progression of disease and the efficacy of disease-modifying therapies. Unfortunately, the temporal resolution of fMRI is far inferior to that of ERPs. By recording both fMRI and ERP activity in response to the same motion stimuli, we revealed spatiotemporal functional changes of the IPL in MCI patients during coherent motion perception. Therefore, the use of ERPs appears to provide additional information about spatiotemporal functional changes in MCI.

#### Acknowledgments

This paper was supported in part by Grants-in-Aid for Scientists, no. 18890131 and no. 20591026, from the Ministry of Education, Culture, Sports, Science, and Technology in Japan. The authors would like to thank Drs. Tsuyoshi Torii, Tomohiko Ohshita, Takafumi Miyachi, Tetsuya Takahashi, Masayasu Matsumoto, Jun-ichi Kira, Yasumasa Ohyagi, Yoshinobu Goto, Takayuki Taniwaki, Akira Monji, Shigenobu Kanba, Shinji Munetsuna, Takashi Yoshiura, Katsuya Ogata, Kensuke Sasaki, Ikue Ijichi, and Yuka Miyanaga for their research assistance.

#### References

- [1] S. Salloway and S. Correia, "Alzheimer disease: time to improve its diagnosis and treatment," *Cleveland Clinic Journal of Medicine*, vol. 76, no. 1, pp. 49–58, 2009.
- [2] R. C. Petersen, G. E. Smith, S. C. Waring, R. J. Ivnik, E. G. Tangalos, and E. Kokmen, "Mild cognitive impairment: clinical characterization and outcome," *Archives of Neurology*, vol. 56, no. 3, pp. 303–308, 1999.
- [3] K. Ritchie and J. Touchon, "Mild cognitive impairment: conceptual basis and current nosological status," *The Lancet*, vol. 355, no. 9199, pp. 225–228, 2000.
- [4] H. Braak and E. Braak, "Neuropathological staging of Alzheimer-related changes," *Acta Neuropathologica*, vol. 82, no. 4, pp. 239–259, 1991.
- [5] R. C. Petersen, R. Doody, A. Kurz et al., "Current concepts in mild cognitive impairment," *Archives of Neurology*, vol. 58, no. 12, pp. 1985–1992, 2001.
- [6] S. Tobimatsu and G. G. Celesia, "Studies of human visual pathophysiology with visual evoked potentials," *Clinical Neurophysiology*, vol. 117, no. 7, pp. 1414–1433, 2006.
- [7] I. A. Cook and A. F. Leuchter, "Synaptic dysfunction in Alzheimer's disease: clinical assessment using quantitative EEG," *Behavioural Brain Research*, vol. 78, no. 1, pp. 15–23, 1996.
- [8] B. C. Dickerson and R. A. Sperling, "Functional abnormalities of the medial temporal lobe memory system in mild cognitive impairment and Alzheimer's disease: insights from functional MRI studies," *Neuropsychologia*, vol. 46, no. 6, pp. 1624–1635, 2008.

- [9] B. C. Dickerson and R. A. Sperling, "Large-scale functional brain network abnormalities in Alzheimer's disease: insights from functional neuroimaging," *Behavioural Neurology*, vol. 21, no. 1-2, pp. 63–75, 2009.
- [10] R. A. Sperling, B. C. Dickerson, M. Pihlajamäki et al., "Functional alterations in memory networks in early Alzheimer's disease," *NeuroMolecular Medicine*, vol. 12, no. 1, pp. 27–43, 2010.
- [11] M. Rizzo and M. Nawrot, "Perception of movement and shape in Alzheimer's disease," *Brain*, vol. 121, no. 12, pp. 2259–2270, 1998.
- [12] S. J. Tetewsky and C. J. Duffy, "Visual loss and getting lost in Alzheimer's disease," *Neurology*, vol. 52, no. 5, pp. 958–965, 1999.
- [13] M. F. Mendez, M. M. Cherrier, and R. S. Meadows, "Depth perception in Alzheimer's disease," *Perceptual and Motor Skills*, vol. 85, no. 3, pp. 987–995, 1996.
- [14] Y. Liu, K. Wang, C. YU et al., "Regional homogeneity, functional connectivity and imaging markers of Alzheimer's disease: a review of resting-state fMRI studies," *Neuropsychologia*, vol. 46, no. 6, pp. 1648–1656, 2008.
- [15] C. Sorg, V. Riedl, R. Pernecky, A. Kurz, and A. M. Wohlschläger, "Impact of Alzheimer's disease on the functional connectivity of spontaneous brain activity," *Current Alzheimer Research*, vol. 6, no. 6, pp. 541–553, 2009.
- [16] M. Filippi and F. Agosta, "Structural and functional network connectivity breakdown in Alzheimer's disease studied with magnetic resonance imaging techniques," *Journal of Alzheimer's Disease*, vol. 24, no. 3, pp. 455–474, 2011.
- [17] G. McKhann, D. Drachman, M. Folstein, R. Katzman, D. Price, and E. M. Stadlan, "Clinical diagnosis of Alzheimer's disease: report of the NINCDS-ADRDA work group under the auspices of department of health and human services task force on Alzheimer's disease," *Neurology*, vol. 34, no. 7, pp. 939–944, 1984.
- [18] L. R. Squire, "Memory systems of the brain: a brief history and current perspective," *Neurobiology of Learning and Memory*, vol. 82, no. 3, pp. 171–177, 2004.
- [19] L. R. Squire, C. E. Stark, and R. E. Clark, "The medial temporal lobe," *Annual Review of Neuroscience*, vol. 27, pp. 279–306, 2004.
- [20] B. Desgranges, J. C. Baron, and F. Eustache, "The functional neuroanatomy of episodic memory: the role of the frontal lobes, the hippocampal formation, and other areas," *Neuroimage*, vol. 8, no. 2, pp. 198–213, 1998.
- [21] E. Svoboda, M. C. McKinnon, and B. Levine, "The functional neuroanatomy of autobiographical memory: a meta-analysis," *Neuropsychologia*, vol. 44, no. 12, pp. 2189–2208, 2006.
- [22] E. Tulving, S. Kapur, F. I. Craik, M. Moscovitch, and S. Houle, "Hemispheric encoding/retrieval asymmetry in episodic memory: positron emission tomography findings," *Proceedings of the National Academy of Sciences of the United States of America*, vol. 91, no. 6, pp. 2016–2020, 1994.
- [23] M. E. Raichle, A. M. MacLeod, A. Z. Snyder, W. J. Powers, D. A. Gusnard, and G. L. Shulman, "A default mode of brain function," *Proceedings of the National Academy of Sciences of the United States of America*, vol. 98, no. 2, pp. 676–682, 2001.
- [24] R. L. Buckner, J. R. Andrews-Hanna, and D. L. Schacter, "The brain's default network: anatomy, function, and relevance to disease," *Annals of the New York Academy of Sciences*, vol. 1124, pp. 1–38, 2008.
- [25] S. M. Daselaar, S. E. Prince, and R. Cabeza, "When less means more: deactivations during encoding that predict subsequent memory," *Neuroimage*, vol. 23, no. 3, pp. 921–927, 2004.
- [26] S. L. Miller, E. Fenstermacher, J. Bates, D. Blacker, R. A. Sperling, and B. C. Dickerson, "Hippocampal activation in adults with mild cognitive impairment predicts subsequent cognitive decline," *Journal of Neurology, Neurosurgery and Psychiatry*, vol. 79, no. 6, pp. 630–635, 2008.
- [27] S. A. Small, G. M. Perera, R. DeLaPaz, R. Mayeux, and Y. Stern, "Differential regional dysfunction of the hippocampal formation among elderly with memory decline and Alzheimer's disease," *Annals of Neurology*, vol. 45, no. 4, pp. 466–472, 1999.
- [28] A. Golby, G. Silverberg, E. Race et al., "Memory encoding in Alzheimer's disease: an fMRI study of explicit and implicit memory," *Brain*, vol. 128, no. 4, pp. 773–787, 2005.
- [29] F. Rémy, F. Mirrashed, B. Campbell, and W. Richter, "Verbal episodic memory impairment in Alzheimer's disease: a combined structural and functional MRI study," *Neuroimage*, vol. 25, no. 1, pp. 253–266, 2005.
- [30] R. Sperling, "Functional MRI studies of associative encoding in normal aging, mild cognitive impairment, and Alzheimer's disease," *Annals of the New York Academy of Sciences*, vol. 1097, pp. 146–155, 2007.
- [31] G. C. Schwindt and S. E. Black, "Functional imaging studies of episodic memory in Alzheimer's disease: a quantitative meta-analysis," *Neuroimage*, vol. 45, no. 1, pp. 181–190, 2009.
- [32] K. A. Celone, V. D. Calhoun, B. C. Dickerson et al., "Alterations in memory networks in mild cognitive impairment and Alzheimer's disease: an independent component analysis," *The Journal of Neuroscience*, vol. 26, no. 40, pp. 10222–10231, 2006.
- [33] M. Pihlajamäsignki, K. M. DePeau, D. Blacker, and R. A. Sperling, "Impaired medial temporal repetition suppression is related to failure of parietal deactivation in Alzheimer disease," *The American Journal of Geriatric Psychiatry*, vol. 16, no. 4, pp. 283–292, 2008.
- [34] W. E. Klunk, H. Engler, A. Nordberg et al., "Imaging brain amyloid in Alzheimer's disease with Pittsburgh Compound-B," *Annals of Neurology*, vol. 55, no. 3, pp. 306–319, 2004.
- [35] M. M. Machulda, H. A. Ward, B. Borowski et al., "Comparison of memory fMRI response among normal, MCI, and Alzheimer's patients," *Neurology*, vol. 61, no. 4, pp. 500–506, 2003.
- [36] A. Hämäläinen, M. Pihlajamäki, H. Tanila et al., "Increased fMRI responses during encoding in mild cognitive impairment," *Neurobiology of Aging*, vol. 28, no. 12, pp. 1889–1903, 2007.
- [37] B. C. Dickerson, D. H. Salat, D. N. Greve et al., "Increased hippocampal activation in mild cognitive impairment compared to normal aging and AD," *Neurology*, vol. 65, no. 3, pp. 404–411, 2005.
- [38] C. Sorg, V. Riedl, M. Mühlau et al., "Selective changes of resting-state networks in individuals at risk for Alzheimer's disease," *Proceedings of the National Academy of Sciences of the United States of America*, vol. 104, no. 47, pp. 18760–18765, 2007.
- [39] J. R. Petrella, F. C. Sheldon, S. E. Prince, V. D. Calhoun, and P. M. Doraiswamy, "Default mode network connectivity in stable vs progressive mild cognitive impairment," *Neurology*, vol. 76, no. 6, pp. 511–517, 2011.
- [40] M. F. Mendez, M. A. Mendez, R. Martin, K. A. Smyth, and P. J. Whitehouse, "Complex visual disturbances in Alzheimer's disease," *Neurology*, vol. 40, no. 3, pp. 439–443, 1990.
- [41] A. Cronin-Golomb, S. Corkin, J. F. Rizzo, J. Cohen, J. H. Growdon, and K. S. Banks, "Visual dysfunction in Alzheimer's disease: relation to normal aging," *Annals of Neurology*, vol. 29, no. 1, pp. 41–52, 1991.

- [42] C. M. Butter, J. D. Trobe, N. L. Foster, and S. Berent, "Visual-spatial deficits explain visual symptoms in Alzheimer's disease," *American Journal of Ophthalmology*, vol. 122, no. 1, pp. 97–105, 1996.
- [43] M. Mapstone, T. M. Steffenella, and C. J. Duffy, "A visuospatial variant of mild cognitive impairment: getting lost between aging and AD," *Neurology*, vol. 60, no. 5, pp. 802–808, 2003.
- [44] M. Livingstone and D. Hubel, "Segregation of form, color, movement, and depth: anatomy, physiology, and perception," *Science*, vol. 240, no. 4853, pp. 740–749, 1988.
- [45] G. Rizzolatti and M. Matelli, "Two different streams form the dorsal visual system: anatomy and functions," *Experimental Brain Research*, vol. 153, no. 2, pp. 146–157, 2003.
- [46] P. Fattori, S. Pitzalis, and C. Galletti, "The cortical visual area V6 in macaque and human brains," *Journal of Physiology-Paris*, vol. 103, no. 1-2, pp. 88–97, 2009.
- [47] M. Gamberini, L. Passarelli, P. Fattori et al., "Cortical connections of the visuomotor parietooccipital area V6Ad of the macaque monkey," *The Journal of Comparative Neurology*, vol. 513, no. 6, pp. 622–642, 2009.
- [48] R. C. Pearson, M. M. Esiri, R. W. Hiorns, G. K. Wilcock, and T. P. Powell, "Anatomical correlates of the distribution of the pathological changes in the neocortex in Alzheimer's disease," *Proceedings of the National Academy of Sciences of the United States of America*, vol. 82, no. 13, pp. 4531–4534, 1985.
- [49] J. Rogers and J. H. Morrison, "Quantitative morphology and regional and laminar distributions of senile plaques in Alzheimer's disease," *The Journal of Neuroscience*, vol. 5, no. 10, pp. 2801–2808, 1985.
- [50] D. A. Lewis, M. J. Campbell, R. D. Terry, and J. H. Morrison, "Laminar and regional distributions of neurofibrillary tangles and neuritic plaques in Alzheimer's disease: a quantitative study of visual and auditory cortices," *The Journal of Neuroscience*, vol. 7, no. 6, pp. 1799–1808, 1987.
- [51] S. E. Arnold, B. T. Hyman, J. Flory, A. R. Damasio, and G. W. Van Hoesen, "The topographical and neuroanatomical distribution of neurofibrillary tangles and neuritic plaques in the cerebral cortex of patients with Alzheimer's disease," *Cerebral Cortex*, vol. 1, no. 1, pp. 103–116, 1991.
- [52] P. R. Hof and J. H. Morrison, "Quantitative analysis of a vulnerable subset of pyramidal neurons in Alzheimer's disease: II. Primary and secondary visual cortex," *The Journal of Comparative Neurology*, vol. 301, no. 1, pp. 55–64, 1990.
- [53] K. R. Thulborn, C. Martin, and J. T. Voyvodic, "Functional MR imaging using a visually guided saccade paradigm for comparing activation patterns in patients with probable Alzheimer's disease and in cognitively able elderly volunteers," *American Journal of Neuroradiology*, vol. 21, no. 3, pp. 524–531, 2000.
- [54] D. Prvulovic, D. Hubel, A. T. Sack et al., "Functional imaging of visuospatial processing in Alzheimer's disease," *Neuroimage*, vol. 17, no. 3, pp. 1403–1414, 2002.
- [55] A. L. W. Bokde, P. Lopez-Bayo, C. Born et al., "Alzheimer disease: functional abnormalities in the dorsal visual pathway," *Radiology*, vol. 254, no. 1, pp. 219–226, 2010.
- [56] T. Yamasaki, T. Fujita, Y. Kamio, and S. Tobimatsu, "Motion perception in autism spectrum disorder," in *Advances in Psychology Research*, A. M. Columbus, Ed., vol. 82, Nova Science Publishers, New York, NY, USA, in press.
- [57] A. L. W. Bokde, P. Lopez-Bayo, C. Born et al., "Functional abnormalities of the visual processing system in subjects with mild cognitive impairment: an fMRI study," *Psychiatry Research*, vol. 163, no. 3, pp. 248–259, 2008.
- [58] P. Vannini, O. Almkvist, T. Dierks, C. Lehmann, and L. O. Wahlund, "Reduced neuronal efficacy in progressive mild cognitive impairment: a prospective fMRI study on visuospatial processing," *Psychiatry Research*, vol. 156, no. 1, pp. 43–57, 2007.
- [59] S. N. Thiyagesh, T. F. D. Farrow, R. W. Parks et al., "The neural basis of visuospatial perception in Alzheimer's disease and healthy elderly comparison subjects: an fMRI study," *Psychiatry Research*, vol. 172, no. 2, pp. 109–116, 2009.
- [60] S. N. Thiyagesh, T. F. D. Farrow, R. W. Parks et al., "Treatment effects of therapeutic cholinesterase inhibitors on visuospatial processing in Alzheimer's disease: a longitudinal functional MRI study," *Dementia and Geriatric Cognitive Disorders*, vol. 29, no. 2, pp. 176–188, 2010.
- [61] S. Pitzalis, M. I. Sereno, G. Committeri et al., "Human V6: the medial motion area," *Cerebral Cortex*, vol. 20, no. 2, pp. 411–424, 2010.
- [62] W. T. Newsome and E. B. Paré, "A selective impairment of motion perception following lesions of the middle temporal visual area (MT)," *The Journal of Neuroscience*, vol. 8, no. 6, pp. 2201–2211, 1988.
- [63] M. Niedeggen and E. R. Wist, "Characteristics of visual evoked potentials generated by motion coherence onset," *Cognitive Brain Research*, vol. 8, no. 2, pp. 95–105, 1999.
- [64] M. C. Morrone, M. Tosetti, D. Montanaro, A. Fiorentini, G. Cioni, and D. C. Burr, "A cortical area that responds specifically to optic flow, revealed by fMRI," *Nature Neuroscience*, vol. 3, no. 12, pp. 1322–1328, 2000.
- [65] J. J. Gibson, *The Perception of the Visual World*, Houghton Mifflin, Boston, Mass, USA, 1950.
- [66] W. H. Warren and D. J. Hannon, "Direction of self-motion is perceived from optical flow," *Nature*, vol. 336, no. 6195, pp. 162–163, 1988.
- [67] K. Tanaka and H. A. Saito, "Analysis of motion of the visual field by direction, expansion/contraction, and rotation cells clustered in the dorsal part of the medial superior temporal area of the macaque monkey," *Journal of Neurophysiology*, vol. 62, no. 3, pp. 626–641, 1989.
- [68] R. M. Siegel and H. L. Reid, "Analysis of optic flow in the monkey parietal area 7a," *Cerebral Cortex*, vol. 7, no. 4, pp. 327–346, 1997.
- [69] A. Mikami, W. T. Newsome, and R. H. Wurtz, "Motion selectivity in macaque visual cortex. I. Mechanisms of direction and speed selectivity in extrastriate area MT," *Journal of Neurophysiology*, vol. 55, no. 6, pp. 1308–1327, 1986.
- [70] S. Tetewsky and C. J. Duffy, "Visual loss and getting lost in Alzheimer's disease," *Neurology*, vol. 52, no. 5, pp. 958–965, 1999.
- [71] H. L. O'Brien, S. Tetewsky, L. M. Avery, L. A. Cushman, W. Makous, and C. J. Duffy, "Visual mechanisms of spatial disorientation in Alzheimer's disease," *Cerebral Cortex*, vol. 11, no. 11, pp. 1083–1092, 2001.
- [72] B. M. de Jong, S. Shipp, B. Skidmore, R. S. Frackowiak, and S. Zeki, "The cerebral activity related to the visual perception of forward motion in depth," *Brain*, vol. 117, no. 5, pp. 1039–1054, 1994.
- [73] M. Ptito, R. Kupers, J. Faubert, and A. Gjedde, "Cortical representation of inward and outward radial motion in man," *Neuroimage*, vol. 14, no. 6, pp. 1409–1415, 2001.
- [74] G. Wunderlich, J. C. Marshall, K. Amunts et al., "The importance of seeing it coming: a functional magnetic resonance imaging study of motion-in-depth towards the human observer," *Neuroscience*, vol. 112, no. 3, pp. 535–540, 2002.

- [75] B. Biswal, F. Z. Yetkin, V. M. Haughton, and J. S. Hyde, "Functional connectivity in the motor cortex of resting human brain using echo-planar MRI," *Magnetic Resonance in Medicine*, vol. 34, no. 4, pp. 537–541, 1995.
- [76] K. Wang, T. Jiang, C. Yu et al., "Spontaneous activity associated with primary visual cortex: a resting-state fMRI study," *Cerebral Cortex*, vol. 18, no. 3, pp. 697–704, 2008.
- [77] M. D. Fox, A. Z. Snyder, J. L. Vincent, M. Corbetta, D. C. Van Essen, and M. E. Raichle, "The human brain is intrinsically organized into dynamic, anticorrelated functional networks," *Proceedings of the National Academy of Sciences of the United States of America*, vol. 102, no. 27, pp. 9673–9678, 2005.
- [78] D. S. Margulies, J. Böttger, X. Long et al., "Resting developments: a review of fMRI post-processing methodologies for spontaneous brain activity," *Magnetic Resonance Materials in Physics, Biology and Medicine*, vol. 23, no. 5-6, pp. 289–307, 2010.
- [79] G. Buzsáki and A. Draguhn, "Neuronal oscillations in cortical networks," *Science*, vol. 304, no. 5679, pp. 1926–1929, 2004.
- [80] M. D. Fox and M. E. Raichle, "Spontaneous fluctuations in brain activity observed with functional magnetic resonance imaging," *Nature Reviews Neuroscience*, vol. 8, no. 9, pp. 700–711, 2007.
- [81] C. F. Beckmann and S. M. Smith, "Tensorial extensions of independent component analysis for multisubject FMRI analysis," *Neuroimage*, vol. 25, no. 1, pp. 294–311, 2005.
- [82] J. S. Damoiseaux, S. A. Rombouts, F. Barkhof et al., "Consistent resting-state networks across healthy subjects," *Proceedings of the National Academy of Sciences of the United States of America*, vol. 103, no. 37, pp. 13848–13853, 2006.
- [83] M. De Luca, C. F. Beckmann, N. De Stefano, P. M. Matthews, and S. M. Smith, "fMRI resting state networks define distinct modes of long-distance interactions in the human brain," *Neuroimage*, vol. 29, no. 4, pp. 1359–1367, 2006.
- [84] M. Hampson, B. S. Peterson, P. Skudlarski, J. C. Gatenby, and J. C. Gore, "Detection of functional connectivity using temporal correlations in MR images," *Human Brain Mapping*, vol. 15, no. 4, pp. 247–262, 2002.
- [85] S. J. Li, Z. Li, G. Wu, M. J. Zhang, M. Franczak, and P. G. Antuono, "Alzheimer disease: evaluation of a functional MR imaging index as a marker," *Radiology*, vol. 225, no. 1, pp. 253–259, 2002.
- [86] L. Wang, Y. Zang, Y. He et al., "Changes in hippocampal connectivity in the early stages of Alzheimer's disease: evidence from resting state fMRI," *Neuroimage*, vol. 31, no. 2, pp. 496–504, 2006.
- [87] H. Y. Zhang, S. J. Wang, J. Xing et al., "Detection of PCC functional connectivity characteristics in resting-state fMRI in mild Alzheimer's disease," *Behavioural Brain Research*, vol. 197, no. 1, pp. 103–108, 2009.
- [88] G. Allen, H. Barnard, R. McColl et al., "Reduced hippocampal functional connectivity in Alzheimer's disease," *Archives of Neurology*, vol. 64, no. 10, pp. 1482–1487, 2007.
- [89] F. Bai, D. R. Watson, H. Yu, Y. Shi, Y. Yuan, and Z. Zhang, "Abnormal resting-state functional connectivity of posterior cingulate cortex in amnesic type mild cognitive impairment," *Brain Research*, vol. 1302, pp. 167–174, 2009.
- [90] C. Sorg, V. Riedl, M. Mühlau et al., "Selective changes of resting-state networks in individuals at risk for Alzheimer's disease," *Proceedings of the National Academy of Sciences of the United States of America*, vol. 104, no. 47, pp. 18760–18765, 2007.
- [91] Z. Qi, X. Wu, Z. Wang et al., "Impairment and compensation coexist in amnesic MCI default mode network," *Neuroimage*, vol. 50, no. 1, pp. 48–55, 2010.
- [92] K. Supekar, V. Menon, D. Rubin, M. Musen, and M. D. Greicius, "Network analysis of intrinsic functional brain connectivity in Alzheimer's disease," *PLoS Computational Biology*, vol. 4, no. 6, Article ID e1000100, 2008.
- [93] L. Wang, Y. Zang, Y. He et al., "Changes in hippocampal connectivity in the early stages of Alzheimer's disease: evidence from resting state fMRI," *Neuroimage*, vol. 31, no. 2, pp. 496–504, 2006.
- [94] K. Wang, M. Liang, L. Wang et al., "Altered functional connectivity in early Alzheimer's disease: a resting-state fMRI study," *Human Brain Mapping*, vol. 28, no. 10, pp. 967–978, 2007.
- [95] E. J. Sanz-Arigita, M. M. Schoonheim, J. S. Damoiseaux et al., "Loss of 'small-world' networks in Alzheimer's disease: graph analysis of fMRI resting-state functional connectivity," *PLoS One*, vol. 5, no. 11, Article ID e13788, 2010.
- [96] G. Chen, B. D. Ward, C. Xie et al., "Classification of Alzheimer disease, mild cognitive impairment, and normal cognitive status with large-scale network analysis based on resting-state functional MR imaging," *Radiology*, vol. 259, no. 1, pp. 213–221, 2011.
- [97] H. Y. Zhang, S. J. Wang, B. Liu et al., "Resting brain connectivity: changes during the progress of Alzheimer disease," *Radiology*, vol. 256, no. 2, pp. 598–606, 2010.
- [98] T. Yamasaki and S. Tobimatsu, "Motion perception in healthy humans and cognitive disorders," in *Early Detection and Rehabilitation Technologies for Dementia: Neuroscience and Biomedical Applications*, J. Wu, Ed., pp. 156–161, IGI Global, Philadelphia, Pa, USA, 2011.
- [99] T. Yamasaki, T. Fujita, K. Ogata et al., "Electrophysiological evidence for selective impairment of optic flow perception in autism spectrum disorder," *Research in Autism Spectrum Disorders*, vol. 5, no. 1, pp. 400–407, 2011.
- [100] S. Tobimatsu, Y. Goto, T. Yamasaki, R. Tsurusawa, and T. Taniwaki, "An integrated approach to face and motion perception in humans," *Clinical Neurophysiology*, vol. 59, supplement, pp. 43–48, 2006.
- [101] S. Tobimatsu, Y. Goto, T. Yamasaki, R. Tsurusawa, and T. Taniwaki, "Non-invasive evaluation of face and motion perception in humans," *Journal of Physiological Anthropology and Applied Human Science*, vol. 23, no. 6, pp. 273–276, 2004.
- [102] S. Tobimatsu, Y. Goto, T. Yamasaki, T. Nakashima, Y. Tomoda, and A. Mitsudome, "Visual ERPs and cortical function," in *Progress In Epileptic Disorders*, A. Ikeda and Y. Inoue, Eds., Vol. 5, Event-Related Potentials In Patients With Epilepsy: From Current State To Future Prospects, pp. 37–48, John Libbey Eurotext, Paris, France, 2008.
- [103] K. G. Claey's, D. T. Lindsey, E. D. Schutter, and G. A. Orban, "A higher order motion region in human inferior parietal lobule: evidence from fMRI," *Neuron*, vol. 40, no. 3, pp. 631–642, 2003.
- [104] A. L. Paradis, J. Droulez, V. Cornilleau-Pérès, and J. B. Poline, "Processing 3D form and 3D motion: respective contributions of attention-based and stimulus-driven activity," *Neuroimage*, vol. 43, no. 4, pp. 736–747, 2008.
- [105] O. J. Braddick, J. M. D. O'Brien, J. Wattam-Bell, J. Atkinson, and T. Hartley, "Brain areas sensitive to coherent visual motion," *Perception*, vol. 30, no. 1, pp. 61–72, 2001.
- [106] M. Schroeter, T. Stein, N. Maslowski, and J. Neumann, "Neural correlates of Alzheimer's disease and mild cognitive impairment: a systematic and quantitative meta-analysis involving 1351 patients," *Neuroimage*, vol. 47, no. 4, pp. 1196–1206, 2009.

## Research Article

# A Pilot Study of Quantitative MRI Measurements of Ventricular Volume and Cortical Atrophy for the Differential Diagnosis of Normal Pressure Hydrocephalus

Dana W. Moore,<sup>1</sup> Ilhami Kovanlikaya,<sup>2</sup> Linda A. Heier,<sup>2</sup> Ashish Raj,<sup>2</sup> Chaorui Huang,<sup>1</sup> King-Wai Chu,<sup>3</sup> and Norman R. Relkin<sup>1</sup>

<sup>1</sup>Department of Neurology and Neuroscience, Weill Cornell Medical College, 428 East 72nd Street, Suite 500, New York, NY 10021, USA

<sup>2</sup>Department of Radiology, Weill Cornell Medical College, 525 East 68th Street, New York, NY 10065, USA

<sup>3</sup>Mental Illness Research, Education, and Clinical Center, James J. Peters VA Medical Center, 130 West Kingsbridge Road, Bronx, NY 10468, USA

Correspondence should be addressed to Norman R. Relkin, nrelkin@med.cornell.edu

Received 2 March 2011; Accepted 8 June 2011

Academic Editor: Andrea Cherubini

Copyright © 2012 Dana W. Moore et al. This is an open access article distributed under the Creative Commons Attribution License, which permits unrestricted use, distribution, and reproduction in any medium, provided the original work is properly cited.

Current radiologic diagnosis of normal pressure hydrocephalus (NPH) requires a subjective judgment of whether lateral ventricular enlargement is disproportionate to cerebral atrophy based on visual inspection of brain images. We investigated whether quantitative measurements of lateral ventricular volume and total cortical thickness (a correlate of cerebral atrophy) could be used to more objectively distinguish NPH from normal controls (NC), Alzheimer's (AD), and Parkinson's disease (PD). Volumetric MRIs were obtained prospectively from patients with NPH ( $n = 5$ ), PD ( $n = 5$ ), and NC (5). Additional NC ( $n = 5$ ) and AD patients ( $n = 10$ ) from the ADNI cohort were examined. Although mean ventricular volume was significantly greater in the NPH group than all others, the range of values overlapped those of the AD group. Individuals with NPH could be better distinguished when ventricular volume and total cortical thickness were considered in combination. This pilot study suggests that volumetric MRI measurements hold promise for improving NPH differential diagnosis.

## 1. Introduction

Normal pressure hydrocephalus (NPH) is a chronic neurologic disorder in adults characterized by impairments of gait, urination and cognition in association with enlargement of the cerebral ventricles. Brain imaging is integral to the diagnosis of NPH [1] and has also contributed to prognosticating response to shunt placement, which is the primary method of treating NPH at this time [2, 3].

The most characteristic physical change in the brains of NPH patients is ventricular enlargement. Radiographic identification of NPH is made by visual inspection of X-ray computed tomographic (CT) or magnetic resonance imaging (MRI) scans of the brain. Diagnosis can be challenging because ventricular enlargement also occurs as a

consequence of aging, cerebrovascular disorders, neurodegenerative diseases, and other forms of hydrocephalus. To distinguish NPH from these other conditions, a determination must be made that the ventricular enlargement is not wholly attributable to cerebral atrophy or macroscopic obstruction to cerebrospinal fluid circulation. Most clinicians use other signs of atrophy such as sulcal widening to judge whether the extent of ventricular enlargement is greater than expected from cerebral atrophy alone. Even when carried out by skilled readers, this assessment is subjective and prone to error. Although various imaging signs such as a rounded ventricular horns, expansion of the Sylvian fissure, thinning of the corpus callosum, and upward displacement of the superior parietal lobule may help to distinguish NPH from cerebral atrophy, these signs are not

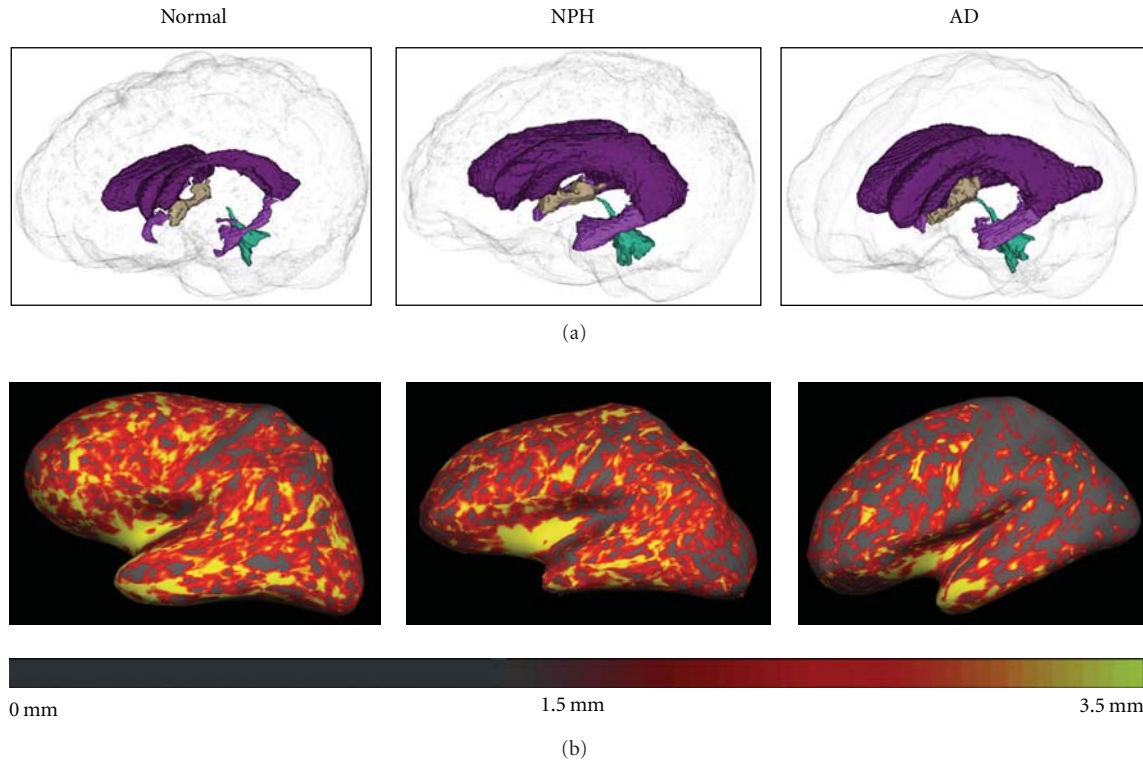


FIGURE 1: (a) Three-dimensional representation of the ventricles in normal, NPH, and AD participant (left to right). The ventricles of the NPH and the AD participants are enlarged relative to the normal participant. (b) FreeSurfer's cortical thickness maps in the same normal, NPH, and AD participant (left to right) are shown. The cortex of the AD participant is notably thinner, particularly in posterior regions, than that of the normal and NPH participant.

universally present or specific to NPH. Two-dimensional methods for quantifying ventricular enlargement such as the Evan's index [4] address only whether the ventricles are enlarged and are not particularly informative about the relative amount of cerebral atrophy present. Better methods are therefore needed to identify NPH radiologically and distinguish it from other conditions associated with ventricular enlargement.

In the past decade, several techniques have emerged for quantitatively measuring cerebral atrophy. Voxel-based morphometry (VBM) has been recently applied in a study that found NPH patients had overall preservation of the cortex with volume loss in periventricular regions [5]. This technique, which is best suited to group analyses, is sensitive to group coregistration issues and has limited applicability to individuals [6, 7]. The present study examines whether another method of quantitative MRI analysis that measures total cortical thickness (TCortTh) and lateral ventricular volume (VentVol), can be used to identify NPH cases and distinguish them from individuals with normal aging and other neurologic conditions. Distinguishing NPH from Parkinson's disease (PD) and Alzheimer's disease (AD) is of particular interest because these disorders are prevalent in the population at risk for NPH and sometimes have overlapping clinical features. An underlying assumption of our approach is that the extent of ventricular enlargement can be used to distinguish NPH from PD and normal aging

but extent of cortical thinning better differentiates NPH from AD (Figure 1). We hypothesized that neither VentVol nor TCortTh alone would fully distinguish NPH from other diagnostic groups but that the combination of these two measures could improve NPH differential diagnosis.

## 2. Methods

**2.1. Participants.** In this study, 5 NPH participants were recruited from the Weill Cornell Medical College (WCMC) Memory Disorders Program and were identified by a neurologist or neurosurgeon as having Probable NPH by International Consensus (IC) criteria [1]. This involved subjective interpretation by a radiologist of ventricular size upon visual inspection of an MRI or CT. Actual measurements of ventricular size and cortical thickness were not used for diagnostic purposes. In addition, all 5 NPH participants were responsive to shunt placement, which was further supportive of the diagnoses.

Five normal control (NC) and 10 AD participants, matched for age and gender, were chosen at random from the Alzheimer's Disease Neuroimaging Initiative (ADNI) dataset [8] (<http://www.loni.ucla.edu/ADNI>). In addition, five PD participants were recruited from the WCMC Movement Disorders Clinic having been diagnosed according to the United Kingdom Parkinson's Disease Society Brain Bank criteria [9]. Because these participants were younger than

TABLE 1

Group	<i>n</i>	M:F	Age
NPH	5	3:2	81 ± 4 (76–87)
AD	10	6:4	81 ± 5 (74–87)
PD	5	2:3	69 ± 4 (64–73)
NC-younger	5	4:1	68 ± 6 (64–78)
NC-older	5	3:2	81 ± 4 (76–86)

the other groups, 5 additional younger NC participants were recruited through advertisements and referrals. See Table 1 for demographic characteristics.

**2.2. Procedures.** All participants gave informed consent. For prospective participants (NPH, PD, and younger NC), sagittal 3D BRAVO MRI sequences were performed on a 3T GE Signa scanner located at the WCMC Citigroup Biomedical Imaging Center. ADNI images (AD and older NC) were acquired from a straight sagittal 3D MPRAGE sequence.

### 2.3. Imaging Measures

**2.3.1. Cortical Thickness.** Measurement of cortical thickness, based on the perpendicular distance from the pial surface to the gray/white matter juncture, is a validated measure of cerebral atrophy. FreeSurfer [10–15] is an image analysis software package available in the public domain (<http://surfer.nmr.mgh.harvard.edu>) that provides automated global and regional measures of cortical thickness. FreeSurfer performs gyral-based cortical parcellation using an algorithm that incorporates probable locations of regions of interest and the potential interparticipant variance based on the sample used. The atlas-generated ROIs were highly accurate compared to manual ROIs using intraclass correlation and mean distance maps [11]. Cortical thickness measurements have been shown to be reliable across different MRI platforms [15], and correlations between cortical thickness and cognition were reliable across different scanner platforms and different field strengths [16]. FreeSurfer (version 4.5.0) provided average cortical thickness values for the left and right hemispheres by automatically calculating the average of the values at each vertex across the hemisphere. FreeSurfer's reconstruction was checked for all participants, and edits were made where needed. The values of the two hemispheres were averaged to provide a measure of TCortTh across the entire cortex for final analyses. Middle temporal thickness (MTempTh) was also measured because prior research has suggested that the middle temporal lobe is relatively resistant to aging [17] but sensitive to AD [18, 19].

**2.3.2. Total Intracranial Volume (TICV).** To control for head size, total intracranial volume was derived from the MRIs by an automated routine, using FreeSurfer.

**2.3.3. Evans Index.** The Evans Index is the ratio of the maximal frontal horn ventricular width to the transverse

diameter of the inner table of the skull. A ratio of 0.3 or greater signifies ventriculomegaly [4].

**2.3.4. Ventricular Volume.** We used a semiautomated algorithm for measuring ventricular volume, implemented in the program Brain Ventricular Quantification (BVQ [20]). BVQ correctly filled the lateral ventricles with minimal manual editing in cases of NPH. BVQ uses a seed point/region-growing method and is optimized specifically for segmentation of the lateral ventricles. In longitudinal studies, BVQ has been shown to successfully differentiate AD patients from NC participants based on annual percent change in ventricular volume [21]. BVQ was therefore chosen to measure VentVol for the purposes of this study.

**2.3.5. Data Analysis.** *T*-tests were used to compare the younger and older NC groups on the outcome measures, and Chi-Square was used to determine if gender distribution differed across groups. Group differences in TICV were calculated with ANOVA. Group and pairwise comparisons of imaging outcomes were calculated using nonparametric methods (Kruskal-Wallis Rank Test). For the purposes of this exploratory analysis, no adjustments were made for multiple comparisons.

## 3. Results

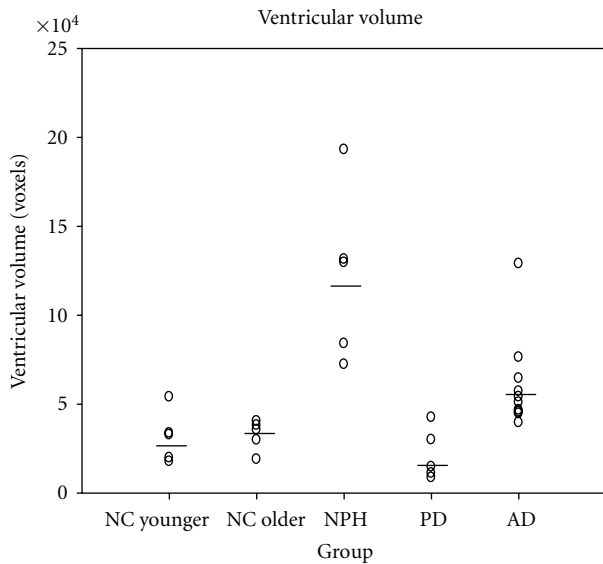
The younger and older NC participants did not significantly differ from each other on any outcome variable. For the purposes of subsequent analyses, the NC participants were all treated as one group. Chi-square results showed no significant differences between groups in gender distribution. One-way ANOVA was significant for group differences in TICV,  $F(3,26) = 5.131$ ,  $P = .006$ , and post hoc testing showed that NPH participants had significantly larger TICV than all other groups ( $P < .05$ ), and PD participants had significantly smaller TICV than all other groups ( $P < .05$ ).

All 5 of the NPH participants scored an Evans Index above the cutoff for ventricular enlargement. Five of the 10 AD participants and 1 of the 5 older NC participants also scored above this cutoff. Kruskal-Wallis Tests across all groups showed significant differences in VentVol ( $P = .000$ ), VentVol/TICV ( $P = .000$ ), TCortTh ( $P = .042$ ), and MTempTh ( $P = .002$ ). Pairwise Kruskal-Wallis Tests showed that NPH participants had significantly larger VentVol and VentVol/TICV compared to all other groups with  $P < .05$  for all comparisons. AD participants had significantly larger VentVol and VentVol/TICV compared to NC and PD participants at  $P < .01$ . NPH participants had lower TCortTh compared to PD participants ( $P = .028$ ). AD participants had lower TCortTh compared to NC ( $P = .021$ ) and PD ( $P = .037$ ) participants. NPH participants had lower MTempTh compared to NC ( $P = .022$ ) participants, and AD participants had lower MTempTh compared to all other groups at  $P < .05$ . NC and PD participants did not significantly differ from each other on any outcome. See Table 2 for descriptive statistics.

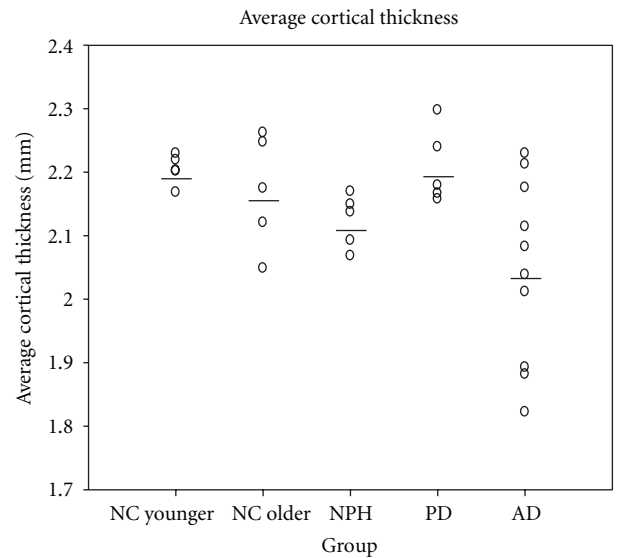
When VentVol was examined in ratio to TCortTh, Kruskal-Wallis results showed that groups significantly differed,

TABLE 2

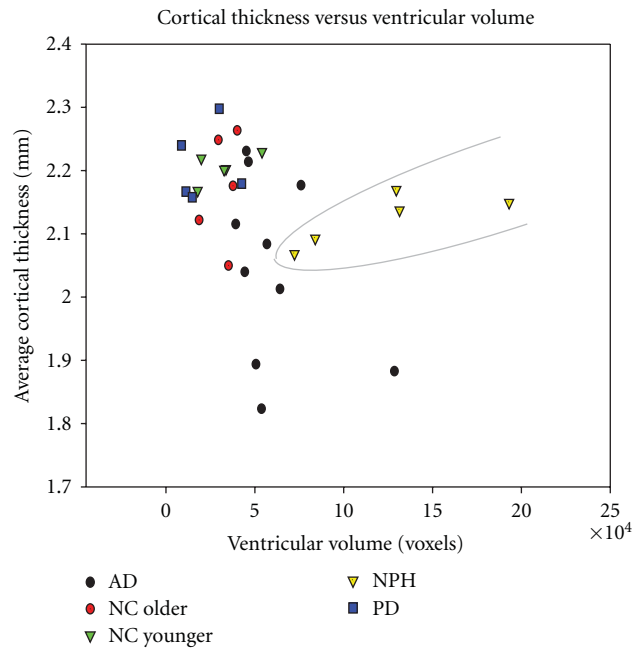
Group	TICV (cm <sup>3</sup> )	VentVol (cm <sup>3</sup> )	TCortTh (mm)	MTempTh (mm)	Proportion of participants with Evans Index >0.3
NC	1493 ± 156	32 ± 11	2.19 ± .06	2.64 ± .12	1/10
PD	1301 ± 153	21 ± 14	2.21 ± .06	2.58 ± .18	0/5
AD	1490 ± 164	61 ± 26	2.05 ± .14	2.29 ± .18	5/10
NPH	1706 ± 186	122 ± 48	2.12 ± .04	2.48 ± .09	5/5



(a)



(b)



(c)

FIGURE 2: (a) Ventricular volume of NPH subjects overlaps that of AD patients. (b) Cortical thickness overlaps among all groups, with AD the best distinguished. (c) When ventricular volume and cortical thickness are both taken into account, NPH can be more clearly distinguished from the other groups.

$P = .000$ . Pairwise Kruskal-Wallis Tests showed that NPH had significantly larger ratios than all other groups with  $P < .05$  for all comparisons. AD participants had significantly larger ratios compared to NC and PD groups at  $P < .01$ .

Results were plotted to examine for patterns that might distinguish NPH from other groups using VentVol and TCortTh (Figure 2). While neither VentVol nor TCortTh alone could separate the NPH participants from other groups, a combination of the two measures more clearly distinguished the NPH participants from the others.

#### 4. Discussion

As a group, the NPH patients in this study had larger total intracranial volumes than other subjects, an observation consistent with past reports of increased head-size among adult NPH patients [22]. Despite the fact that NPH patients had significantly larger ventricular volumes than all other groups including AD, there was overlap in this measure between the NPH and AD participants (Figure 2(a)). The Evans Index also failed to differentiate between groups, as several AD and one older NC participant scored above the cutoff for ventricular enlargement. This is consistent with the observation that it is difficult to distinguish ventriculomegaly due to NPH and AD based on ventricular size alone. NPH patients also showed a large degree of overlap with other groups in measures of global or regional cortical thickness. The AD group has significantly different total cortical thickness and middle temporal thickness than the other groups, but these measures did not distinguish all AD patients from the other patient groups. Accordingly, neither ventricular volume nor cortical thickness alone would be expected to adequately serve as the basis for differential diagnosis of NPH individual patients. However, when both VentVol and TCortTh were considered together as in Figure 2(c), subjects with an NPH diagnosis can be more clearly separated from NC and patients with AD and PD.

The volumetric analysis techniques employed in this study have become more widely available, efficient, and user friendly in recent years. Fully automated measurements of cortical thickness and ventricular volume may be less subject to interrater variations and therefore more suitable for clinical use. Limitations to the present study include the small number of subjects and the use of images obtained with different MRI platforms and sequences. Although these factors are likely to have influenced the absolute values of our ventricular volume and cortical thickness measurements, the outcomes obtained for these parameters in this study are consistent with those in the literature [21].

Differential diagnosis of NPH from AD and other neurological disorders might be assisted by additional biomarkers. Positron emission tomography (PET) imaging with amyloid tracers detects amyloid plaques in the brain, which are characteristic of AD [23]. This technique could be used to confirm this study's findings in individual cases, but it would require carrying out an expensive, additional test. The 42-amino acid subtype of the amyloid beta protein is present in cerebrospinal fluid (CSF) and is associated with AD [24]. Other CSF biomarkers include total tau and phosphorylated

tau [24, 25]. Amyloid PET and CSF biomarkers, however, have not been shown to conclusively distinguish AD from NPH, although ongoing studies can help to address this [26]. Future research can combine the MRI measures examined in the current study with other biomarkers to further improve the accuracy of the differential diagnosis of NPH.

Future follow-up studies with larger samples can use parametric statistics such as logistic regression to further establish the separation of NPH from other groups based on ventricular volume and cortical thickness. In addition, future studies can examine cortical thickness and/or volume changes in specific structures that are vulnerable to AD to further improve the differential diagnosis of NPH relative to AD. Hippocampal volume, however, may not be as useful in differentiating the two diseases because it can be reduced in NPH due to compression by the expanded temporal horn of the lateral ventricle. Cortical structures, being farther removed from the ventricles, might better contribute to the differential diagnosis of NPH. In this study, middle temporal thickness was not as effective as total cortical thickness in distinguishing groups, since NPH patients showed thinning of this area. Further research is needed to identify specific areas of the cortex that can contribute to the differential diagnosis of NPH.

Another possible confounder to this analytic strategy in practice is the simultaneous occurrence of NPH and AD or PD in the same patient. Such cases were excluded from the present analysis but are often encountered in clinical practice. Further studies will be required to determine if patients with dual diagnoses can be identified by these methods.

#### 5. Conclusion

While these preliminary findings require replication in larger numbers of subjects, these results highlight the promise of combining quantitative measures of cortical thickness and ventricular volume as potential brain imaging markers for the differential diagnosis of NPH.

#### Acknowledgments

This research was supported by funding from the Leon Levy Foundation (N. R. Relkin), the Hydrocephalus Association (D. W. Moore), and the NIH Grant No.5R01 NS 064038 (C. Huang). Data collection and sharing for this project was funded by the Alzheimer's Disease Neuroimaging Initiative (ADNI) (National Institutes of Health Grant U01 AG024904). ADNI is funded by the National Institute on Aging, the National Institute of Biomedical Imaging and Bioengineering, and through generous contributions from the following: Abbott, AstraZeneca AB, Bayer Schering Pharma AG, Bristol-Myers Squibb, Eisai Global Clinical Development, Elan Corporation, Genentech, GE Healthcare, Glaxo-SmithKline, Innogenetics, Johnson and Johnson, Eli Lilly and Co., Medpace, Inc., Merck and Co., Inc., Novartis AG, Pfizer Inc, F. Hoffman-La Roche, Schering-Plough, Synarc, Inc., as well as nonprofit partners the Alzheimer's Association and Alzheimer's Drug Discovery Foundation, with participation from the US Food and Drug Administration. Private sector

contributions to ADNI are facilitated by the Foundation for the National Institutes of Health (<http://www.fnih.org/>). The grantee organization is the Northern California Institute for Research and Education, and the study is coordinated by the Alzheimer's Disease Cooperative Study at the University of California, San Diego. ADNI data are disseminated by the Laboratory for Neuro Imaging at the University of California, Los Angeles. This paper was also supported by NIH Grants P30 AG010129, K01 AG030514, and the Dana Foundation.

## References

- [1] N. Relkin, A. Marmarou, P. Klinge, M. Bergsneider, and P. M. Black, "INPH guidelines, part II: diagnosing idiopathic normal-pressure hydrocephalus," *Neurosurgery*, vol. 57, no. 3, pp. S4–S16, 2005.
- [2] R. C. Petersen, B. Mokri, and E. R. Laws Jr., "Surgical treatment of idiopathic hydrocephalus in elderly patients," *Neurology*, vol. 35, no. 3, pp. 307–311, 1985.
- [3] J. Vanneste, P. Augustijn, W. F. Tan, and C. Dirven, "Shunting normal pressure hydrocephalus: the predictive value of combined clinical and CT data," *Journal of Neurology Neurosurgery and Psychiatry*, vol. 56, no. 3, pp. 251–256, 1993.
- [4] W. Evans, "An encephalographic ratio for estimating ventricular enlargement and cerebral atrophy," *Archives of Neurology and Psychiatry*, vol. 47, pp. 931–937, 1942.
- [5] K. Ishii, T. Kawaguchi, K. Shimada et al., "Voxel-based analysis of gray matter and CSF space in idiopathic normal pressure hydrocephalus," *Dementia and Geriatric Cognitive Disorders*, vol. 25, no. 4, pp. 329–335, 2008.
- [6] F. L. Bookstein, "'voxel-based morphometry' should not be used with imperfectly registered images," *NeuroImage*, vol. 14, no. 6, pp. 1454–1462, 2001.
- [7] J. L. Whitwell, "Voxel-based morphometry: an automated technique for assessing structural changes in the brain," *Journal of Neuroscience*, vol. 29, no. 31, pp. 9661–9664, 2009.
- [8] C. R. Jack Jr., M. A. Bernstein, N. C. Fox et al., "The Alzheimer's Disease Neuroimaging Initiative (ADNI): MRI methods," *Journal of Magnetic Resonance Imaging*, vol. 27, no. 4, pp. 685–691, 2008.
- [9] A. J. Hughes, S. E. Daniel, L. Kilford, and A. J. Lees, "Accuracy of clinical diagnosis of idiopathic Parkinson's disease: a clinico-pathological study of 100 cases," *Journal of Neurology Neurosurgery and Psychiatry*, vol. 55, no. 3, pp. 181–184, 1992.
- [10] A. M. Dale, B. Fischl, and M. I. Sereno, "Cortical surface-based analysis: I. Segmentation and surface reconstruction," *NeuroImage*, vol. 9, no. 2, pp. 179–194, 1999.
- [11] R. S. Desikan, F. Ségonne, B. Fischl et al., "An automated labeling system for subdividing the human cerebral cortex on MRI scans into gyral based regions of interest," *NeuroImage*, vol. 31, no. 3, pp. 968–980, 2006.
- [12] B. Fischl, D. H. Salat, E. Busa et al., "Whole brain segmentation: automated labeling of neuroanatomical structures in the human brain," *Neuron*, vol. 33, no. 3, pp. 341–355, 2002.
- [13] B. Fischl, M. I. Sereno, and A. M. Dale, "Cortical surface-based analysis: II. Inflation, flattening, and a surface-based coordinate system," *NeuroImage*, vol. 9, no. 2, pp. 195–207, 1999.
- [14] B. Fischl, A. van der Kouwe, C. Destrieux et al., "Automatically parcellating the human cerebral cortex," *Cerebral Cortex*, vol. 14, no. 1, pp. 11–22, 2004.
- [15] X. Han, J. Jovicich, D. Salat et al., "Reliability of MRI-derived measurements of human cerebral cortical thickness: the effects of field strength, scanner upgrade and manufacturer," *NeuroImage*, vol. 32, no. 1, pp. 180–194, 2006.
- [16] B. C. Dickerson, E. Fenstermacher, D. H. Salat et al., "Detection of cortical thickness correlates of cognitive performance: reliability across MRI scan sessions, scanners, and field strengths," *NeuroImage*, vol. 39, no. 1, pp. 10–18, 2008.
- [17] D. H. Salat, R. L. Buckner, A. Z. Snyder et al., "Thinning of the cerebral cortex in aging," *Cerebral Cortex*, vol. 14, no. 7, pp. 721–730, 2004.
- [18] R. S. Desikan, H. J. Cabral, B. Fischl et al., "Temporoparietal MR imaging measures of atrophy in subjects with mild cognitive impairment that predict subsequent diagnosis of Alzheimer disease," *American Journal of Neuroradiology*, vol. 30, no. 3, pp. 532–538, 2009.
- [19] R. S. Desikan, B. Fischl, H. J. Cabral et al., "MRI measures of temporoparietal regions show differential rates of atrophy during prodromal AD," *Neurology*, vol. 71, no. 11, pp. 819–825, 2008.
- [20] V. L. R. Accomazzi, C. J. Barlow, and B. Davey, "inventors; Cedara Software Corp., assignee. Image region segmentation system and method," US Patent Application, 2005.
- [21] S. M. Nestor, R. Rupsingh, M. Borrie et al., "Ventricular enlargement as a possible measure of Alzheimer's disease progression validated using the Alzheimer's disease neuroimaging initiative database," *Brain*, vol. 131, no. 9, pp. 2443–2454, 2008.
- [22] T. A. Krefft, N. R. Graff-Radford, J. A. Lucas, and J. A. Mortimer, "Normal pressure hydrocephalus and large head size," *Alzheimer Disease and Associated Disorders*, vol. 18, no. 1, pp. 35–37, 2004.
- [23] W. E. Klunk, H. Engler, A. Nordberg et al., "Imaging brain amyloid in Alzheimer's disease with pittsburgh compound-B," *Annals of Neurology*, vol. 55, no. 3, pp. 306–319, 2004.
- [24] J. M. Schott, "Using CSF biomarkers to replicate genetic associations in Alzheimer's disease," *Neurobiology of Aging*. In press, 2011.
- [25] L. M. Shaw, H. Vanderstichele, M. Knapik-Czajka et al., "Cerebrospinal fluid biomarker signature in alzheimer's disease neuroimaging initiative subjects," *Annals of Neurology*, vol. 65, no. 4, pp. 403–413, 2009.
- [26] S. Assuras, *Cerebrospinal fluid biomarkers for the differential diagnosis of normal pressure hydrocephalus and Alzheimer's disease*, Doctoral dissertation, The Graduate Center and Queens College, City University of New York, New York, NY, USA, 2010.

## Review Article

# MRI Findings in Neuroferritinopathy

**Emiko Ohta and Yoshihisa Takiyama**

*Department of Neurology, Interdisciplinary Graduate School of Medicine and Engineering, University of Yamanashi, 1110 Shimokato, Chuo, Yamanashi 409-3898, Japan*

Correspondence should be addressed to Emiko Ohta, oemiko@cup.ocn.ne.jp

Received 12 March 2011; Revised 10 May 2011; Accepted 23 May 2011

Academic Editor: Antonio Cerasa

Copyright © 2012 E. Ohta and Y. Takiyama. This is an open access article distributed under the Creative Commons Attribution License, which permits unrestricted use, distribution, and reproduction in any medium, provided the original work is properly cited.

Neuroferritinopathy is a neurodegenerative disease which demonstrates brain iron accumulation caused by the mutations in the ferritin light chain gene. On brain MRI in neuroferritinopathy, iron deposits are observed as low-intensity areas on T2WI and as signal loss on T2\*WI. On T2WI, hyperintense abnormalities reflecting tissue edema and gliosis are also seen. Another characteristic finding is the presence of symmetrical cystic changes in the basal ganglia, which are seen in the advanced stages of this disorder. Atrophy is sometimes noted in the cerebellar and cerebral cortices. The variety in the MRI findings is specific to neuroferritinopathy. Based on observations of an excessive iron content in patients with chronic neurologic disorders, such as Parkinson disease and Alzheimer disease, the presence of excess iron is therefore recognized as a major risk factor for neurodegenerative diseases. The future development of multimodal and advanced MRI techniques is thus expected to play an important role in accurately measuring the brain iron content and thereby further elucidating the neurodegenerative process.

## 1. Introduction

Neuroferritinopathy is an autosomal dominant neurodegenerative disorder characterized by the deposition of iron and ferritin in the brain and a decreased level of serum ferritin. The disease is caused by a mutation in the ferritin light chain gene [1]. Seven different pathogenic mutations of the ferritin light chain gene have been identified [1–7]. These mutations are predicted to affect the tertiary structure and stability of the ferritin light chain polypeptide and may cause inappropriate iron release from ferritin polymers [8, 9]. It is supposed that the excess iron induces free toxic radical production, which leads to tissue oxidative stress and neuronal cell death [10–12]. The clinical features of neuroferritinopathy are characterized by the adult onset of extrapyramidal motor symptoms: dystonia, chorea, choreoathetosis, parkinsonism, and tremor. Some patients may present cerebellar ataxia, cognitive decline, and pyramidal signs [2, 3, 5–7]. The phenotypic signs of the disease are variable, even among members of the same family [1, 3]. Generally, there are no nonneurological symptoms [13], different from in other neurodegenerative brain iron

accumulation diseases. The clinical features of neuroferritinopathy are not specific, and they overlap with those of common extrapyramidal disorders. It is difficult to diagnose neuroferritinopathy solely based on the clinical findings. Brain MR imaging in the disease is quite characteristic and it may facilitate differential diagnosis of neuroferritinopathy from other extrapyramidal disorders.

## 2. Brain MR Imaging in Neuroferritinopathy

We will review the findings in neuroferritinopathy with conventional MRI methods, T1-weighted imaging, T2-weighted imaging, and T2\*-weighted imaging. On T1WI, there is a sharp contrast between the parenchyma and ventricles, and it is adequate for evaluating brain atrophy and cystic changes. T2WI is suitable for detecting the pathological processes with an increase in water content, such as gliosis, edema and axonal/neuronal loss, as hyperintense signals. On T2\*WI with a gradient echo sequence, the signals are readily influenced by magnetic inhomogeneity. Therefore, T2\*WI is sensitive enough to detect paramagnetism such as that of iron.

Signal abnormalities on brain MR imaging were observed in all affected individuals previously reported except for one case [13–15]. Despite the clinical differences, the neuroimaging is similar across cases [16]. The findings are usually bilateral and symmetric but sometimes asymmetric [3, 17]. Signal changes are found in widespread areas in the central nervous system [14].

Radiological findings in patients with neuroferritinopathy have been shown to correlate with the observed pathology [18]. The abnormalities observed on MRI reflect four pathological changes: iron deposition, edema and gliosis, cystic changes, and cortical atrophy [1–3]. Each finding is described individually below.

**2.1. Iron Deposition.** Iron is essential for normal neuronal metabolism, but excessive iron may be harmful [19, 20]. It is known that iron overload can cause free-radical formation and neuronal damage.

Physiologically, brain iron appears to be found predominantly in the extrapyramidal system, in particular the globus pallidus, substantia nigra, red nucleus, and putamen. It has been shown that moderate levels of iron occur in the striatum, thalamus, cerebral cortex, cerebellar cortex, and deep white matter [21]. It is also known that iron deposition increases normally with age. The brain histopathology of affected individuals with neuroferritinopathy involves excess iron and ferritin deposits throughout the forebrain and cerebellum, notably in the basal ganglia [1–3]. The accumulation observed in affected patients exceeds that found in normal elderly individuals. However, these regions still exhibit the general distribution pattern for iron in the normal aging brain [1].

On fast spin echo T2WI, iron deposits are demonstrated as low-intensity areas and as signal loss on gradient echo T2\*WI [13, 22]. Comparison of T2WI and T2\*WI sequences suggests that the T2\* one is more sensitive for the detection of iron, while the T2 fast spin echo T2WI sequence is more frequently used in routine clinical practice [14]. In particular, the cortical iron deposition in neuroferritinopathy is hardly detectable on T2WI but is easily observed on T2\*WI [14]. Generally, iron deposit regions are isointense on T1WI [23].

**2.2. Degeneration.** T2 hyperintense abnormalities are seen in the pallidum, putamen, caudate nucleus [1, 3], thalamus and dentate nucleus, and sometimes in the red nucleus and substantia nigra [16, 24] in patients with neuroferritinopathy. The border of a lesion has a tendency to be unclear and the signal is unequal. These changes are supposed to reflect tissue degeneration with edema and gliosis observed pathologically. Because of the increased water content, the lesions are detected as hyperintense signals on T2WI [25]. Around these hyperintense areas, hypointensity due to iron deposits is frequently seen.

**2.3. Cystic Changes.** On MRI in neuroferritinopathy, the bilateral cystic changes involving the pallidum and putamen are impressive. Cavities are demonstrated as low-intensity signals on T1WI and high-intensity signals on T2WI,

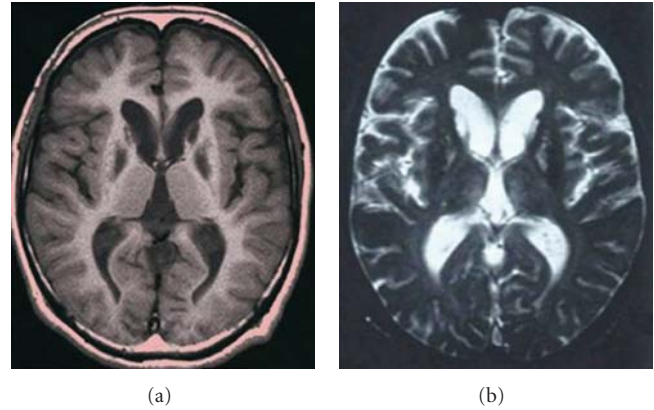


FIGURE 1: Axial section at the level of the basal ganglia in the patient at 35 years of age. (a) A T1-weighted image (TR 400 msec/ TE 14 msec) shows symmetrical hypointense signals in the head of the caudate nucleus and globus pallidus. (b) A T2-weighted image (TR 800 msec/TE 30 msec) shows hypointense changes in the lenticular nucleus. Hyperintense signals can be observed in the putamen and the head of the caudate nucleus.

compared with the CSF signal. In the region adjacent to a cystic lesion, severe loss of nerve cells and neuropil is observed pathologically. In one case, Vidal et al. reported that microcavities measuring up to 1.5 mm in diameter were seen in the putamen anatomically and that these cavities were consistent with small hypointense areas on T1WI and to hyperintense ones on T2WI on MRI [2]. This finding is thought to represent the beginning stage of cavity formation.

McNeill et al. analyzed the MRI findings in 21 patients with neuroferritinopathy. In 52% (11/21 patients), they found that the globus pallidus and/or putamen coincided with a confluent area of hyperintensity and that this hyperintense area was likely to be due to fluid within an area of cystic degeneration. It is usually accompanied by a rim of peripheral hypointensity reflecting iron deposition. This is a characteristic imaging pattern in neuroferritinopathy. The presence of large cysts is thought to be a finding observed at an advanced stage [14].

**2.4. Cortical Atrophy.** On brain MRI in neuroferritinopathy, atrophy is sometimes noted in the cerebellar cortices and cerebral cortices, notably in the frontal lobe. Atrophy of the cerebellar and cerebral cortices has also been anatomically identified. Regarding on clinicoradiologic correlation, patients having cerebellar atrophy present ataxia [2, 3, 26], and ones having cerebral atrophy present cognitive decline [23, 26].

### 3. The Relationship between the Stage of the Disease and MRI Findings

The first MRI change is loss of the T2\* signal due to iron deposits. In an early symptomatic stage, and even in an asymptomatic carrier, there is obvious signal loss on T2\* imaging in the basal ganglia, especially in the globus pallidus, at considerable frequency. In conventional spin

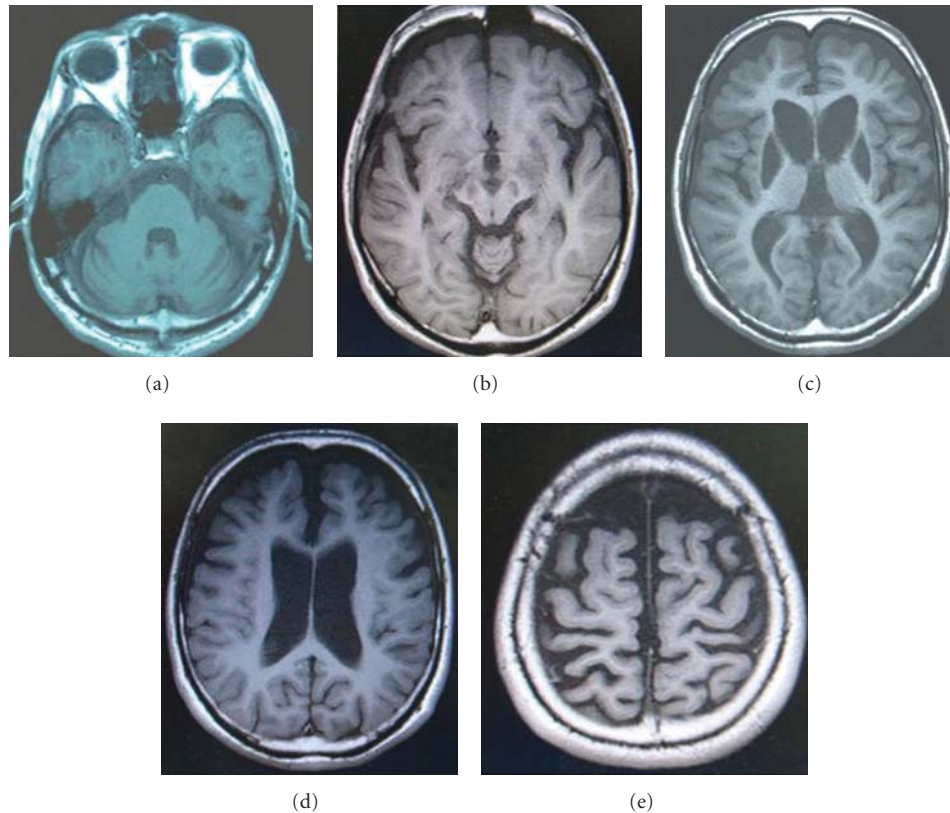


FIGURE 2: T1-weighted images (TR 400 msec/ TE 9 msec) of the same patient at 42 years of age. (a) A cross-section at the pontine level shows cerebellar cortex atrophy. (b) An image of a midbrain section demonstrates the hypointense change in the substantia nigra. (c) An image at the level of the basal ganglia shows symmetrical hypointense signals in the head of the caudate nucleus and globus pallidus. As compared with the findings at 35 years, the hypointense signals in the pallidum extend to the putamen. The cystic changes of the lenticular nuclei can be clearly observed. The shape of the cyst is fan shaped and exactly fits the region of the lenticular nucleus. The cerebral cortex in the frontal lobes is atrophic. The hypointense lesion in the caudate head observed in the image at 35 years of age seems to be combined with the hypointense signal of the anterior horn of the lateral ventricle. (d) In this image, enlargement of the lateral ventricles is evident. (e) This image shows cerebral cortical atrophy.

echo MR sequences, the signal change is inconspicuous and is observed as a minor low signal on T2WI [13]. There has only been one report of that brain MR T2WI was normal without evidence of iron deposition; however, it was obtained six years after the onset of neuroferritinopathy symptoms. In this case, the T2\* sequence was not examined at that time. The follow-up MRI performed 16 years after the onset, however, showed typical abnormalities [15].

With disease progression, the T2 hypointense signal and T2\* signal loss become more pronounced [13]. The changes eventually extend to the thalamus, dentate nucleus, substantia nigra, red nucleus, and cerebral cortex.

In the middle stage of the disorder, T2 hyperintense abnormalities reflecting tissue edema and gliosis are observed. In the basal ganglia, this change is thought to represent precystic degeneration [13]. The hypersignal lesions are often intermixed with decreased intensity areas corresponding to iron deposits. The combination of hyperintense and hypointense abnormalities is found in the pallidum, putamen, thalamus, and dentate nucleus frequently and sometimes in the red nucleus and substantia nigra [17, 27].

The characteristic finding on brain MRI at the advanced stage is symmetrical cystic degeneration of the basal ganglia [16, 28]. Pathologically, many microcavities due to the loss of neurophils and neurons are observed, which are consistent with hypointense areas on T1WI and with hyperintense ones on T2WI on MRI [2]. It is supposed that small cavities merge to form larger cavities with progression of the disease. The large cavities observed on MRI have been confirmed by macropathological investigation [1].

#### 4. MRI Findings in Our Case

Brain MR images of our case are presented in Figures 1, 2, 3, and 4. Our patient is a 42-year-old Japanese man who first developed hand tremor in his middle teens. He noticed his right foot dragging at age 35, and generalized hypotonia, hyperextensibility, aphonia, micrographia, hyperreflexia, dystonia of his face, and cognitive impairment at age 42. Rigidity, spasticity, and chorea were not observed. His deceased mother had presented similar symptoms. His serum ferritin concentration was apparently low. He was

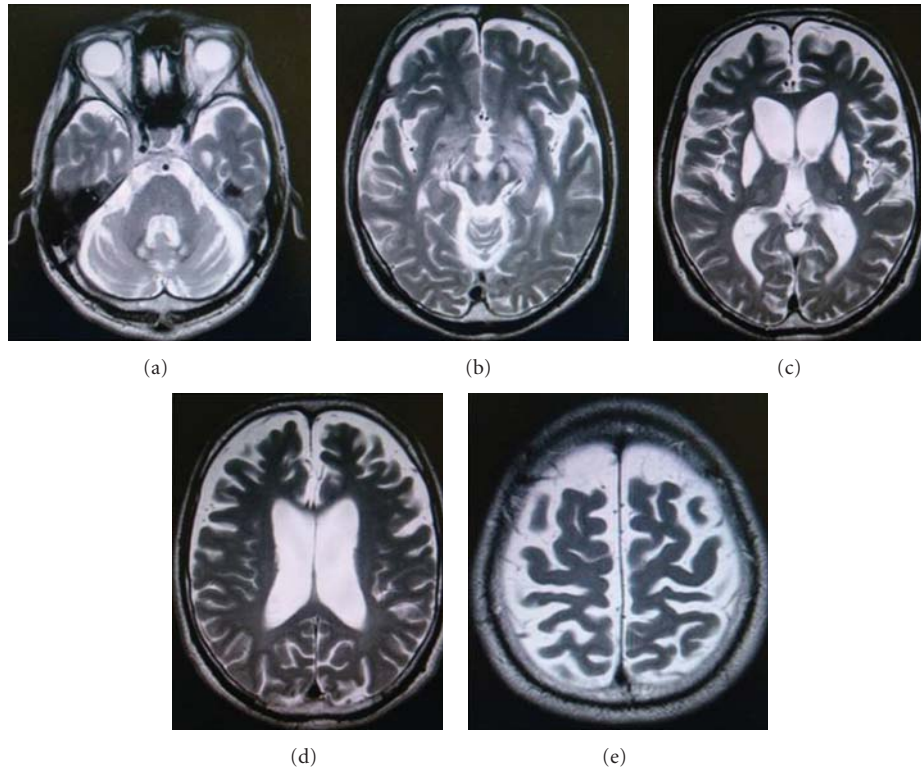


FIGURE 3: T2-weighted images (TR 3,440 msec/TE 89.4 msec) at 42 years old. (a) A cross-section at the pontine level exhibits bilateral and symmetrical signal loss with central hyperintense abnormalities in the dentate nucleus with cerebellar cortical atrophy. (b) An image of a midbrain section demonstrates the symmetrical increased signal intensity involving the substantia nigra. A decreased signal change is observed in the red nucleus. (c) An image at the level of the basal ganglia shows hyperintensity with a band of surrounding hypointensity affecting the putamen and pallidum. Foggy high signal changes can be seen in the inner part of the thalamus bilaterally. (d) An image of a section of the central part of the lateral ventricles. (e) An image of a section of the cerebral cortex. The signal change is not evident.

tested by means of the molecular technique and diagnosed as having neuroferritinopathy because a mutation of the ferritin light chain gene was detected [5].

All images presented here were taken with a 1.5 Tesla MR System. T1-weighted, T2-weighted, and T2\*-weighted sequences were collected in the transverse plane. A T1-weighted image is useful for evaluating the atrophy and size of a cyst. As compared with the image at 35 years (Figure 1), that at 42 years demonstrates progression of the cystic formation and deterioration of the cortical atrophy in the frontal lobes (Figures 2(c) and 3(c)). Cortical atrophy can also be seen in the cerebellum (Figure 2(a)). Enlargement of the lateral ventricles is evident (Figure 2(d)).

A T2-weighted image is valuable for detecting the combination of degenerative change and iron accumulation. A clear hyperintense lesion with a hypointense signal was found in the center of the dentate nucleus (Figure 3(a)). Foggy high signal changes were found in the inner part of the thalamus bilaterally (Figure 3(c)). These lesions are supposed to reflect the edema and gliosis observed pathologically.

T2\* images are valuable for detecting iron deposition. Iron deposits were indicated as signal loss in the dentate nuclei (Figure 4(a)), red nuclei (Figure 4(b)), thalamus (Figure 4(c)), at the periphery of the cysts (Figure 4(c)), and in the cerebral cortex (Figure 4(e)) in T2\*-weighted images.

## 5. Differential Diagnosis

In this section, we provide an overview of the MRI findings in three other subtypes of neurodegeneration with brain iron accumulation (NBIA): pantothenate kinase-2 associated neurodegeneration (PKAN, formerly known as Hallervorden-Spatz syndrome), aceruloplasminemia, and infantile neuroaxonal dystrophy (INAD) for the differential diagnosis of iron deposition in the basal ganglia. Over the last decade, iron deposition in the adult brain is being increasingly recognized as an indicator of neurodegenerative processes in many chronic neurologic disorders including Parkinson disease and Alzheimer disease. We also mention the MRI findings in these common neurodegenerative diseases.

PKAN is a childhood-onset extrapyramidal disorder with aberrant iron metabolism caused by a mutation of the pantothenate kinase-2 (PANK2) gene [29]. Brain MRI findings in patients with the PANK2 mutation include hypointensity with an area of central hyperintensity in the globus pallidi on T2- and T2\*-imaging, this characteristic sign being called the “eye-of-the-tiger” sign [14, 30–32]. McNeill et al. reported that two of 21 cases of neuroferritinopathy presented the “eye-of-the-tiger” sign and that the MRI findings in these iron accumulative disorders sometimes might overlap. He

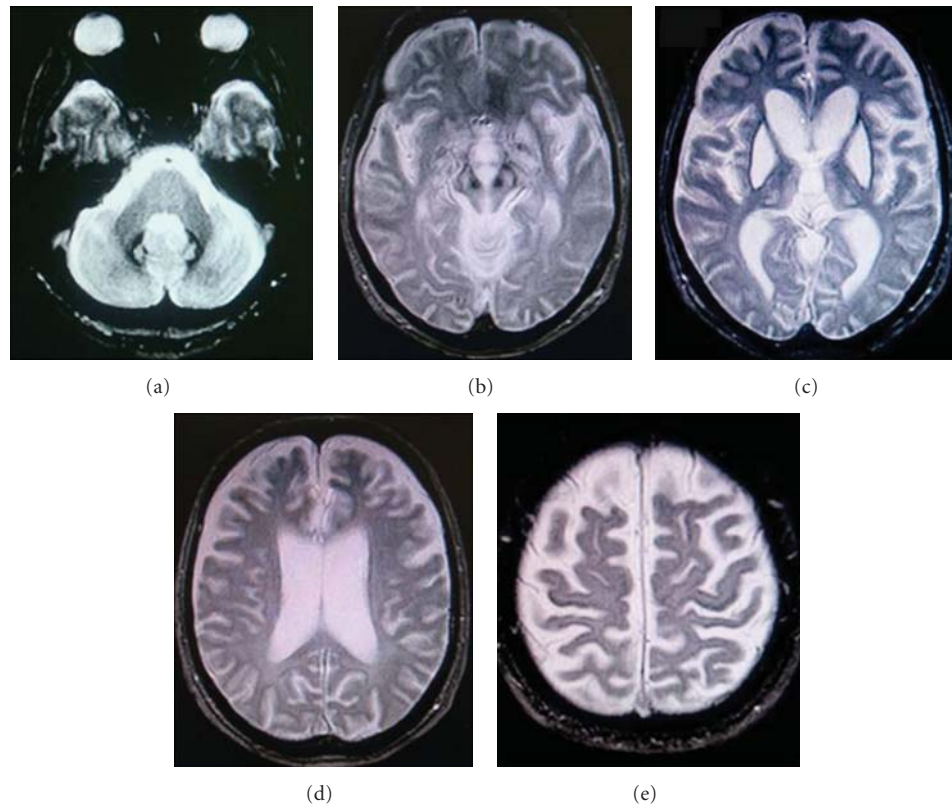


FIGURE 4: T2\*-weighted images (TR 400 msec/ TE 25 msec) obtained with a gradient echo sequence in the same patient at 42 years old. (a) A cross-section at the pontine level. The signal loss with central hyperintense lesions in the dentate nucleus is more obvious than that observed on T2WI. (b) An image of the midbrain demonstrates the hypointense change in the red nucleus. (c) Cystic degeneration of the basal ganglia with a rim of peripheral signal loss is obvious. In the thalamus, bilateral hyperintense abnormalities surrounded by slight hypointensity can be seen. (d) An image of a section of the central part of the lateral ventricles. (e) The iron deposition in the cerebral cortex is detected as signal loss.

emphasized the importance of repeat imaging for a more accurate clinical diagnosis [14]. In the majority of PKAN cases, abnormalities are restricted to the globus pallidus and substantia nigra. In neuroferritinopathy, lesions in the globus pallidus, putamen, and dentate nuclei are consistently accompanied by ones in the caudate nuclei or thalami in a subset. The widespread location of lesions throughout the central nervous system is one of the characteristic MR findings in neuroferritinopathy patients [14].

Aceruloplasminemia is an adult onset extrapyramidal disorder with iron deposition in the brain, liver, and reticuloendothelial system. It is caused by a mutation of the ceruloplasmin gene. The iron deposition in the central nervous system in aceruloplasminemia exhibits a distribution comparable to that in neuroferritinopathy, but in aceruloplasminemia, all basal ganglia nuclei and thalami are simultaneously involved as seen in T2-weighted and T2\*-weighted images. A further distinguishing feature is the lack of the combination of hyperintense and hypointense abnormalities that is often observed in neuroferritinopathy. The low signal areas observed in aceruloplasminemia are homogenous. The cystic changes of the basal ganglia observed in neuroferritinopathy are rarely seen in aceruloplasminemia [13, 14, 33].

INAD is an autosomal recessive disorder with motor and mental deterioration, appearing within the first two years of life. It is due to mutations in *PLA2G6*. The characteristic MRI finding in INAD patients is cerebellar atrophy, which is often accompanied by signal hyperintensity in the diffuse cerebellar cortex [34]. In INAD, abnormal iron accumulation, detected as hypointense lesions on T2WI and T2\*WI, is mainly observed in the globus pallidus, sometimes in the substantia nigra, and occasionally in the dentate nuclei. Even in advanced cases of INAD, there has been no report of iron accumulation in other structures [14]. It is different from the frequent involvement of the putamen, caudate and thalami in neuroferritinopathy. It has been observed in two INAD families with *PLA2G6* mutations that no iron accumulation was detectable on MRI despite severe clinical symptoms [35]. The cystic changes of the basal ganglia are not seen in INAD.

Patients with Parkinson disease (PD) may show T2 hypointensity in many anatomic areas compared to normal controls including the substantia nigra pars compacta, dentate nucleus, subthalamic nucleus, and basal ganglia, probably reflecting an excess iron content. Quantitative studies have shown a 25% to 100% increase in substantia nigra iron

levels in patients with PD compared to in normal controls. The correlation between T2 hypointensity of the substantia nigra and clinical severity has been demonstrated [22].

In patients with Alzheimer disease (AD), iron deposition in neurons, neurofibrillary tangles, and plaques has been reported pathologically. To detect brain iron accumulation using MRI in AD, investigators tried the high-resolution 4.7 T MRI or field-dependent-rate-increase (FDRI) technique [22]. In these studies, increased iron levels were found in the basal ganglia.

The signal change on MRI reflecting an excess iron content observed in patients with chronic neurologic disorders such as PD and AD is usually slight as compared with that in patients with NBIA including neuroferritinopathy. For exact measurement of brain iron or mineralization as a major risk factor for neurodegenerative diseases, multimodal and advanced MRI techniques are proposed [36, 37]. Improvement of MRI technique is one of the most important goals for correct diagnosis.

## 6. Conclusion

The variety of MRI findings including cystic degeneration of the basal ganglia, the combination of hyperintense and hypointense abnormalities, T2 hypointense lesions reflecting iron deposits, and cortical atrophy are specific to neuroferritinopathy.

In cases of suspected neuroferritinopathy, MRI may be useful for the detection and confirmation of such findings. At an early stage, since the abnormal iron deposits might be not detectable on T2-weighted imaging, T2\*-weighted imaging is recommended. In most cases, there are clear distinguishing features for neuroferritinopathy and other iron accumulative disorders, including PKAN, INAD, and aceruloplasminemia. However, there is a degree of radiological overlap between neuroferritinopathy and these other iron accumulative disorders.

The multimodal and advanced MRI techniques being developed to more sensitively and specifically quantify brain iron will be important for correct diagnosis and better understanding of the neurodegenerative processes in the pathological brain.

## References

- [1] A. R. J. Curtis, C. Fey, C. M. Morris et al., "Mutation in the gene encoding ferritin light polypeptide causes dominant adult-onset basal ganglia disease," *Nature Genetics*, vol. 28, no. 4, pp. 350–354, 2001.
- [2] R. Vidal, B. Ghetti, M. Takao et al., "Intracellular ferritin accumulation in neural and extraneural tissue characterizes a neurodegenerative disease associated with a mutation in the ferritin light polypeptide gene," *Journal of Neuropathology and Experimental Neurology*, vol. 63, no. 4, pp. 363–380, 2004.
- [3] M. Mancuso, G. Davidzon, R. M. Kurlan et al., "Hereditary ferritinopathy: a novel mutation, its cellular pathology, and pathogenetic insights," *Journal of Neuropathology and Experimental Neurology*, vol. 64, no. 4, pp. 280–294, 2005.
- [4] P. Maciel, V. T. Cruz, M. Constante et al., "Neuroferritinopathy: missense mutation in FTL causing early-onset bilateral pallidal involvement," *Neurology*, vol. 65, no. 4, pp. 603–605, 2005.
- [5] E. Ohta, T. Nagasaka, K. Shindo et al., "Neuroferritinopathy in a Japanese family with a duplication in the ferritin light chain gene," *Neurology*, vol. 70, no. 16, part 2, pp. 1493–1494, 2008.
- [6] D. Devos, P. J. Tchofo, I. Vuillaume et al., "Clinical features and natural history of neuroferritinopathy caused by the 458dupA FTL mutation," *Brain*, vol. 132, no. 6, p. e109, 2009.
- [7] A. Kubota, A. Hida, Y. Ichikawa et al., "A novel ferritin light chain gene mutation in a Japanese family with neuroferritinopathy: description of clinical features and implications for genotype-phenotype correlations," *Movement Disorders*, vol. 24, no. 3, pp. 441–445, 2009.
- [8] S. Levi, A. Cozzi, and P. Arosio, "Neuroferritinopathy: a neurodegenerative disorder associated with L-ferritin mutation," *Best Practice and Research: Clinical Haematology*, vol. 18, no. 2, pp. 265–276, 2005.
- [9] R. Vidal, L. Miravalle, X. Gao et al., "Expression of a mutant form of the ferritin light chain gene induces neurodegeneration and iron overload in transgenic mice," *Journal of Neuroscience*, vol. 28, no. 1, pp. 60–67, 2008.
- [10] T. A. Rouault, "Iron on the brain," *Nature Genetics*, vol. 28, no. 4, pp. 299–300, 2001.
- [11] Y. Ke and Z. M. Qian, "Iron misregulation in the brain: a primary cause of neurodegenerative disorders," *Lancet Neurology*, vol. 2, no. 4, pp. 246–253, 2003.
- [12] A. Cozzi, E. Rovelli, G. Frizzale et al., "Oxidative stress and cell death in cells expressing L-ferritin variants causing neuroferritinopathy," *Neurobiology of Disease*, vol. 37, no. 1, pp. 77–85, 2010.
- [13] P. F. Chinnery, D. E. Crompton, D. Birchall et al., "Clinical features and natural history of neuroferritinopathy caused by the FTL1 460InsA mutation," *Brain*, vol. 130, no. 1, pp. 110–119, 2007.
- [14] A. McNeill, D. Birchall, S. J. Hayflick et al., "T2\* and FSE MRI distinguishes four subtypes of neurodegeneration with brain iron accumulation," *Neurology*, vol. 70, no. 18, pp. 1614–1619, 2008.
- [15] P. Mir, M. J. Edwards, A. R. J. Curtis, K. P. Bhatia, and N. P. Quinn, "Adult-onset generalized dystonia due to a mutation in the neuroferritinopathy gene," *Movement Disorders*, vol. 20, no. 2, pp. 243–245, 2005.
- [16] D. E. Crompton, P. F. Chinnery, D. Bates et al., "Spectrum of movement disorders in neuroferritinopathy," *Movement Disorders*, vol. 20, no. 1, pp. 95–98, 2005.
- [17] D. Caparros-Lefebvre, A. Destée, and H. Petit, "Late onset familial dystonia: could mitochondrial deficits induce a diffuse lesioning process of the whole basal ganglia system?" *Journal of Neurology, Neurosurgery and Psychiatry*, vol. 63, no. 2, pp. 196–203, 1997.
- [18] D. E. Crompton, P. F. Chinnery, C. Fey et al., "Neuroferritinopathy: a window on the role of iron in neurodegeneration," *Blood Cells, Molecules and Diseases*, vol. 29, no. 3, pp. 522–531, 2002.
- [19] P. M. Harrison and P. Arosio, "The ferritins: molecular properties, iron storage function and cellular regulation," *Biochimica et Biophysica Acta*, vol. 1275, no. 3, pp. 161–203, 1996.
- [20] C. W. Olanow and G. W. Arendash, "Metals and free radicals in neurodegeneration," *Current Opinion in Neurology*, vol. 7, no. 6, pp. 548–558, 1994.

- [21] C. M. Morris, J. M. Candy, A. E. Oakley, C. A. Bloxham, and J. A. Edwardson, "Histochemical distribution of non-haem iron in the human brain," *Acta Anatomica*, vol. 144, no. 3, pp. 235–257, 1992.
- [22] J. Stankiewicz, S. S. Panter, M. Neema, A. Arora, C. E. Batt, and R. Bakshi, "Iron in chronic brain disorders: imaging and neurotherapeutic implications," *Neurotherapeutics*, vol. 4, no. 3, pp. 371–386, 2007.
- [23] A. Gregory, B. J. Polster, and S. J. Hayflick, "Clinical and genetic delineation of neurodegeneration with brain iron accumulation," *Journal of Medical Genetics*, vol. 46, no. 2, pp. 73–80, 2009.
- [24] P. F. Chinnery, A. R. J. Curtis, C. Fey et al., "Neuroferritinopathy in a French family with late onset dominant dystonia," *Journal of Medical Genetics*, vol. 40, no. 5, p. e69, 2003.
- [25] F. Ory-Magne, C. Brefel-Courbon, P. Payoux et al., "Clinical phenotype and neuroimaging findings in a French family with hereditary ferritinopathy (FTL498-499InsTC)," *Movement Disorders*, vol. 24, no. 11, pp. 1676–1683, 2009.
- [26] E. Ohta, T. Nagasaka, K. Shindo et al., "Clinical features of neuroferritinopathy," *Clinical Neurology*, vol. 49, no. 5, pp. 254–261, 2009.
- [27] A. J. Wills, G. V. Sawle, P. R. Guilbert, and A. R. J. Curtis, "Palatal tremor and cognitive decline in neuroferritinopathy," *Journal of Neurology Neurosurgery and Psychiatry*, vol. 73, no. 1, pp. 91–92, 2002.
- [28] J. Burn and P. F. Chinnery, "Neuroferritinopathy," *Seminars in Pediatric Neurology*, vol. 13, no. 3, pp. 176–181, 2006.
- [29] B. Zhou, S. K. Westaway, B. Levinson, M. A. Johnson, J. Gitschier, and S. J. Hayflick, "A novel pantothenate kinase gene (PANK2) is defective in Hallervorden-Spatz syndrome," *Nature Genetics*, vol. 28, no. 4, pp. 345–349, 2001.
- [30] S. J. Hayflick, M. Hartman, J. Coryell, J. Gitschier, and H. Rowley, "Brain MRI in neurodegeneration with brain iron accumulation with and without PANK2 mutations," *American Journal of Neuroradiology*, vol. 27, no. 6, pp. 1230–1233, 2006.
- [31] S. J. Hayflick, S. K. Westaway, B. Levinson et al., "Genetic, clinical, and radiographic delineation of Hallervorden-Spatz syndrome," *New England Journal of Medicine*, vol. 348, no. 1, pp. 33–40, 2003.
- [32] M. C. Sharma, N. Aggarwal, M. Bihari et al., "Hallervorden Spatz disease: MR and pathological findings of a rare case," *Neurology India*, vol. 53, no. 1, pp. 102–104, 2005.
- [33] H. Morita, S. Ikeda, K. Yamamoto et al., "Hereditary ceruloplasmin deficiency with hemosiderosis: a clinicopathological study of a Japanese family," *Annals of Neurology*, vol. 37, no. 5, pp. 646–656, 1995.
- [34] J. Kóbor, A. Javaid, and M. F. Omojola, "Cerebellar hypoperfusion in infantile neuroaxonal dystrophy," *Pediatric Neurology*, vol. 32, no. 2, pp. 137–139, 2005.
- [35] C. Paisan-Ruiz, K. P. Bhatia, A. Li et al., "Characterization of PLA2G6 as a locus for dystonia-parkinsonism," *Annals of Neurology*, vol. 65, no. 1, pp. 19–23, 2009.
- [36] P. Péran, G. Hagberg, G. Luccichenti et al., "Voxel-based analysis of R2\* maps in the healthy human brain," *Journal of Magnetic Resonance Imaging*, vol. 26, no. 6, pp. 1413–1420, 2007.
- [37] A. Cherubini, P. Péran, C. Caltagirone, U. Sabatini, and G. Spalletta, "Aging of subcortical nuclei: microstructural, mineralization and atrophy modifications measured in vivo using MRI," *Neuroimage*, vol. 48, no. 1, pp. 29–36, 2009.